ABSTRACT

Title of dissertation: ASSESSMENT OF TURBULENCE LENGTH SCALES IN HYBRID RANS-LES METHODS

Nishan Jain
Doctor of Philosophy, 2017

Dissertation directed by: Professor James D. Baeder
Aerospace Engineering Department

Separated flows are common in many scenarios of practical interest. Key examples of these scenarios include static stall over fixed wing aircraft and dynamic stall over rotorcraft blades. During rotor operation at high advance ratio, the stall events lead to loss in performance of the rotorcraft and may cause severe aerodynamic loads. In order to mitigate vibratory loads, it is important to evaluate the involved flow physics as accurately as possible. It is well known that a complex rotor flow field involving separation and reverse flow cannot be numerically predicted reliably by classical RANS model. At the other end, using high-fidelity approaches such as DNS and LES to resolve the rotor flow-field at practical Reynolds number is beyond the current computational capabilities. Therefore, the main objective of this work is to develop a high-fidelity modeling framework for capturing flow features that are important for predicting stall events while remaining computationally affordable. The framework employs and refines DES type hybrid RANS-LES methods along with specialized numerical techniques from literature to accurately resolve incipient separated flows under static and dynamic conditions. A baseline computational framework compris-

ing of well established laminar-turbulent transition model, adverse pressure gradient (APG) correction and a low Mach number correction is selected as a starting point.

By conducting simulations of flow over SC1095 airfoil at near-stall regime using the baseline framework, the importance of regulating eddy viscosity in the outer part of the shear layer is realized. Sub-grid length scales from the literature are implemented into the in-house computational solvers and their sensitivity in generating the eddy viscosity is investigated. A novel length scale called SSM length scale is proposed based on the properties of available length scales and the grid requirements in mildly separated flows. Proposed length scale demonstrated good predictive capabilities in mildly separated flows under static conditions by reducing eddy viscosity levels at the outer region boundary layer. Three-dimensional dynamic stall simulations are also conducted on flow over the modified VR12 airfoil. With SSM length scale, DDES method predictions agreed well with experimental data and captured the cycle-to-cycle variation of integrated aerodynamic quantities.

The undesirable weakening of conventional shielding is observed due to proposed length scale in a highly resolved computational domain. A novel and stronger shielding formulation are proposed based on the properties of available length scales. The combination of new shielding and SSM length scale demonstrated good predictive capabilities in near stall regime without any undesirable effects. The combination also eliminated the need for adverse pressure gradient correction.

The final computational framework proved to be robust towards grid resolution and varying flow separation and provided highly accurate aerodynamic characteristics for rotorcraft airfoils exhibiting stall events in the complete angle of attack range.

Assessment of Turbulence Length Scales in Hybrid RANS-LES Methods

by

Nishan Jain

Dissertation submitted to the Faculty of the Graduate School of the
University of Maryland, College Park in partial fulfillment
of the requirements for the degree of
Doctor of Philosophy
2017

Advisory Committee:
Dr. James D. Baeder, Chair/Advisor
Dr. Anubhav Datta
Dr. Kenneth Yu
Dr. Howard Elman
Dr. James Duncan, Dean's Representative

To my parents, Kamlesh Jain and Sunita Jain, for their immense love and support

and to my wife Aanchal without whom none of my success would be possible.

Acknowledgments

I owe my gratitude to all the people who have made this thesis possible and because of whom my graduate experience has been one that I will cherish forever. First and foremost, I would like to express my sincere gratitude to my advisor Dr. James Baeder for his continuous support of my Ph.D. study, for his patience, motivation, enthusiasm, and immense knowledge. His guidance and encouragement helped me through the highs and lows during the research and allowed me to grow as a research scientist. It has been a pleasure to work with and learn from such an extraordinary individual. I also wish to thank the members of my dissertation and oral exam committee: Dr. James Duncan, Dr. Howard Elman, Dr. Anubhav Datta, Dr. Kenneth Yu, Dr. Inderjit Chopra, and Dr. Anya Jones for generously offering their time, support, guidance, encouragement and insightful comments.

Next, I would like to acknowledge Joseph Schmaus and Taran for their invaluable help and guidance that led me to complete the comprehensive exam and ultimately the Ph.D. I am grateful for the many friends I have made at Maryland through the years: Yong Su, Mathieu, Harinder, Bumseok, Seung Joon, Bharath, Dylan, Brother Marius, Ben, Brahma, Prakhar, Salil, Rohit, Shashi, Sebastian, Shivaji, Debo, Ananth, and James. They extended their support in a very special way, and I gained a lot from them, through their personal and scholarly interactions while having some great times. It is impossible to remember all, and I apologize to those I've inadvertently left out. Sincere thanks to Tom Hurst who is always ready to provide timely help whenever required.

I owe my deepest thanks to my family - my mother, father and my sister Sonia who have always stood by me and guided me through my career, and have pulled me through against impossible odds at times. Words cannot express the gratitude I owe them. Special thanks to my in-laws for their countless blessings and heartfelt prayers.

Last, but not least, I owe my deepest gratitude towards the love of my life Aanchal for her eternal support and understanding of my goals and aspirations. Her infallible love and support have always been my strength. Her patience and sacrifice will remain my inspiration throughout my life. Without her help, I would not have been able to complete much of what I have done.

Table of Contents

List of Figures

Nomenclature

a	Speed of sound $= \sqrt{\gamma RT}$
C_d	Sectional drag coefficient $= \frac{D}{\frac{1}{2}\rho_\infty U_\infty^2 c}$
C_f	Skin friction coefficient $= \frac{\tau_w}{\frac{1}{2}\rho_\infty U_\infty^2}$
C_l	Sectional lift coefficient $= \frac{L}{\frac{1}{2}\rho_\infty U_\infty^2 c}$
C_p	Pressure coefficient $= \frac{p-p_\infty}{\frac{1}{2}\rho_\infty U_\infty^2}$
d	Nearest wall distance
D	Drag force
e	Internal energy
k	Turbulent kinetic energy $= \frac{1}{2}\left[\overline{(u')^2} + \overline{(v')^2 + \overline{(w')^2}}\right]$
L	Reference length / Lift force
M	Mach number
p	Static pressure
Pr	Prandtl number
Re	Reynolds number $= \frac{\rho_\infty U_\infty L}{\mu_\infty}$
Re_θ	Reynolds number based on momentum thickness $= \frac{\rho_\infty U_\infty \theta}{\mu_\infty}$
S	Strain rate magnitude
t	Time
T	Roror thrust
Tu_∞	Freestream turbulence intensity $= \frac{\sqrt{2k/3}}{U_\infty}$
u, v, w	Flow velocity components along Cartesian coordinate directions
u', v', w'	Turbulent fluctuation velocities along Cartesian coordinate directions
$\overline{u_i' u_j'}$	Time-average of Reynolds stress tensor components
U_∞	Total freestream velocity magnitude
U_e	Boundary layer edge velocity magnitude
x, y, z	Cartesian coordinate directions

Symbols

δ	Boundary layer thickness
γ	Ratio of specific heats / Intermittency
μ	Molecular viscosity
μ_t	Turbulent/Eddy viscosity
ν	Kinematic viscosity $= \frac{\mu}{\rho}$
ω	Specific dissipation rate
Ω	Vorticity magnitude
ρ	Density
τ_w	Wall shear stress
θ	Momentum thickness

Subscripts

e	Boundary layer edge
s	Streamline direction
v	Viscous quantities
∞	Freestream flow variables

Abbreviations

APG	Adverse Pressure Gradient
$DDES$	Delayed Detached Eddy Simulation
DES	Detached Eddy Simulation
LES	Large Eddy Simulation
MSD	Modeled Stress Depletion
$RANS$	Reynolds Averaged Navier-Stokes
SA	Spalart-Allmaras
SSM	Shur-Scotti-Min
$WMLES$	Wall Modeled Large Eddy Simulation
DNS	Direct Numerical Simulation
$MUSCL$	Monotone Upstream-centered Schemes for Conservation Laws
$OverTURNS$	Overset Transonic Unsteady Rotor Navier-Stokes

Chapter 1

Introduction

Helicopters are widely used for civilian and military applications due to their unique ability to take-off and land vertically. They exhibit highly unsteady and complex flow field and as a result, face many design challenges. This chapter describes the operating conditions of helicopters, gives an overview of complex flow physics associated with them and defines the objectives of this thesis.

1.1 Rotorcraft operation

Hovering flight

As shown in figure 1.1a, in hovering flight, the rotor blades have a constant angle of attack with the airflow throughout the azimuth, with 180° defined as the forward direction of the helicopter. The speed of the relative airflow of a blade section due to

rotor blade rotation, U_{rot}, given by

$$U_{rot} = r\Omega \tag{1.1}$$

where Ω is the rotational speed of the blade and r is the radial distance of the blade section from the hub. The rotation of the rotor subject the blades to a number of forces which affect their behavior.

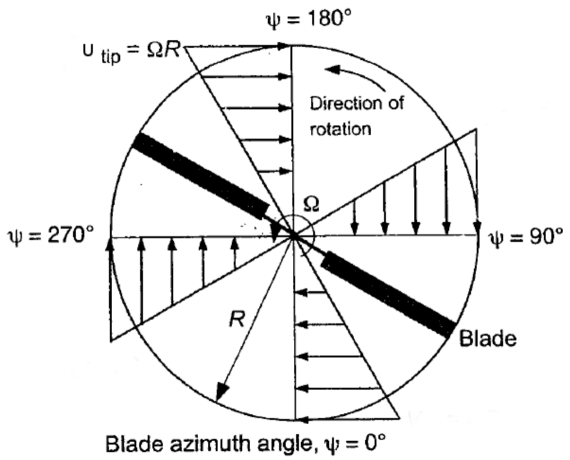

(a)

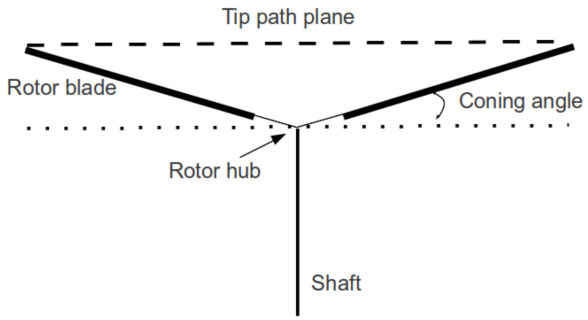

(b)

Figure 1.1: (a) Top view of rotor disk showing the distribution of incident velocity in hovering flight, reproduced from [3]. (b) Side view of rotor blades showing coning angle and tip path plane. Reproduced from [3].

The lift force generated by the rotor tends to draw the blade upward, at a coning

angle, which places the tip path plane above the rotor hub as shown in figure 1.1b. The drag force on the blades causes the tip of the blade to lag slightly behind the root of the blade in azimuth angle. The centrifugal force or inertia of the rotating blades tend to counteract the coning and lag forces. Note that helicopter rotors feature a "rotor hub" to allow for these type of motion via hinges or flexures.

Forward Flight

Forward flight at a speed of U_∞ adds a component of velocity that varies as a function of azimuth in the frame of the rotating blade element, as shown in figure 1.2.

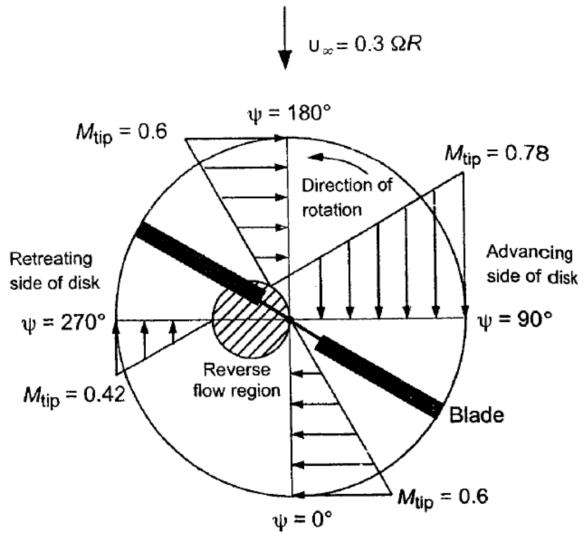

Figure 1.2: Top-view of rotor blades showing the distribution of incident velocity as a function of azimuth ψ in forward flight. Reproduced from [3].

The forward flight speed is given by

$$U_{fwd} = U_\infty sin\psi = U_\infty sin\Omega t \tag{1.2}$$

where the azimuth of rotation ψ is given by the product of the rotor blade rotational

speed Ω and time t. The sum of both the rotational and forward speed components gives the resultant airflow, which in the reference frame of the rotor blade is given by

$$U = U_{fwd} + U_{rot} = U_{\infty} sin(\psi) + \Omega r \tag{1.3}$$

The forward flight speed of a helicopter is typically expressed by the non-dimensional parameter called "advance ratio", which is the ratio of the aircraft's forward flight speed to the blade tip speed, U_{TIP}, i.e.

$$\mu = \frac{U_{\infty}}{U_{TIP}} = \frac{U_{\infty}}{R\Omega} \tag{1.4}$$

Advance ratio is a very important parameter for helicopters and is indicative of the size of the reversed flow region on helicopter blades in forward flight. In figure 1.2, the reverse flow region is a circle and the diameter of this circle is equal to the product μR. Typical advance ratios for helicopters range between $0.2 - 0.4$ in cruise, which means that $20 - 40\%$ of the blade does not generate lift at $\psi = 270°$, since it experiences reversed flow. But as the advance ratio increases, complex flow phenomena begin to appear on on the advancing and retreating side of the rotor disk. The advancing blades may experience transonic effects including shock waves due to the relative high-speed airflow whereas the retreating blades will see reversed flow. The asymmetry in lift between advancing and retreating side will also continue to increase with increase in advancing ratio. This asymmetry in lift is generally addressed by introducing a periodic change of the angle of attack throughout the azimuth such that the blade is now operating at high angle of attack on the retreating side. This results in dynamic stall where the flow over the blade on the retreating side remains attached beyond the

static stall angle, leading to a temporary increase in both lift and pitching moment until they both stall sharply at the point of dynamic stall. Detailed mechanism of dynamic stall is discussed in the next section.

1.2 Background

1.2.1 Static Stall

Consider a typical airfoil section of a helicopter rotor blade as shown in figure 1.3. The flow remains attached when the angle of attack is small. As the angle of attack is increased quasi-statically, there comes a limit beyond which the flow separates completely from the suction side of the airfoil. The event of complete flow separation is called static stall and it drastically reduces the lift generated by the airfoil when it occurs.

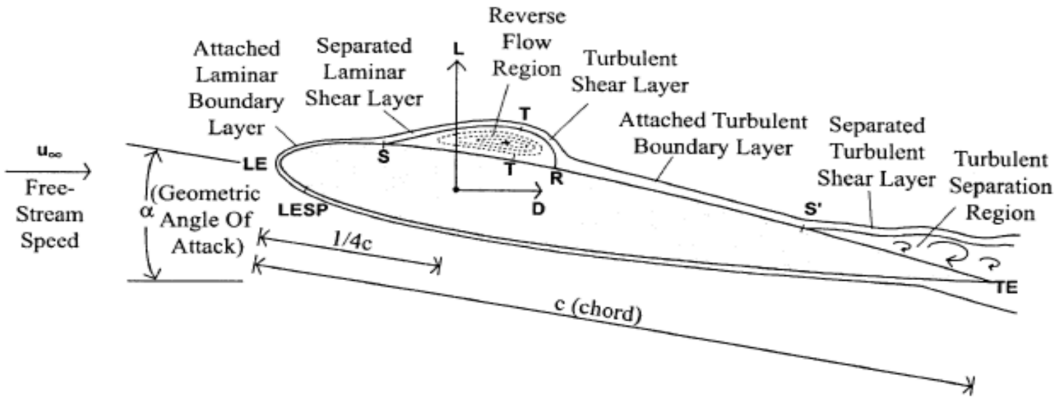

Figure 1.3: Flow features over a typical airfoil section as the angle of attack increases from 6 degree to near-stall limit. Reproduced from [64].

A static stall occurs in one of the three ways as described by McCullough et al.

[65]. The first type of stall, trailing-edge stall, occurs as the turbulent boundary layer separation point moves upstream with increasing angle of attack. This type of stall is gradual and is indicated when the coefficient of lift reaches a maximum. The second type of stall, leading edge stall, takes place when a strong adverse pressure gradient on the leading edge of the airfoil causes flow separation at the low angle of attack. The boundary layer may reattach, in a turbulence state, forming a laminar separation bubble (LSB).

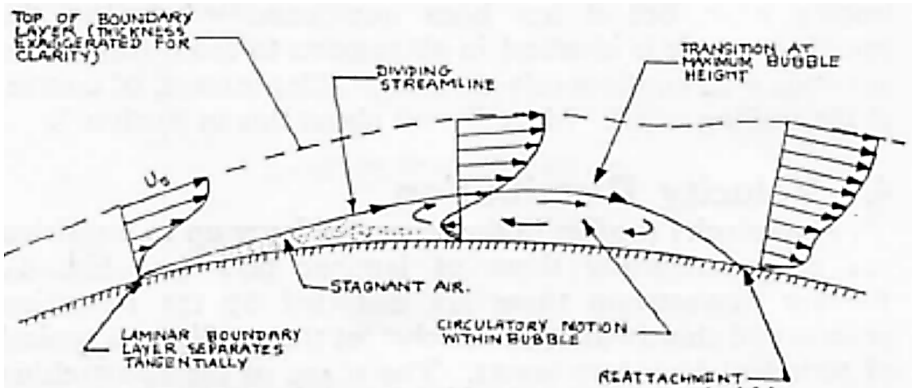

Figure 1.4: Airflow around the laminar separation bubble. Reproduced from [67].

The transition takes place at the maximum height of bubble as shown in figure 1.4. Reattachment may also occur in some cases after transition since the turbulent flow is more resistant towards adverse pressure gradient. As the angle of attack increases, this bubble moves forward towards the leading edge until the reattachment of the boundary layer is no longer possible and stall takes place abruptly as the majority of the boundary layer separates at once. The third mechanism of the static stall is the thin airfoil stall, where a long laminar separation bubble is formed and the reattachment point moves aft with increasing angle of attack until reattachment fails

to take place. At that point, the stall occurs.

1.2.2 Dynamic Stall

Nature of dynamic stall is quite different from that of the static stall as a result of the rapid pitching motion and the increase of the peak angle of attack beyond the static stall limit. This peak angle defines the strength of dynamic stall. As this strength increases, the flow characteristics of dynamic stall differ to a greater extent from those of static stall. A dynamic stall occurs when helicopter rotor blades are at a high advance ratio and a high thrust coefficient such that the angle of attack is high and the speed seen by the retreating rotor blade is low. These conditions are also found on the rotor disk during maneuvers where high blade loading is required such as pull-up or a high-speed diving turn. Bousman [1] observed multiple dynamic stall cycles occurring on the rotor disk during flight tests of UH-60 rotor under high load maneuvers.

The effects of the dynamic stall are more pronounced at higher angles of attack where the blade angle exceeds the static stall angle. Compared to a statically stalling airfoil, Gerontakos [64] observed that boundary layer transition was delayed and progressed upstream more slowly on a dynamically stalling airfoil. The presence of the LSB was observed, consistent with static stall behavior. It was also observed that the boundary layer was thinner, and flow reversal was delayed to the larger angle of attack most likely attributed to the dynamic motion. Different regimes of flow exist in a dynamic stall phenomenon depending on the maximum angle of attack attained.

Attached Flow

When the maximum angle of attack, α_{max}, is below the static stall angle, α_{ss}, flow remains attached throughout the motion, and hysteresis and aerodynamic loads do not differ significantly from static values.

Light Stall

Light dynamic stall takes place when the maximum airfoil angle of attack exceeds the static stall angle i.e. the angle of attack reaches its maximum before the onset of stall, and the change in pitch direction causes the shedding of the leading edge vortex (LEV) [66]. A thin layer of reversed flow may be present over the airfoil, lifting the boundary layer from the surface – however, the boundary layer continues to follow the airfoil curvature and therefore the flow is not considered to be separated. As a result, the presence of reverse flow is not always indicative of flow separation, unlike with static stall where they always coincide, as shown in Figure 1.5[9]. At the top of the upstroke, deceleration of the airfoil causes the formation of LEV, also referred to as the dynamic stall vortex. This vortex is the defining feature of the dynamic stall and a key difference between dynamic and static stall. The downstroke motion causes a smaller separation region and weaker LEV than in the deep stall case, as discussed below. McCroskey et al. [2] determined that the mechanism of dynamic stall and LEV generation is rapid turbulent boundary layer separation and not separation due to the LSB.

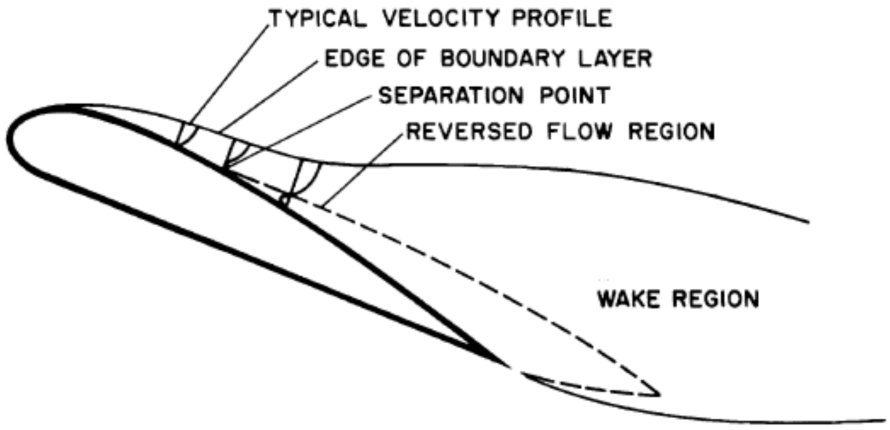

(a)

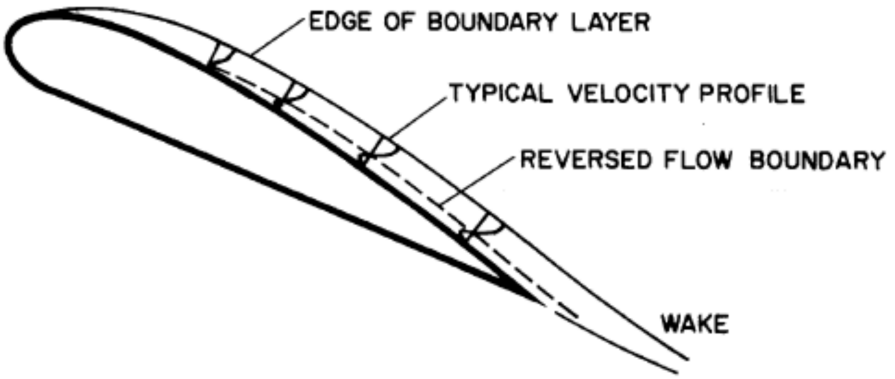

(b)

Figure 1.5: Comparison of reverse flow conditions over (a) static and (b) unsteady airfoils. Reproduced from [9].

The LEV grows and is convected downstream over the airfoil upper surface, creating hysteresis and leading to increase in the aerodynamic loads, and importantly nose-down pitching moment. The resultant effect is a favorable increase in lift generated and the attached flow maximum angle of attack, but several unfavorable effects including high torsional blade loading, blade vibration, and large pitch link loads associated with the pitching moment. Such high loads can exceed fatigue or endurance

limits of components, making dynamic stall a design condition which effectively limits helicopter's forward speed, as shown in Figure 1.6.

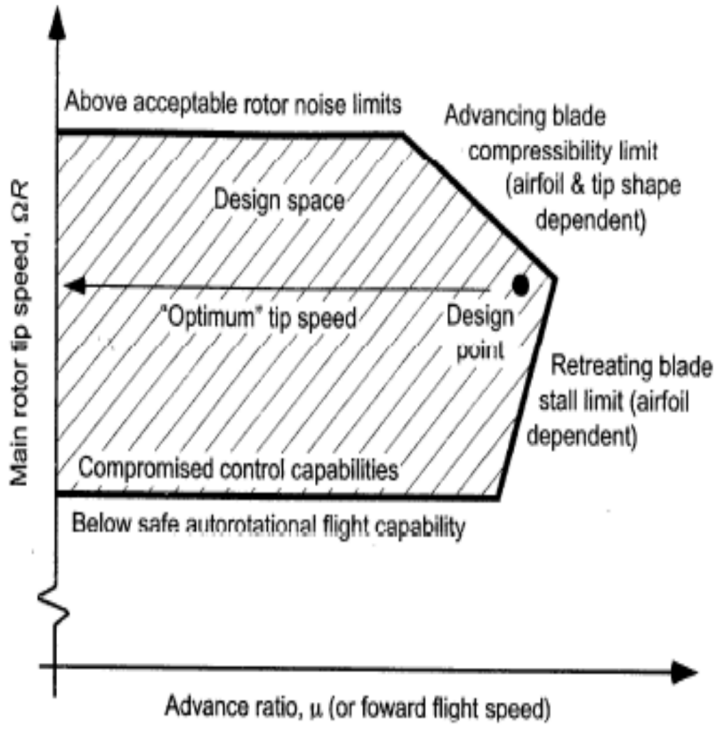

Figure 1.6: Helicopter design constraints on forward speed and main rotor tip speed. Reproduced from [3].

Deep Stall

When the maximum airfoil pitch angle exceeds the static stall angle by a greater margin than light stall, the onset of stall typically occurs prior to reaching the maximum angle of attack, and deep dynamic stall is said to take place [66]. With increasing angle of attack, a stronger LEV is formed than in the light stall case, magnifying the effects of light stall: increasing the aerodynamic load peaks, delaying stall to a higher angle of attack, and increased loads loop hysteresis. Dynamic stall is a complex phe-

nomenon whose behavior is influenced by the Mach and Reynolds number, frequency and magnitude of airfoil pitch oscillation, and the three-dimensional effects in which dynamic stall is native. Due to the complexities of modeling all of these effects, either experimentally or numerically, modeling and simulation of this phenomenon have mostly been confined to simplified conditions.

1.2.3 Mechanism of Dynamic Stall

Dynamic stall behavior is far more complex than the stall behavior of a static airfoil. A great deal of analytical, experimental, and numerical studies have been conducted to study its effects. Leishman [3] describes the dynamic stall process as having five stages and highlights the key events defining the phenomenon, as illustrated in figure 1.7. Thorough descriptions of the dynamic stall are also discussed by McCroskey [4, 5], McCroskey et al. [6], Carr et al. [7] and McAlister et al. [8].

In stage one, dynamic stall begins as the angle of attack exceeds the static stall angle of the airfoil (a in figure 1.7). The rapid pitch-up motion of the airfoil delays the onset of boundary layer separation to higher angles of attack, including angles beyond α_{ss} under certain conditions. The delay in the onset of boundary layer separation is caused by three unsteady effects. First, there is a reduction in the adverse pressure gradient on the suction surface compared to a static airfoil at the same angle of attack. This reduction is caused due to the kinematics of the positive pitch rate, known as the induced camber. Second, the time-varying angle of attack sheds circulation from the trailing edge of the airfoil, decreasing the adverse pressure gradient on the suction

surface and as a result, the lift generated by the airfoil. Third, external pressure gradients cause unsteady effects in the boundary layer including reverse flow prior to flow separation, which delays the onset of stall. The delay in flow separation causes a desirable increase in lift, however, this comes at a cost of less desirable effects in the later stages of dynamic stall. Unlike static stall, where the lift and moment stalls occur simultaneously, in dynamic stall the pitching moment stall occurs first and is followed by the lift stall at the higher angle of attack.

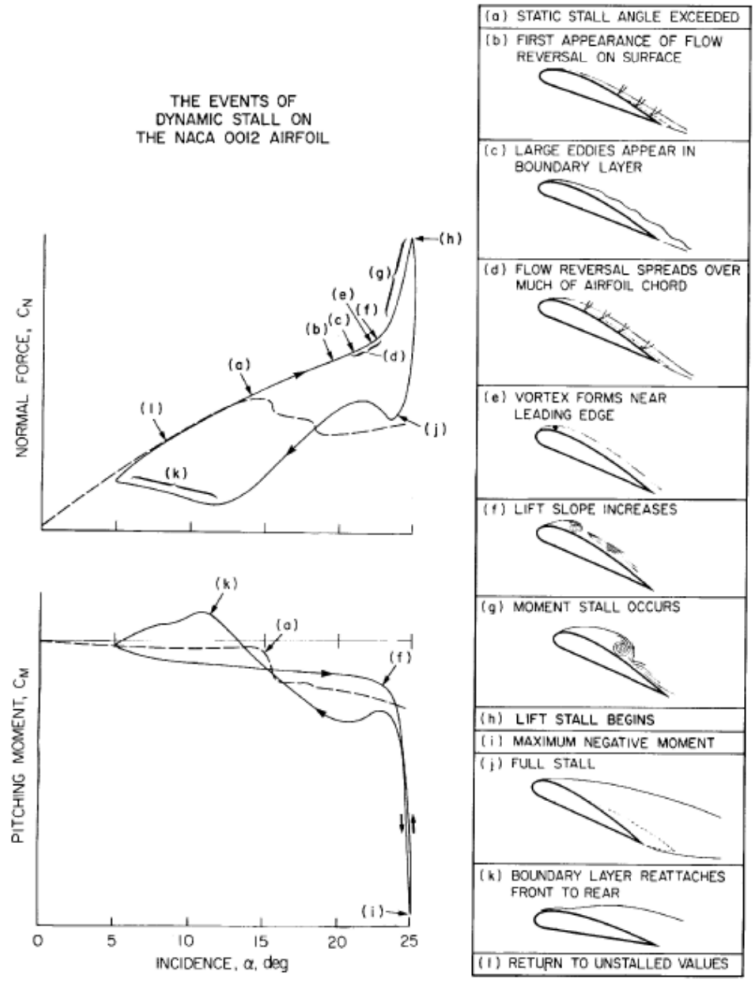

Figure 1.7: Dynamic Stall Events on the NACA 0012 Airfoil. Reproduced from [7].

The second stage (b-d in figure 1.7) begins as a shear layer forms downstream of the leading edge where high adverse pressure gradients cause flow separation to take place. The shear layer then forms a vortex that is shed from the leading edge region of the airfoil (e), also known as the Leading Edge Vortex (LEV). The LEV reduces the pressure on the upper surface of the airfoil increasing lift beyond what is created by a static airfoil at the same angles of attack and delaying separation to higher angles of attack. Carr [7] observed an increase in the lift-curve slope (f in figure 1.7) following the formation of LEV. This increase in lift is accompanied by a significant increase in nose-down pitching moment, the moment stall (g in figure 1.7), resulting from the center of pressure moving aft as the LEV is convected downstream. The effect of the nose-down pitching moment result as high torsional air loads on the blade, which may also introduce aeroelastic problems such as stall flutter.

The third stage starts when the LEV is convected over the airfoil and into its wake, resulting in the peak lift value (h in figure 1.7) followed by the drastic loss of lift and surged values of pitching moment and drag associated with lift stall (i in figure 1.7). There is also a loss of dynamic lift associated with dynamic stall, though this effect is not as significant as that of the pitching moment. As the clockwise rotating LEV is shed from the leading edge an anti-clockwise rotating trailing-edge vortex (TEV) is generated as a result of the low pressure of the LEV. As the LEV convects downstream, the TEV becomes stronger and grows in size causing a second suction peak over the trailing edge of the airfoil that contributes significantly to the negative pitching moment. The LEV convects away from the surface of the airfoil and over the TEV as it moves beyond the trailing edge of the airfoil.

In stage four, the LEV becomes entrained in the turbulent wake downstream of the airfoil, and the flow on the upper surface of the airfoil reaches to a state of full separation (j in figure 1.7). When the airfoil is fully stalled, it behaves as a bluff body and the flow becomes independent of the airfoil and becomes solely a function of free-stream.

In stage five, the flow re-attaches at low angles of attack, well below the normal static stall angle. It was observed that reattachment followed a high rate of decrease in suction. Leishman [3] explained that the lag in reattachment is caused by an induced camber effect on the leading edge pressure gradient resulting from the nose-down pitch rate. The lag generates hysteresis loops in the pitch, drag and lift; these loops are the source of reduced aerodynamic damping, which can lead to aeroelastic problems on the rotor such as stall flutter [3]. Flutter is a dynamic aeroelastic effect resulting in divergent oscillations caused by positive feedback between aerodynamic loads and the blade's elastic structure. When flutter occurs on an aircraft, the loads can quickly increase to the point of being catastrophic to the aircraft structure. In a helicopter, it is the pitch links that control the angle of attack of the rotor blades and are exposed to failure under conditions of stall flutter. If the oscillations are caused by flow separation, the phenomenon is called stall flutter.

Figure 1.8 illustrates the hysteresis loops as a function of the depth of dynamic stall. In attached flow, $\alpha_{max} < \alpha_{ss}$, damping is positive and the counter-clockwise loop increases in size as α_{avg} increases toward α_{ss}. As α_{max} begins to exceed α_{ss} indicating the onset of light stall, second loop forms in the $C_M - \alpha$ curve. Overall damping is reduced as this negative damping second loop grows in size with increasing depth of

light stall when damping can become negative [3]. As α_{max} continues to increase into the deep stall regime, the peak moment occurs before the maximum angle of attack causing a third counterclockwise loop to appear in the $C_M - \alpha$ curve, increasing the damping as the depth of stall increases further. The amount of aerodynamic damping can be modified by changing the average angle of attack, the reduced frequency and the type of motion, as discussed in the next section.

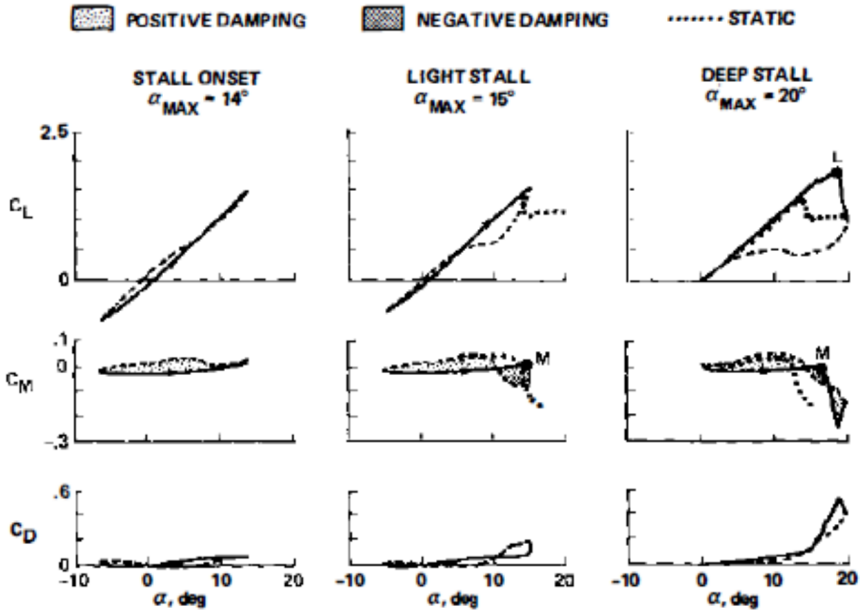

Figure 1.8: Unsteady airloads at various depths of dynamic stall, M = 0.3, $\alpha = \alpha_0 + 10°cos(\Omega t)$, $k = 0.1$ $\alpha_0 = 4°, 5°, 10°$. Reproduced from [5].

1.2.4 Factors effecting Dynamic Stall

This section discusses relevant parameters pertaining to the flow-field and the geometry that have a significant impact on the dynamic stall. It is important to note that these parameters do not have an effect on the sequence of events in the stages of dynamic stall described above, but may affect attributes such as the onset of flow

separation, the depth of stall, and air load peak magnitudes.

Airfoil Shape

Experiments by Carr et al. [7], and McCroskey et al. [6] have shown that differences in airfoil shapes can significantly change the loads but have little influence over the mechanism of dynamic stall. Leishman [3] illustrated further that the effect of airfoil shape influences the timing of the moment stall and the depth of the moment break at moment stall. In the current work, the NACA0012 airfoil is used for validation studies because of the widely available results in literature for the airfoil. The main focus, however, is on SC1095 and VR-12 airfoils because of the relevance of these airfoils to helicopter rotor blade applications. These airfoils are suited because of their good compromise between high Cl_{max}, low pitching moment and high drag divergence Mach number.

Three-Dimensional Effects

Dynamic stall is a 3D phenomenon which occurs over different parts of the blade at different azimuth angles making the resulting flow very complicated, with more complex flow structures than 2D flow can model. Three-dimensional effects include rotor blade sweep effects, the blade tip vortex, blade-vortex interaction and interference of the helicopter non-rotor blade wake. A sweep angle is imparted on the flow by centrifugal effects caused by blade rotation, the Mach number gradient across the rotor blade span, and the component of the forward airspeed parallel to the rotor blade. These combined effects may cause a significant radial component of the relative wind

velocity, resulting in a local sweep angle [3]. Leishman [3] described that cross-flow conditions combined with high angle of attack of the blade section have favorable effects on the spanwise development of the boundary layer, which tends to delay the onset of flow separation to higher angles of attack and reduce the strength of the LEV producing much higher lift coefficients and promoting flow reattachment on the down stroke. Near the blade tip, the tip vortex effectively reduces the angle of attack, causing a gradual reduction in lift curve slope along with a decrease in the depth of dynamic stall [68].

Blade-vortex interaction (BVI) occurs due to the rotor blades interacting with the wakes of other blades during rotation, and represent another field of research due to the complexities involved in that phenomenon. Modeling of BVI requires complete helicopter rotor to be modeled and is not viable for the turbulence focused study considered in this research. Note that the wake of the remainder of the helicopter, including fuselage and rotor hub and also interaction between the main rotor blades and tail rotor vortices, is out of the scope of the current work.

Reynolds Number Similarity

The Reynolds number, the ratio of inertial to viscous forces, is given by

$$Re = \frac{Uc}{\nu} = \frac{\rho U c}{\mu} \tag{1.5}$$

Where c is the airfoil chord, and μ and ν are the dynamic and kinematic viscosity of the fluid, respectively. Martin et al. [70] found that increase in Reynolds number caused the increase in peak lift and pitching moment magnitudes and delays in

the dynamic stall. The Reynolds number influences the formation of LSB (laminar separation bubble). Sharma and Poddar [69] identified that increasing the Reynolds number reduced the size of the LSB, shifted the boundary layer transition closer to the separation point and also shifted the reattachment point upstream. These observations have consequences for the boundary layer and LSB. However, the LSB has been shown to have minimal impact on the aerodynamic loads at flight Reynolds number [7]. McCroskey et al. [6], and Carr et al. [7] also found that the mechanism of the dynamic stall (i.e., the formation of the LEV) is largely independent of Reynolds number.

Boundary Layer Transition

Leishman [3] emphasized that accurate prediction of boundary layer transition is a key challenge towards the prediction of dynamic stall. Barla et al. [71] also suggested that transition effects have substantial effects on unsteady flow characteristics. Ekaterinaris and Menter [72] also found that transition modeling may have an important effect on simulated data, and noticed improvements when even simple transition modeling was used. McCroskey et al. [6] and Carr et al. [7] studied airfoils with both clean and tripped boundary layers and found that the time-history of the breakdown of the leading-edge flow and aerodynamic loads, and the stall angle were affected by the state of the boundary layer and the presence of an LSB. They were also observed that the onset of the stall was more irregular in the presence of a boundary layer trip.

Compressibility Effects

The Mach number in compressible flow is given by

$$M = \frac{U}{a} = \frac{U}{\sqrt{\gamma RT}} \tag{1.6}$$

where a is the speed of sound, γ is the ratio of specific heats, R is the specific gas constant and T is the temperature. A dynamic stall occurs over a range of Mach numbers, from below 0.3 for the first cycle to over 0.8 for the third cycle [1]. Compressibility effects appear for Mach numbers as low as 0.2-0.3. Leishman [3] indicated that qualitative features of dynamic stall do not change significantly over a range of Mach numbers, but there are variations in the quantitative behavior. Carr and Chandrasekhara [73] explained that the physics of the stall process can change significantly between low and high Mach numbers. They also showed that as Mach number increases, the magnitude of the critical adverse pressure gradient is reduced, promoting flow separation, LEV formation, and dynamic stall to lower angles of attack, thereby reducing LEV strength and C_{lmax}. At higher Mach numbers, shock waves near the leading edge can cause flow separation to take place and increase the complexity of center of pressure behavior during boundary layer separation and reattachment [3]. Bowles et al. [74] conducted a time-resolved analysis of the pitching moment recorded from experiment and showed that there was negative damping during the pitch-up motion at low reduced frequencies and compressible Mach numbers.

Pitching amplitude

The maximum angle of attack obtained from the combination of the mean and oscillatory amplitudes has to influence on the depth of stall, moving from attached flow to light and finally deep stall as the maximum angle of attack increases. Lee and Gerontakos [76] found that the peak aerodynamic loads did not change significantly as a function of oscillation amplitude if the maximum angle of the attack remained constant. The influence of the mean angle of attack on torsional damping depends greatly on the stall regime. In attached flow, increasing the mean angle of attack increases positive damping. Once light stall begins, increasing the angle of attack decreases damping. At the onset of deep stall, damping increases with an increase in angle of attack.

Pitching frequency

The frequency of oscillation of the airfoil is one of the most significant parameters affecting dynamic stall [8] and is measured by the dimensionless parameter known as reduced frequency, a measure of unsteadiness of a motion, which is given by

$$k = \frac{\Omega c}{2U} \tag{1.7}$$

where Ω is the rotational frequency of the airfoil. Airflow is steady at $k = 0$ and becomes increasingly unsteady as k is increased. Dynamic stall begins to occur outside of the quasi-steady regime, defined as $k < 0.05$ [3].

The pitching motion of the airfoil influences dynamic stall by inducing a linear distribution of velocity normal to the chord. The effect of the linear distribution is

known as induced camber, which delays dynamic stall formation [3]. An increase in the reduced frequency will delay the onset of stall due to an increase in the magnitude of the critical adverse pressure gradient and reduce flow separation. This leads to increase in peak load magnitudes, hysteresis and dynamic stall angles. Increased reduced frequency also delays the formation and shedding of the LEV and flow reattachment. Martin et al. [70] observed through experimental testing that the LEV shedding occurred at α_{max} for low-amplitude, high-frequency oscillations. This emphasizes the importance of accurately modeling the pitch rate in any research on the dynamic stall.

1.3 Numerical Modeling of Dynamic Stall

Because of the inherent challenges of experimental testing of dynamic stall, extensive numerical studies of dynamic stall have been performed, though these are not without their challenges either. Dynamic stall aerodynamic load predictions are used in comprehensive rotor analysis, and are generated using a variety of methods. Theoretical, semi-empirical and CFD approaches such as unsteady Reynolds-averaged Navier–Stokes (RANS), Large-Eddy Simulation (LES) and Hybrid RANS-LES approaches have been used to study the phenomenon.

1.3.1 Comprehensive Rotor Analysis

Comprehensive rotor analysis combines aerodynamic, structural, dynamic and aeroelastic models to calculate performance, loading and vibration characteristics of a he-

licopter. These analyses require the coupling of many models, and to be of practical use the computational expense must be reasonable. Traditionally, to avoid expensive CFD computations, the aerodynamic models under this analysis make use of lookup tables of 2D airfoil data, corrected for unsteady aerodynamics. Corrections for dynamic stall are carried out using semi-empirical models discussed in the next section.

An important example of comprehensive rotor analysis is the Comprehensive Analytical Model of Rotorcraft Aerodynamics and Dynamics (CAMRAD) II [75]. It comprises of aerodynamic models which use blade element momentum theory (BEMT) to determine loads of a rotating system of rotor blades. BEMT is a combination of momentum theory and blade element theory. Momentum theory, proposed by Glauert [77], treats the blade rotor system as a single disk with a pressure difference across it and is useful as a first approximation for thrust and rotor power. However, it does not consider the local effects on each blade. Blade element theory is useful for blade design. It assumes that a rotor blade can be modeled as a series of 2D airfoil sections, accounting for 3D effects by applying empirical factors, and integrating the loads over the blade span [3]. The combination of these two theories is BEMT which models the inflow by dividing the rotor disk into a series of concentric annuli and applying conservation equations to each annulus.

1.3.2 Analytical and Semi-Empirical Approaches

Theodorsen [78] started developing the underlying theory of dynamic stall using potential flow theory and the Kutta condition. Equations were developed for both lift and pitching moment, each with circulatory and non-circulatory components. The non-circulatory terms represent flow acceleration, and the circulatory terms represent the influence of the shed wake. McCroskey and Philippe [79] pointed out that this theory is applicable only to thin airfoil small amplitude oscillations since the viscous effects (flow reversal in boundary layer and formation of the LEV) that are relevant in the dynamic stall are not considered.

Leishman [3] has contributed significantly to the development of indicial methods, based on the linearization of the flow as a function of the forcing condition. An indicial function models unsteady flow as a series of step function disturbances. This method does not apply well to compressible or separated flow in its original form. Jose et al. [81] improved the method and extended its applicability to unsteady compressible flows and also allowing combined pitching and free-stream oscillations. The improved method is limited to speeds below the critical Mach number and $k < 0.4$. Since indicial methods use superposition of linear terms, they are not able to model the post-stall period of dynamic stall, which is highly influenced by separated flow.

One of the dynamic stall models used by the CAMRAD II aeromechanical analysis is the Leishman–Beddoes [82] model. This model uses unsteady thin airfoil theory to determine the unsteady attached flow loading which is linear in nature. The nonlinear loads are determined from modeling of separated flow using Kirchoff-Helmholtz

theory, which determines lift as a function of an angle of attack and the flow separation point [3]. The effects of LEV during dynamic stall are considered by modeling its formation, as a function of the leading edge pressure and Mach number, and convection over the chord and into the wake. The semi-empirical models allow for computationally inexpensive determination of aerodynamic loads which is very useful for fluid-structure interaction modeling when coupled with a BEM model. However, because of the linear behavior assumption, these models suffer in accuracy specifically shock waves and separated flow. Despite these limitations, theoretical models assist in understanding the underlying physics of the phenomenon of dynamic stall.

1.3.3 Numerically Modeling Unsteady Flow field

Since the flight conditions of helicopter rotors are difficult to reproduce experimentally with full inclusion of their nonlinear complexity, numerical solution of the full Navier-Stokes equations is another approach to completely model the behavior of dynamic stall. However, the computational expense associated with the brute force CFD approach such as DNS (Direct Numerical Simulation) has led researchers to find a less expensive numerical framework for predicting dynamic stall. It is usually not feasible for a single numerical methodology to accurately measure different flow conditions such as flow reversal and flow separation of varying extent. Modeling the aerodynamic behavior of airfoil in a wide range of angles of attack starting from low values and leading up to the stall event is challenging for CFD because of the varied flow physics.

RANS approach

Given the importance of turbulence in unsteady flow, several researchers have investigated different turbulence models integrated with classical Reynolds-averaged Navier-Stokes (RANS) approach to obtain predictions for the static and dynamic stall. RANS model equations are the time-averaged form of the Navier–Stokes equation. They do not resolve turbulent flow structures but model the flow in terms of mean and universal turbulence scales. Any high-frequency transient features in the flow are lost during the process of time averaging when RANS model is used. The RANS approach is computationally inexpensive and works well for attached flow at low angles of attack when there is minimal adverse pressure gradient resisting the boundary layer. The attached boundary layer does not contain turbulent vortical disturbances and flow has no disturbances in the span-wise direction either [84].

Ko and McCroskey [83] tested the Baldwin-Lomax, Spalart-Allmaras (SA) and $k-\epsilon$ turbulence models which are respectively zero, one and two equation models alongside RANS approach. The test case comprised of an NACA0015 airfoil oscillating in attached flow, light and deep stall at Mach number 0.3, reduced frequency of 0.1 and Re of 1.95×10^6. It was found that none of the turbulence models performed well during the deep stall, especially on the downstroke. In attached flow and light stall, the SA and $k-\epsilon$ models agreed well. Barla et al. [71] also conducted dynamic stall simulations and found that the SA model provided the most reliable results until severe separation took place. Ekaterinaris and Menter [72] studied the performance of one and two-equation turbulence models to predict massively separated flow. They

found that for light stall simulation, SA under-predicted and Baldwin-Barth over-predicted flow separation, while the predictions of SST were better among the three models.

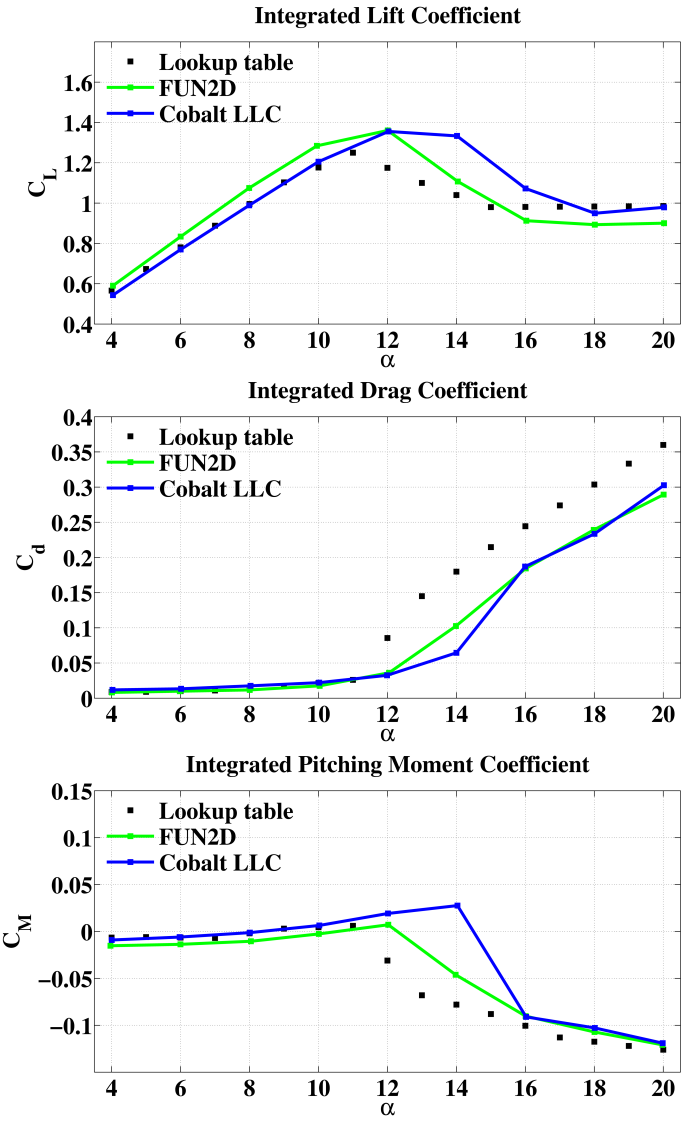

Figure 1.9: Integrated forces predicted by GIT(Cobalt LLC) and AED(FUN2D) data sets from Smith et al. [12] compared with UH-60A lookup table data [11] for SC1095 airfoil.

To get an idea of how RANS based numerical predictions match with experimental

data under static conditions, two exemplary data sets from Smith et al. [12] are compared with the UH-60A lookup table data [11] in Figure 1.9 for the integrated forces. The first data set comprised of simulation results from the CFD code Cobalt LLC from Georgia Institute of Technology (GIT) [13]. The second data set consisted of CFD results from the FUN2D code used by Aviation Engineering Directorate (AED) [14]. When the flow is fully attached ($\alpha \leq 10°$), there is a good agreement between the RANS-based CFD predictions and the lookup table data for integrated lift. As the flow begins to separate at 11° angle of attack due to the adverse pressure gradient, the attached boundary layer gets thicker. Substantial anisotropic turbulent structures enter the outer part of the boundary layer. RANS model simply average out those turbulent structures leading to delay in the predicted onset of stall. As a result, lift is over-predicted along with higher pressure peak. Drag and pitching moment predictions also deviate from experimental data in the range 12°– 15°. From the comparison, it is evident that RANS model performs poorly in the near-stall regime of 11°– 15°.

DNS and LES approach

Unlike RANS model, scale resolving approaches such as DNS (Direct Numerical Simulation) and LES [18] (Large Eddy Simulation) are capable of comprehensively capturing turbulent flows of any complexity. DNS resolves all the temporal and spatial scales of the flow without any modeling/approximation of the flow. This approach is the most accurate numerical representation of the flow but remains prohibitively expensive in terms of the computational resources at practical Reynolds number. LES

also resolves most of the turbulent length scales and is more accurate than RANS model in capturing three-dimensional and unsteady flow features. The predictive power of LES in capturing unsteady physics comes at the price of up to two orders of magnitude increase in the required computational resources [19].

Hybrid RANS-LES approach

The need for higher accuracy at reduced computational resources has led to the development of hybrid RANS-LES methods. Hybrid RANS-LES methods behave as LES in the region where the grid is fine enough to directly resolve the larger eddies and as a RANS model in the region where the grid is too coarse for direct resolution of the eddies. A number of hybrid models have been developed over the past two decades. Among these methods, DES (Detached Eddy Simulation) type hybrid RANS-LES methods have gained considerable importance because of their accuracy in the prediction of flows with separation and their straightforward integration into established turbulence models. DES type methods are non-zonal [20]– they are able to auto-switch between RANS and LES based on the local grid and flow parameters. The first DES type hybrid method which is also called the DES method models the boundary layer using RANS mode and resolves the flow features outside the boundary layer using LES mode. DES method has been shown to perform better than RANS model for flows with massive separation [21].

A number of computational studies have employed RANS, DES and DDES formulations to predict aerodynamic behavior of airfoils at various angles of attack. Smith et al. [33] conducted numerical grid resolution study on two airfoils using RANS and

hybrid RANS-LES methods. Their main objective, however, was to investigate the effects of grid topology on the numerical flow solutions predicted by Hybrid RANS-LES methods. Medida and Baeder [34] conducted the detailed numerical study to obtain static and dynamic stall characteristics using RANS and DES type methods. They found that DDES method was not able to predict the onset of stall accurately and poorly resolved incipient flow separation near the trailing edge.

The turbulence length scale plays a key role in determining the location of the switch and dominantly governs the eddy viscosity production in the boundary layer provided RANS mode is active. The definition of turbulence length scale is open to interpretation and there are few definitions suggested in the literature [35, 36]. By definition, DES type methods impose RANS mode in most of the boundary layer and will also inherit the limitations of RANS model has in capturing flows with the thick boundary layer. For example, under strong adverse pressure gradient, the RANS based Spalart-Allmaras turbulence model predicts excessive modeled turbulence in the outer part of the boundary layer of the flow and makes the boundary layer resistant towards separation [23]. This will cause a hybrid method to also delay the transition from model to resolved turbulence. For such flows, it is important to evaluate length scales for their ability to obtain correct modeled and resolved stresses at the RANS-LES switching interface. Realizing a length scale definition which leads to correct stress predictions within the boundary layer can significantly improve flow prediction accuracy and can capture stall events precisely.

1.4 Objectives

The aim of this thesis is to enhance numerical techniques for predicting separated and stalled flows and to contribute to the understanding of these flows. The technical challenges associated with the numerical analysis of separated flow are realized and the following objectives are accomplished based on this realization:

- DES type hybrid models of varying fidelity are evaluated to accurately resolve the flow at different extents of separation and in a comprehensive angle of attack range. Emphasis is laid on capturing the correct (physical) turbulence near the boundary layer region at the near-stall regime where the lower fidelity models have failed.

- The impact of explicit numerical techniques to account for laminar-turbulent transition [38] and adverse pressure gradient [39] is noted as they are used in conjunction with DES type methods.

- The sensitivity of hybrid RANS-LES methods toward turbulence length scale and anisotropy of grid is investigated. Conventional shielding parameters used in the DDES formulation are also assessed. Based on the analysis, an alternative turbulence length scale is proposed along with suitable shielding function that facilitated highly accurate predictions for weakly separated flows.

- Development of numerical framework is established that resulted computation of highly accurate aerodynamic characteristics of rotorcraft pertinent SC1095 and VR12 airfoils under static and dynamic conditions.

The end result of this work is a high fidelity numerical framework based on hybrid RANS-LES methods and relevant computational techniques that are able to provide precise aerodynamic characteristics of rotorcraft pertinent SC1095 and VR12 airfoils under static and dynamic conditions.

Chapter 2

Numerical Methodology

Simulations were performed using the CPU based Overset Transonic Unsteady Rotor Navier–Stokes (OverTURNS) flow solver [40] and the GPU based unsteady Navier–Stokes solver [43, 44]. Both the solvers share similar numerical capabilities. This chapter details the numerical setup employed by the solvers to conduct detailed Hybrid RANS-LES simulations. At the core, a system of partial differential equations governing unsteady, compressible fluid flow is numerically solved in a Eulerian framework. The final form of the governing equations is obtained through the following sequence of transformations applied to their three-dimensional Cartesian form: (1) Non-dimensionalization, (2) Curvilinear coordinate transformation and (3) Reynolds-averaging. These transformed equations are numerically discretized on a computational domain in both space and time to obtain a system of coupled algebraic equations, which are then solved to obtain the flow field solution.

2.1 Governing equations

The three-dimensional, unsteady, Navier–Stokes equations describe the behavior of fluid flow. In this work, they are used to represent compressible, non-reacting, ideal gas flow across the boundary of a closed domain known as a control volume. They ensure universal laws of conservation of mass, momentum, and energy in the control volume. The Cartesian system of equations in their strong conservation form is given by Eq. 2.1:

$$\frac{\partial Q}{\partial t} + \frac{\partial F_i}{\partial x} + \frac{\partial G_i}{\partial y} + \frac{\partial H_i}{\partial z} = \frac{\partial F_v}{\partial x} + \frac{\partial G_v}{\partial y} + \frac{\partial H_v}{\partial z} + S \tag{2.1}$$

where Q is the vector of conserved variables, F_i,G_i and H_i are the inviscid flux vectors, and F_v,G_v and H_v are the viscous flux vectors. S represents the vector of body forces and accounts for a change in reference frame. The vector of conserved variables, Q, is given by Eq. 2.2:

$$Q = \begin{Bmatrix} \rho \\ \rho u \\ \rho v \\ \rho w \\ E \end{Bmatrix} \tag{2.2}$$

where, ρ is the fluid density, and (u, v, w) are components of the fluid velocity along the Cartesian coordinate system (x, y, z). E is the total energy per unit volume given by:

$$E = \rho \left[e + \frac{1}{2} \left(u^2 + v^2 + w^2 \right) \right] \tag{2.3}$$

here, e is the internal energy per unit mass. The vector of primitive variables is given by (ρ, u, v, w, p). The inviscid and viscous flux vectors are given by Eqs. 2.4–2.9:

$$F_i = \begin{Bmatrix} \rho u \\ \rho u u + p \\ \rho u v \\ \rho u w \\ (E + p)\, u \end{Bmatrix} \tag{2.4}$$

$$G_i = \begin{Bmatrix} \rho v \\ \rho v u \\ \rho v v + p \\ \rho v w \\ (E + p)\, v \end{Bmatrix} \tag{2.5}$$

$$H_i = \begin{Bmatrix} \rho w \\ \rho w u \\ \rho w v \\ \rho w w + p \\ (E + p)\, w \end{Bmatrix} \tag{2.6}$$

$$F_v = \begin{Bmatrix} 0 \\ \tau_{xx} \\ \tau_{yx} \\ \tau_{zx} \\ u\tau_{xx} + v\tau_{yx} + w\tau_{zx} - q_x \end{Bmatrix} \tag{2.7}$$

$$G_v = \begin{Bmatrix} 0 \\ \tau_{xy} \\ \tau_{yy} \\ \tau_{zy} \\ u\tau_{xy} + v\tau_{yy} + w\tau - q_y \end{Bmatrix} \tag{2.8}$$

$$H_v = \begin{Bmatrix} 0 \\ \tau_{xz} \\ \tau_{yz} \\ \tau_{zz} \\ u\tau_{xz} + v\tau_{yz} + w\tau_{zz} - q_z \end{Bmatrix} \tag{2.9}$$

where, q_x, q_y, and q_z are heat conduction terms expressed as a function of temperature (T) and coefficient of thermal conductivity (k) as follows:

$$q_j = k\frac{\partial T}{\partial x_j}\,(j = x, y, z) \tag{2.10}$$

The viscous stress tensor for Newtonian fluids, τ_{ij}, formulated using Stokes' hypothesis [45] is given by:

$$\tau_{ij} = \mu\left[\left(\frac{\partial u_i}{\partial x_j} + \frac{\partial u_i}{\partial x_j}\right) - \frac{2}{3}\frac{\partial u_k}{\partial x_k}\delta_{ij}\right], \quad \delta_{ij} = 1\; if\; i = j;\; \delta_{ij} = 0\; if\; i \neq j \tag{2.11}$$

The coefficient of molecular viscosity is given by Sutherland's formula in Eq. 2.12:

$$\mu = C_1\frac{T^{\frac{3}{2}}}{T + C_2} \tag{2.12}$$

where, $C_1 = 1.4 \times 10^{-6} kg/(ms\sqrt{K})$ and $C_2 = 110.4$ K for air at standard temperature and pressure. To close the system of equations, the equation of state for ideal gas is

used:

$$p = \rho RT \tag{2.13}$$

where R is the gas constant. Since all the flows studied in this work involve air at standard temperature and pressure, the calorically perfect gas assumption is valid. A calorically perfect gas is an ideal gas with constant specific heats. Specific heat at constant volume (c_v) and specific heat at constant pressure (c_p) are given by:

$$c_v = \frac{R}{\gamma - 1}; \qquad c_p = \frac{\gamma R}{\gamma - 1} \tag{2.14}$$

The following relations between thermodynamic quantities are applicable to calorically perfect gases:

$$e = c_v T \tag{2.15}$$

$$p = (\gamma - 1)\rho e \tag{2.16}$$

The total energy per unit volume, E, can now be re-written in terms of pressure, p, and velocity components as follows:

$$E = \frac{p}{\gamma - 1} + \frac{1}{2}\rho\left(u^2 + v^2 + w^2\right) \tag{2.17}$$

In the above equations, the value of the ratio of specific heats (γ) is 1.4 for air at standard temperature and pressure.

2.2 Rotating Reference Frame

When simulating problems with moving bodies, the computational grid is usually translated and rotated based on the path of the solid surface. In such cases, the

governing equations are solved in an inertial frame of reference. This method increases computational time since it requires the calculation of grid-related quantities (such as metrics, surface normals, etc.), and to perform domain connectivity related operations for overset meshes at each time step. To solve the equations in a non-inertial reference frame, the three velocity components (u, v, w) in the convective flux vectors of the governing equations (Eq. 2.4–2.6) are replaced by $(u - u_g, v - v_g, w - w_g)$, where $U_g = (u_g, v_g, w_g) = \Omega \times r$ is the vector of grid velocities due to rotation, and $\Omega = (\Omega_x, \Omega_y, \Omega_z)$ is the angular velocity vector. In addition, Coriolis acceleration terms must be included as a source term vector, S, on the right-hand side of Eq. 2.1 as shown below:

$$S = \begin{Bmatrix} 0 \\ \rho v \Omega_z \\ -\rho v u \Omega_z \\ 0 \\ 0 \end{Bmatrix} \tag{2.18}$$

2.3 Non-dimensional Form of Equations

The governing equations are often solved in their non-dimensional form. There are two advantages of doing this:

1. parameters such as Mach number and Reynolds number can be varied independently,

2. All flow variables are normalized to fall in the vicinity of (0,1), thereby reducing numerical inaccuracies that may occur due to mathematical operations between

largely different values.

All independent and dependent variables are non-dimensionalized using a set of reference variables indicated by the $*$ superscript in the equations given below:

$$x* = \frac{x}{L}, \qquad y* = \frac{y}{L}, \qquad z* = \frac{z}{L}, \qquad t* = \frac{t}{{}^{L}/_{a_\infty}} \tag{2.19}$$

$$u* = \frac{u}{a_\infty}, \qquad v* = \frac{v}{a_\infty}, \qquad w* = \frac{w}{a_\infty}, \qquad \mu* = \frac{\mu}{\mu_\infty} \tag{2.20}$$

$$\rho* = \frac{\rho}{\rho_\infty}, \qquad p* = \frac{p}{p_\infty a_\infty^2}, \qquad T* = \frac{T}{T_\infty} \tag{2.21}$$

For problems involving airfoil sections, the chord length of the airfoil is chosen as the reference length, L. Substituting the above relations into the governing equations in Eq. 2.1 gives a new set of equations in terms of the non-dimensional variables. The non-dimensional equations are identical in form to the dimensional equations except for the viscous stress tensor and thermal conduction terms. Modified viscous stress tensor and heat conduction terms are given below:

$$\tau_{ij} = \frac{\mu M_\infty}{Re_\infty} \mu \left[\left(\frac{\partial u_i}{\partial x_j} + \frac{\partial u_j}{\partial x_i} \right) - \frac{2}{3} \frac{\partial u_k}{\partial x_k} \delta_{ij} \right] \tag{2.22}$$

$$q_j = -\frac{\mu M_\infty}{Re_\infty Pr(\gamma - 1)} \frac{\partial T}{\partial x_j} \tag{2.23}$$

All independent and dependent variables in the above two equations are non-dimensional, and the superscript $*$ representation is not used. The new non-dimensional parameters that are formed as a result of non-dimensionalization are given below:

$$Reynolds\ number: \ Re_\infty = \frac{\rho_\infty V_\infty L}{\mu_\infty} \tag{2.24}$$

$$Mach: \ M = \frac{V_\infty L}{a_\infty} \tag{2.25}$$

$$Prandtl\ Number:\ Pr = \frac{\mu c_p}{k} \tag{2.26}$$

For air at standard temperature and pressure, the Prandtl number, $Pr = 0.72$. V_∞ is the free-stream velocity magnitude given by $\sqrt{u_\infty^2 + v_\infty^2 + w_\infty^2}$.

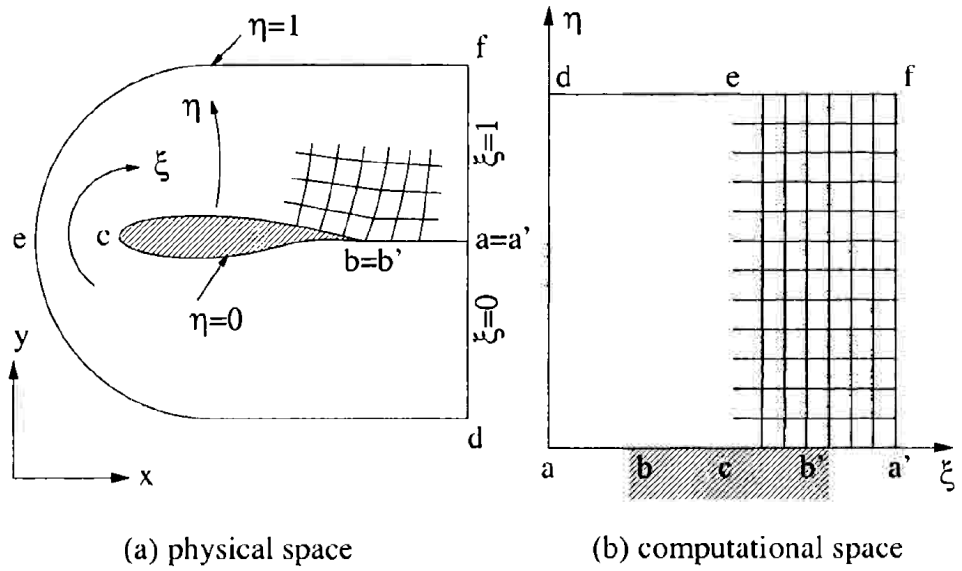

Figure 2.1: Curvilinear mapping of physical space onto computational space. Reproduced from [41].

2.4 Curvilinear Coordinate Transformation

Although the Cartesian form of the N-S equations is applicable to any computational grid topology, it is sometimes necessary and convenient to rewrite them in a generalized, body-conforming coordinate system when using structured grids. Due to the definition of numerical spatial derivative stencils based on uniform grid spacing, they are not suitable for grids with non-uniform spacing and rapid stretching. A Curvilinear coordinate transformation maps the governing equations from a non-uniform spaced Cartesian domain (x, y, z) onto a computational domain (ξ, η, ζ) with equal

grid spacing, as shown in Fig. 2.1. This is achieved by applying the chain-rule of differentiation on the Cartesian set of equations:

$$\frac{\partial \tilde{Q}}{\partial t} + \frac{\partial \tilde{F}}{\partial \xi} + \frac{\partial \tilde{G}}{\partial \eta} + \frac{\partial \tilde{H}}{\partial \zeta} = \tilde{S} \tag{2.27}$$

where,

$$\begin{aligned}
\tilde{Q} &= \tfrac{1}{J} Q \\
\tilde{E} &= \tfrac{1}{J} \left[\xi_t Q + \xi_x \left(F_i + F_v \right) + \xi_y \left(G_i + G_v \right) + \xi_z \left(H_i + H_v \right) \right] \\
\tilde{F} &= \tfrac{1}{J} \left[\eta_t Q + \eta_x \left(F_i + F_v \right) + \eta_y \left(G_i + G_v \right) + \eta_z \left(H_i + H_v \right) \right] \\
\tilde{G} &= \tfrac{1}{J} \left[\zeta_t Q + \zeta_x \left(F_i + F_v \right) + \zeta_y \left(G_i + G_v \right) + \zeta_z \left(H_i + H_v \right) \right] \\
\tilde{S} &= \tfrac{1}{J} S
\end{aligned} \tag{2.28}$$

J is the Jacobian of the coordinate transformation, defined by the determinant of the 3×3 matrix $\dfrac{\partial(\xi, \eta, \zeta)}{\partial(x, y, z)}$.

2.5 Numerical Algorithms Within the Solver Framework

This section describes the various numerical algorithms for spatial and temporal discretization of the governing equations, numerical boundary conditions, and convergence acceleration techniques available in the in-house computational solvers. The Curvilinear form of the RANS equations is solved using a cell-averaged finite-volume technique. The control volume is a computational cell defined around each grid point on a structured mesh. This cell is created by joining the mid-points of the edges of the mesh, as shown in Fig. 2.2. Inviscid and viscous fluxes are evaluated at the

interfaces of this computational cell, and integrated over all faces of a cell to obtain the time rate of change of the conserved quantities at each time step. The resulting semi-discrete form of Eq. 2.27 is given below:

$$\frac{\partial \tilde{Q}}{\partial t} = -\frac{\tilde{F}_{j+\frac{1}{2}} - \tilde{F}_{j-\frac{1}{2}}}{\Delta\xi} - \frac{\tilde{G}_{k+\frac{1}{2}} - \tilde{G}_{k-\frac{1}{2}}}{\Delta\eta} - \frac{\tilde{F}_{l+\frac{1}{2}} - \tilde{H}_{l-\frac{1}{2}}}{\Delta\zeta} + \tilde{S}_{j,k,l} \tag{2.29}$$

where, (j, k, l) are the indices corresponding to the grid points in (ξ, η, ζ) directions respectively and $(j \pm \frac{1}{2}, l \pm \frac{1}{2}, l \pm \frac{1}{2})$ define the interfaces of the computational cell. Spatial discretization techniques used to evaluate the inviscid and viscous flux contributions at each cell face are described in the following two sections.

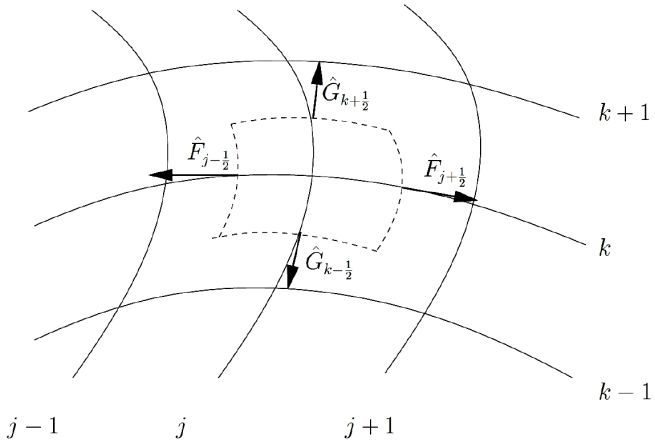

Figure 2.2: Schematic of a computational cell on a structured mesh. Reproduced from [41].

2.5.1 Inviscid Fluxes

Evaluation of inviscid fluxes (Eq. 2.4–2.6) involves two steps: (1) reconstruction of the primitive variables at cell faces, and (2) evaluation of the fluxes at cell faces using re-

constructed primitive variables. Reconstruction schemes for systems with hyperbolic properties are often based on some form of upwinding, through inclusion of explicit or implicit dissipation terms. This ensures that the numerical scheme respects the direction of wave propagation and uses information only from the upstream direction. In this work, the third-order Monotone Upstream-Centered Scheme for Conservation Laws (MUSCL) [51] and fifth-order Compact Reconstruction Weighted Essentially Non-Oscillatory (CRWENO) scheme [52] is used for the reconstruction of left and right states. With MUSCL scheme, the reconstructed primitive variables $(q^L_{i+\frac{1}{2}}, q^R_{i-\frac{1}{2}})$ at each cell face is expressed as a function of the cell-averaged values $(\overline{q}_{i-1}, \overline{q}_i, \overline{q}_{i+1})$ with a three-point stencil:

$$q^L_{i+\frac{1}{2}} = \overline{q} + \phi_i \left[\frac{1}{3} \left(\overline{q}_{i+1} - \overline{q_i} \right) + \frac{1}{6} \left(\overline{q}_i - \overline{q_{i-1}} \right) \right] \tag{2.30}$$

$$q^R_{i-\frac{1}{2}} = \overline{q} + \phi_i \left[\frac{1}{3} \left(\overline{q}_{i+1} - \overline{q_i} \right) + \frac{1}{6} \left(\overline{q}_i - \overline{q_{i-1}} \right) \right] \tag{2.31}$$

where,ϕ_i is Koren's differentiable limiter [53] given by:

$$\phi_i = \frac{3 \Delta \overline{q_i} \nabla \overline{q_i} + \epsilon}{2 \left(\Delta \overline{q_i} - \nabla \overline{q_i} \right)^2 + 3 \Delta \overline{q_i} \nabla \overline{q_i} + \epsilon} \tag{2.32}$$

ϵ is a small number used to prevent division by zero, and Δ and ∇ are forward and backward difference operators defined by $\Delta \overline{q}_i = (\overline{q}_{i+1} - \overline{q}_i)$ and $\nabla \overline{q}_i = (\overline{q}_i - \overline{q}_{i-1})$.

The reconstructed left and right states are used to compute inviscid fluxes at each cell face using Roe's flux difference splitting scheme with an entropy fix [54], as shown below:

$$F\left(q^L, q^R\right) = \frac{F\left(q^L\right) + F\left(q^R\right)}{2} - \left| \tilde{A}\left(q^L, q^R\right) \right| \frac{q^R - q^L}{2} \tag{2.33}$$

where, F_L and F_R are the left and right state fluxes, and $\tilde{A}$ is the Roe-averaged

Jacobian matrix. The second term on the right-hand side of the above equation represents numerical dissipation. Harten's entropy correction to Eigenvalues of the flux Jacobian is given by [55]:

$$|\lambda| = \begin{cases} |\lambda|, & if \ \ |\lambda| > \delta \\ \\ \frac{\lambda^2+\delta^2}{2\delta}, & if \ \ |\lambda| \leq \delta \end{cases} \tag{2.34}$$

where, $\delta = \max[0, (\overline{\lambda}_{i+1/2} - \overline{\lambda}_i), (\overline{\lambda}_{i+1} - \overline{\lambda}_{i+1/2})$. The over-bar on λ indicates Roe-averaged Eigenvalues.

CRWENO scheme computes the flux at a given cell interface from the fluxes at cell centers using a fifth order compact interpolation. A biased 3-point stencil $(j-1, j, j+1)$ is used to compute the interface flux at $(j + 1/2 :)$

$$\frac{3}{10}\hat{f}_{j-1/2} + \frac{3}{10}\hat{f}_{j-1/2} + \frac{3}{10}\hat{f}_{j-1/2} = \frac{1}{30}f_{j-1} + \frac{1}{30}f_{j-1} + \frac{1}{30}f_{j-1} \tag{2.35}$$

where the quantities with hat denote the approximate flux functions at cell interface and quantities without hat are the fluxes directly obtained from conservative variables at cell center.

2.5.2 Viscous flux

Viscous fluxes (Eq. 2.7–2.9) in the Curvilinear form of governing equations contain derivative terms of the form:

$$\frac{\partial}{\partial \xi}\left(\alpha \frac{\partial \beta}{\partial \eta}\right) \tag{2.36}$$

They are evaluated using a second order central differencing scheme as shown

below:

$$\frac{1}{\Delta\xi}\left(\left[\alpha_{j+\frac{1}{2},k}\frac{\beta_{j+\frac{1}{2},k+1}-\beta_{j+\frac{1}{2},k}}{\Delta\eta}\right]-\left[\alpha_{j-\frac{1}{2},k}\frac{\beta_{j-\frac{1}{2},k}-\beta_{j-\frac{1}{2},k-1}}{\Delta\eta}\right]\right) \tag{2.37}$$

where, $\delta_{j+\frac{1}{2},k}=\frac{\delta_{j,k}+\delta_{j+1,k}}{2}$ and $\delta=(\alpha,\beta)$.

2.5.3 Time Integration

After the inviscid and viscous fluxes on the right hand side of Eq. 2.29 are evaluated, the semi-discrete equation is integrated using a second-order accurate backwards in time method (also knowns as BDF2). Backwards-in-time methods are known as implicit time marching methods. They are more suited for boundary layer flows due to their superior stability and convergence characteristics compared to explicit time marching methods. In implicit methods, fluxes and source terms on the right-hand side of the semi-discrete equation are evaluated at the new time level, $n+1$. The resulting non-linear equation obtained using the BDF2 method is shown below:

$$\frac{\partial\tilde{Q}^{n+1}}{\partial t}=-\frac{\tilde{F}^{n+1}_{j+\frac{1}{2}}-\tilde{F}^{n+1}_{j-\frac{1}{2}}}{\Delta\xi}-\frac{\tilde{G}^{n+1}_{k+\frac{1}{2}}-\tilde{G}^{n+1}_{k-\frac{1}{2}}}{\Delta\eta}-\frac{\tilde{F}^{n+1}_{l+\frac{1}{2}}-\tilde{H}^{n+1}_{l-\frac{1}{2}}}{\Delta\zeta}+\tilde{S}^{n+1}_{j,k,l} \tag{2.38}$$

where,

$$\frac{\partial\tilde{Q}^{n+1}}{\partial t}=\frac{3\tilde{Q}^{n+1}-4\tilde{Q}^{n}+\tilde{Q}^{n-1}}{2\Delta t} \tag{2.39}$$

The above non-linear equation is linearized in time using a Taylor series expansion about $\tilde{Q}_n$ as follows:

$$\tilde{F}^{n+1}=\tilde{F}^{n}+\tilde{A}\Delta\tilde{Q}+O\left(\Delta t^2\right) \tag{2.40}$$

$$\tilde{G}^{n+1}=\tilde{G}^{n}+\tilde{B}\Delta\tilde{Q}+O\left(\Delta t^2\right) \tag{2.41}$$

$$\tilde{H}^{n+1}=\tilde{H}^{n}+\tilde{C}\Delta\tilde{Q}+O\left(\Delta t^2\right) \tag{2.42}$$

where, $\Delta\tilde{Q} = \tilde{Q}^{n+1} - \tilde{Q}^{n}$ is the solution update, and $A,\ B,\ C$ are the flux Jacobians given by $\dfrac{\partial \tilde{F}}{\partial \tilde{Q}}$, $\dfrac{\partial \tilde{G}}{\partial \tilde{Q}}$, and $\dfrac{\partial \tilde{H}}{\partial \tilde{Q}}$ respectively. The source term S is also linearized in a similar manner. Since the linearization operator is second-order accurate, it will not degrade the time-accuracy of the BDF2 scheme. The linearized form of Eq. 2.38 in terms of the solution update, $\Delta\tilde{Q}$, is given by:

$$\left[I + \Delta t\left(\delta_\xi \tilde{A}^n + \delta_\eta \tilde{B}^n + \delta_\zeta \tilde{C}^n\right)\right]\Delta\tilde{Q} = -\Delta t\left(\delta_\xi \tilde{F}^n + \delta_\eta \tilde{G}^n + \delta_\zeta \tilde{H}^n\right) \tag{2.43}$$

The right-hand side of the above equation represents the physics of the flow field, and the left-hand side represents the numerics responsible for stability and convergence of the solution. The above system of equations produces a banded matrix of algebraic equations that is solved using an approximate factorization method. Either Lower-Upper Symmetric Gauss-Seidel (LUSGS) method [56] or Diagonalized Alternating Direction Implicit (DADI) method is used to invert the linearized system of equation.

LUSGS

In the LUSGS algorithm, the left-hand side of the equation is factorized by grouping terms into a lower diagonal (L), an upper diagonal (U), and a main diagonal (D) as follows:

$$\left[L + D + U\right]\Delta\tilde{Q}^n\left[D + L\right]D^{-1}\left[D + U\right]\Delta\tilde{Q}^n = -\Delta t\left[RHS\right]^n \tag{2.44}$$

where,

$$L = \Delta t\left(*4 - \tilde{A}^{+}_{j-1,k,l} - \tilde{B}^{+}_{j,k-1,l} - \tilde{C}^{+}_{j,k,l-1}\right) \tag{2.45}$$

$$U = \Delta t\left(-\tilde{A}^{-}_{j+1,k,l} - \tilde{B}^{-}_{j,k+1,l} - \tilde{C}^{-}_{j,k,l+1}\right) \tag{2.46}$$

$$D = I + \Delta t \left(\tilde{A}^{+}_{j,k,l} - \tilde{A}^{-}_{j,k,l} + \tilde{B}^{+}_{j,k,l} - \tilde{B}^{-}_{j,k,l} + \tilde{C}^{+}_{j,k,l} - \tilde{C}^{-}_{j,k,l} \right) \tag{2.47}$$

This system is solved to obtain the solution update ($\Delta\tilde{Q}$) using a two-step procedure as shown below:

$$[D + L]\,\Delta\overline{\overline{Q}} = -\Delta t\,[RHS]^n \tag{2.48}$$

$$[D + U]\,\Delta\tilde{Q} = D\Delta t\overline{\overline{Q}} \tag{2.49}$$

Since L, D, and U are block matrices of size 5×5 for the three dimensional N-S equations and 4×4 for the two dimensional N-S equations, inverting the above two equations is computationally expensive. The main diagonal (D) is reduced to a scalar value using the spectral radius approximation for the flux Jacobian matrices ($\tilde{A}, \tilde{B}, \tilde{C}$) as follows:

$$\tilde{A}^{+} = \frac{1}{2}\left(\tilde{A} + \sigma_\xi\right), \qquad \tilde{A}^{-} = \frac{1}{2}\left(\tilde{A} - \sigma_\xi\right) \tag{2.50}$$

$$\sigma_\xi = |U_\xi| + c + \frac{2\mu\left(\xi_x^2 + \xi_y^2 + \xi_z^2\right)}{\rho} \tag{2.51}$$

where, U_ξ is the contravariant velocity in the ξ-direction (and similarly for $\tilde{B}$ and $\tilde{C}$).

DADI

Another method of inverting the LHS is by using DADI [61]. The equation is rewritten by Beam and Warming [63] and is first order implicit in time:

$$[I + \Delta t(\partial_\xi \tilde{A} + \partial_\eta \tilde{B} + \partial_\zeta \tilde{C})\tilde{Q}\left[I + \Delta t\partial_\xi \tilde{A}\right]\left[I + \Delta t\partial_\eta \tilde{B}\right]\left[I + \Delta t\partial_\zeta \tilde{C}\right] \tag{2.52}$$

The original inversion has now been replaced by three less expensive inversions. The computational expense can be further reduced by diagonalizing the inviscid compo-

nent of the flux Jacobians:

$$\lambda_\xi = T_\xi^{-1} \hat{A}_i T_\xi \tag{2.53}$$

$$\lambda_\eta = T_\eta^{-1} \hat{B}_i T_\eta \tag{2.54}$$

$$\lambda_\zeta = T_\zeta^{-1} \hat{C}_i T_\zeta \tag{2.55}$$

where T_ξ is the set of left eigenvectors of matrix $\hat{A}_i$ and T_ξ^{-1} is the set of right eigenvectors of matrix $\hat{A}_i$. Similarly, T_η and T_ζ are matrices corresponding to the matrices $\hat{B}_i$ and $\hat{C}_i$ respectively. The set of eigenvalues of matrix $\hat{A}_i$ are given in matrix λ_ξ. Similarly λ_η and λ_ζ contain eigenvalues of $\hat{B}_i$ and $\hat{C}_i$.

Substituting this diagonalized form of the flux Jacobians and ignoring the viscous contribution on the LHS into the discretized Navier–Stokes equation, one can write eq. 2.52 as:

$$\left[T_\xi T^{-1} + h(T_\xi \lambda_\xi T_\xi^{-1})\right] \left[T_\eta T^{-1} + h(T_\eta \lambda_\eta T_\eta^{-1})\right] \left[T_\zeta T^{-1} + h(T_\zeta \lambda_\zeta T_\zeta^{-1})\right] \Delta\hat{Q}^n = \Delta t \left[RHS^n\right] \tag{2.56}$$

Assuming that the eigenvectors of the inviscid flux Jacobians are locally constant in the local neighborhood of (j, k, l), the above equation can be rewritten as:

$$T_\xi \left[I + \Delta t \delta_\xi \lambda_\xi\right] T_\xi^{-1} T_\eta \left[I + \Delta t \delta_\eta \lambda_\eta\right] T_\eta^{-1} T_\zeta \left[I + \Delta t \delta_\zeta \lambda_\zeta\right] T_\zeta^{-1} = \Delta t \left[RHS^n\right] \tag{2.57}$$

The diagonal algorithm reduces the block tridiagonal inversion to 5×5 matrix multiplications and scalar tridiagonal inversions. The diagonal algorithm described above is

rigorously valid for the Euler equations. This is because we have neglected the implicit linearization of the viscous fluxes. The viscous flux Jacobians are not simultaneously diagonalizable with the inviscid flux Jacobians and therefore an approximation to the viscous Jacobian eigenvalues have to be used and is given by:

$$\lambda_v(\xi) = \overline{\mu J^{-1}\left(\xi_x^2 + \xi_y^2 + \xi_z^2\right)} J\rho^{-1} \tag{2.58}$$

$$\lambda_v(\eta) = \overline{\mu J^{-1}\left(\eta_x^2 + \eta_y^2 + \eta_z^2\right)} J\rho^{-1} \tag{2.59}$$

$$\lambda_v(\zeta) = \overline{\mu J^{-1}\left(\zeta_x^2 + \zeta_y^2 + \zeta_z^2\right)} J\rho^{-1} \tag{2.60}$$

The new form of diagonal algorithm is given by

$$T_\xi\left[I + \Delta t\left(\delta_\xi\lambda_\xi - \delta_{\xi\xi}\lambda_v(\xi)\right)\right]T_\xi^{-1}T\left[I + \Delta t\left(\delta_\eta\lambda_\eta - \delta_{\eta\eta}\lambda_v(\eta)\right)\right]T_\eta^{-1}$$
$$T_\zeta\left[I + \Delta t\left(\delta_\zeta\lambda_\zeta - \delta_{\zeta\zeta}\lambda_v(\zeta)\right)\right]T_\zeta^{-1}\Delta\hat{Q}_n = \Delta t \tag{2.61}$$

Dual time stepping

Approximation of the LHS results in factorization errors. To remove these factorization errors and to recover time accuracy, one must perform sub-iterations at each physical time step. To carry out these iterations, eq. 2.29 can be modified to consider a term that also contains a fictitious pseudo time, τ:

$$\frac{\partial\tilde{Q}}{\partial\tau} + \frac{\partial\tilde{Q}}{\partial t} + \frac{\partial\tilde{F}}{\partial\xi} + \frac{\partial\tilde{G}}{\partial\eta} + \frac{\partial\tilde{H}}{\partial\zeta} = \tilde{S} \tag{2.62}$$

Convergence of the pseudo-time (sub-iterations) at each physical time step is important for obtaining an accurate transient solution. Discretization of eq. 2.29 with first order finite difference scheme for both artificial and physical time results in

$$\frac{\partial \tilde{Q}^{k+1} - \tilde{Q}^{k}}{\partial \tau} + \frac{\partial \tilde{Q}^{k+1} - \tilde{Q}^{n}}{\partial t} + \frac{\partial \tilde{F}^{k+1}}{\partial \xi} + \frac{\partial \tilde{G}^{k+1}}{\partial \eta} + \frac{\partial \tilde{H}^{k+1}}{\partial \zeta} = \tilde{S}^{k+1} \tag{2.63}$$

where k is the pseudo-iteration counter and n is is the time step counter. After linearization one gets:

$$\left[\frac{1}{\Delta\tau} + \frac{1}{\Delta t} + \delta_\xi \tilde{A}^k + \delta_\eta \tilde{B}^k + \delta_\zeta \tilde{C}^k\right] \Delta Q^k = -\left[\delta_\xi \tilde{F}^k + \delta_\eta \tilde{G}^k + \delta_\zeta \tilde{H}^k - \tilde{S}^k + \frac{Q^k - Q^n}{\Delta t}\right] \tag{2.64}$$

Defining $h = \dfrac{\Delta t}{1 + \dfrac{\Delta t}{\Delta \tau}}$ and rearranging:

$$\left[I + h(\delta_\xi \tilde{A}^k + \delta_\eta \tilde{B}^k + \delta_\zeta \tilde{C}^k)\right] \Delta Q^k = -h\left[\delta_\xi \tilde{F}^k + \delta_\eta \tilde{G}^k + \delta_\zeta \tilde{H}^k - \tilde{S}^k + \frac{Q^k - Q^n}{\Delta t}\right] \tag{2.65}$$

The above equation has similar form as eq. 2.43 and therefore can be solved either using LUSGS or DADI scheme. The unsteady residual at each time step is given by:

$$\delta_\xi \tilde{F}^k + \delta_\eta \tilde{G}^k + \delta_\zeta \tilde{H}^k - \tilde{S}^k + \frac{\tilde{Q}^k - \tilde{Q}^n}{\Delta t} \tag{2.66}$$

This term should approach zero as the solution converges during the sub- iterations. Typically, a drop in the unsteady residual on the order of one to two orders of magnitude may be considered to be sufficient to ensure that the iteration error is less than the other remaining discretization errors. If the pseudo time size is made very large τ, then $h \to \infty$ and we obtain a Newton sub-iteration scheme. If no sub-iterations are used, then the traditional Euler implicit method is recovered.

2.5.4 Initial Conditions

The unsteady Navier-Stokes equations represent an Initial Boundary Value Problem (IBVP), which means that the evolution of the solution in time is influenced by the initial conditions and boundary conditions specified in the computational domain. This section describes the manner in which the initial conditions are specified.

To perform the time integration of the Navier-Stokes equations, an initial flow field consisting of the primitive variables (ρ, u, v, w, p) must be specified at each grid point. In this work, two types of problems are solved: (1) steady-state, and (2) transient (or time-accurate). For steady state simulations, initial conditions do not affect the converged solution. However, a good choice of initial conditions can improve the convergence behavior of a steady-state simulation. In simulations of external aerodynamic flows, the entire flow field is typically initialized with the free-stream values. Since the non-dimensionalized N–S equations are used in this work, initial values of (u, v, w) are deduced from free-stream Mach number components along the Cartesian coordinate directions. For the current choice of reference quantities, it can be shown that free-stream density (ρ_∞) is unity and free-stream pressure (p_∞) is $\frac{1}{\gamma}$, where $\gamma = 1.4$ is the ratio of specific heats for air at standard temperature and pressure.

2.5.5 Boundary Conditions

This section presents the numerical treatment of the physical and artificial boundaries that are part of the current simulations. Examples of physical boundary conditions

are the specification of primitive variables on a solid wall boundary through a no-slip condition or an adiabatic/isothermal requirement. Artificial boundaries such as an inlet or outlet are created due to the truncation of the computational domain to a finite size. In this section, the discussion of boundary conditions is limited to those arising in external flow problems simulated on a structured O-mesh and C-mesh with both types of mesh extruded in the span-wise direction. The relevant boundary conditions specified on a C-mesh and O-mesh are shown in Fig. 2.3.

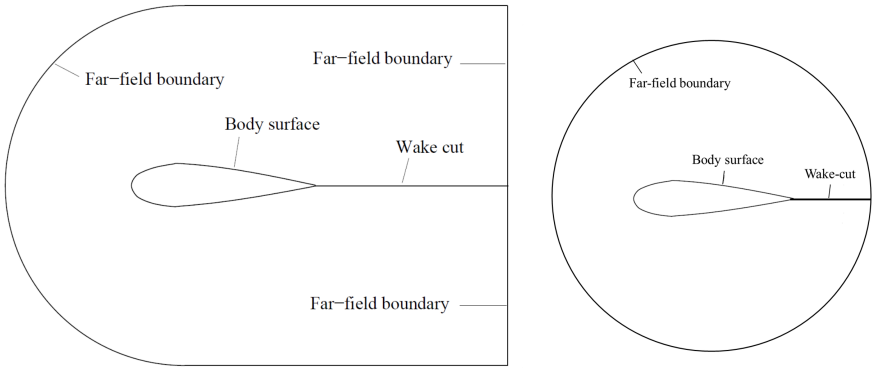

(a) C-topology (b) O-topology

Figure 2.3: Boundary conditions on a structured C-topology mesh and an O-topology mesh. Reproduced from [60].

Wall Boundary

At a viscous solid wall, the no-slip and no-penetration conditions are enforced. All velocity components are set to zero for grid points on a stationary wall boundary. For moving walls, the velocity components are set to based on the surface motion. Density is extrapolated from the interior of the domain. Pressure on wall boundary is obtained either by extrapolation or by solving the normal momentum equation [55].

Wake-cut Boundary

A key component of a C-topology mesh is its wake-cut adjacent to the solid wall boundary. It consists of two identical grid lines overlapping in the same physical space. Since the wake-cut is an artifact of the topology, continuity of flow must be ensured across this "boundary". This is achieved by an explicit averaging of the solution on grid points from either side of the wake-cut and setting the two overlapping grid lines to the averaged solution.

Far-field Boundary

In external flow simulations, the computational domain is truncated to a finite size, thus creating an artificial boundary. Specification of such a boundary condition must ensure that no spurious information propagates across the boundary: (1) waves that are going out of the domain must be allowed to pass through without any spurious reflections back into the domain, (2) only physical disturbances must be propagated into the domain from the exterior. In this work, non-reflecting boundary conditions based on one-dimensional Riemann invariants are used at far-field boundaries [55]. These boundary conditions are strictly designed to allow small disturbances to pass through the far-field boundary in the absence of strong mean flow gradients approaching the boundary. Therefore, meshes for external flow problems are typically generated with the far-field boundary located at large distances from regions of flow activity, such as flow past a solid body. Mesh stretching is also employed towards the far-field boundary to numerically dissipate strong flow gradients.

Periodic Boundary

Periodic boundary conditions are used when the physical geometry and the expected pattern of the flow solution have a periodically repeating nature. In the airfoil simulations conducted in the present work, there exists periodicity of geometry and the flow behavior in the span-wise direction. As a result, periodic boundary conditions are applied in the span-wise direction. This saves computational resources as the length of the computational domain in the span-wise direction can be limited to half a chord. By applying periodic boundary conditions at the faces of the computational domain normal to the span-wise direction, a wing of an infinite span is simulated effectively.

2.6 Parallelization

An accurate resolution of the boundary layer and incipient separation using DDES type methods requires a well-resolved mesh in the region around the airfoil. All the meshes used in this work have the smallest wall-normal spacing of $y^+ \leq 0.5$ and the stretching ratio is close to unity in the near-surface region of the airfoil. This stretching ratio ensures that the cells are as close to isotropic in the boundary layer region. The mesh spacing in the span-wise direction is kept small to the order of 0.006 chords which is recommended for the DDES type methods [25]. Because of memory constraints, a single GPU/CPU processor cannot accommodate the computational domain entirely. A typical GPU card with a video RAM size of 6 Gigabytes is able to support only up to 3.5 million mesh points whereas a well-resolved airfoil domain used

in the current work comprises of nearly 7 million mesh points. Additionally, DDES type simulations can be considerably expensive due to the extended computation time. A large number of iterations are needed with small time-steps to achieve statistical convergence in simulations of flow that undergo incipient separation.

Because of the need to speed-up turbulent simulation, and also overcome memory limitations of available GPU cards and CPU processors, it becomes imperative to divide the computational domain into smaller sub-domains. Both the solvers are capable of dividing the computational domain among multiple processors using the domain decomposition approach and running the simulations simultaneously on all processors. The OverTURNS code is written using the FORTRAN 77/90 programming language in a modular fashion. The code is parallelized using the Message Passing Interface (MPI) library. An equally capable MPI library is available for The GPU based solver which is developed using CUDA-C programming language.

With domain decomposition, the computational domain is divided into similarly sized blocks and solved as subproblems. Each processor is assigned the job of solving the governing equations on a unique mesh block. At the end of each time step, the exchange of relevant data between blocks sharing a common interface is handled by the MPI implementation. Figure 2.4 shows an O-mesh with a span-wise extent of half chord being split into multiple blocks along the airfoil span. Generally, the domain decomposition is preferred in the span-wise direction since splitting in the wall-normal direction may affect solution convergence and accuracy, due to the presence of strong gradients in the boundary layer.

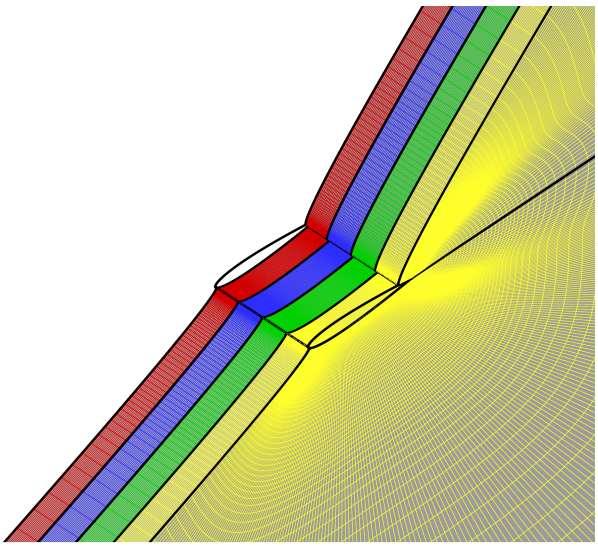

Figure 2.4: Spanwise domain decomposition of an O-topology airfoil mesh.

2.7 Summary

Details of the governing equations and their numerical solution methodology in the in-house CFD solvers were summarized in this chapter. Techniques specific to high-fidelity airfoil simulations were presented. The discussion also included advanced algorithms such as reconstruction schemes and All-Mach correction that was used in this work. In the next section, the fundamentals of turbulence modeling are discussed along with the details pertaining to hybrid RANS-LES methods and importance of involved length scales.

Chapter 3

Turbulence Physics and Modeling

A wide variety of methods exist to represent turbulence each with specific pros and cons terms of computational cost and prediction accuracy. These methods can be classified in the increasing order of computational cost as shown in figure 3.1. The increasing computational cost also corresponds to decreasing empiricism starting from RANS model in which the complete range of turbulent motions are described by the mathematical model to DNS in which all the turbulent motions are directly resolved in space and time.

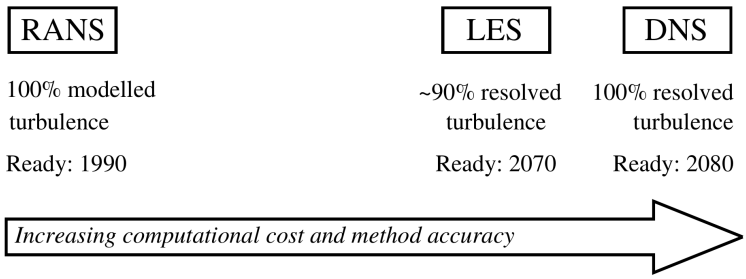

Figure 3.1: Key turbulence treatment methods arranged in the increasing order of computational cost. Reproduced from [26] .

3.1 Direct Numerical Simulation (DNS)

DNS is an approach resolving all the spatial and temporal scales present in a turbulent flow field. However, it is well established that DNS simulations are prohibitively expensive for flow problems at relatively high Reynolds numbers. It is because as the Reynolds number increases, the magnitude of the smallest turbulent length scale (Kolomogorov scale) relative to the largest scales decreases. Since the turbulence is three-dimensional in space and unsteady in time, the requirement of resolution of all scales increases the numerical cost of DNS strongly with the higher Reynolds number. Since the smallest spatial eddies must also be resolved temporally, the numerical time step size also gets smaller. Pope [27] estimated that for an isotropic turbulence in a cubic domain of length l_o, the number grid points needed to resolve all the spatial scales is proportional to $160Re_{l_o}^3$. The scaling gets worse for the non-isotropic flows. Given the correct grid-resolution and sufficient small time-step size, DNS contains no empiricism and provide most accurate results.

3.2 Reynolds-Averaged Navier–Stokes Equations (RANS)

The Reynolds-Averaged Navier–Stokes (RANS) equations along with addition turbulence models present an affordable alternative to DNS simulations. RANS equations describe the turbulence statistically with the help of mathematical models. These models assume a steady mean flow-field with no turbulent motion being resolved di-

rectly. As such steady-state solutions can be computed on highly anisotropic grids with relatively larger wall-normal spacing and substantially reduced computational cost. For this reason, RANS models are used widely in the industry for the CFD analysis. In the RANS approach, dependent variables in the baseline governing equations (2.1–2.9) are decomposed into their mean and fluctuating components. This decomposition is called Reynolds decomposition. if $\phi(x_i, t)$ is the unsteady turbulent field, then Reynolds decomposition results into:

$$\phi(x_i, t) = \overline{\phi}(x_i) + \phi'(x_i, t) \tag{3.1}$$

and the resulting Navier–Stokes equations are averaged over a period of time. In the averaging procedure, the mean or time-averaged quantity $\overline{\phi}(x_i)$ is defined as:

$$\overline{\phi}(x_i) = \frac{1}{\Delta t} \int_{t_o}^{t_o+\Delta t} \phi(x_i, t) dt \tag{3.2}$$

where Δt is of the order of the duration in which the flow achieves a steady state solution.

Now, many important flows exhibit unsteadiness without necessarily transitioning to turbulence. This unsteadiness can arise from hydrodynamic instabilities such as vortex shedding behind a blunt trailing edge of airfoil section or shock related oscillations. In such cases, performing time-averaging over large Δt is not applicable and will lead to a significant source of error in the transient flow solution prediction. Instead, time-averaging over a suitable finite time period is required, such that the non-turbulent unsteadiness is resolved in the mean flow and the turbulent fluctuations are described by the RANS model. Such a simulation is called unsteady RANS

(URANS). By definition, the time-average of a fluctuating quantity is zero:

$$\overline{f'} = \frac{1}{\Delta t}\int_{t_o}^{t_o+\Delta t} f' dt = 0 \tag{3.3}$$

The following relations hold for sum and product of any two fluctuating quantities:

$$\overline{\overline{f}g'} = 0 \qquad \overline{\overline{f}g} = \bar{f}\bar{g} \qquad \overline{f+g} = \bar{f} + \bar{g} \tag{3.4}$$

The most important identity is that the time-average of the product of two fluctuating quantities is not zero:

$$\overline{f'f'} \neq 0 \quad and \quad \overline{f'g'} \neq 0 \tag{3.5}$$

In the Reynolds decomposition approach, dependent variables in the Navier–Stokes equations are written as sum of their mean and fluctuating components as shown below:

$$u = \overline{u} + u' \qquad v = \overline{v} + u' \qquad w = \overline{w} + w' \qquad \rho = \overline{\rho} + \rho' \qquad p = \overline{p} + p' \qquad T = \overline{T} + T' \tag{3.6}$$

Substitution of the Reynolds-decomposed dependent variables in Eq. 3.6 into the instantaneous, unsteady Navier–Stokes equations in Eq. 2.1, followed by time-averaging of the equations gives rise to a new set of governing equations. These are known as the Reynolds-Averaged Navier–Stokes equations (RANS). The Reynolds-averaged continuity and momentum equations for incompressible flow are:

$$\frac{\partial \overline{u}_i}{\partial x_i} = 0 \tag{3.7}$$

$$\rho\frac{D\overline{u}_i}{Dt} = -\frac{\partial \overline{p}}{\partial x_i} + \frac{\partial \overline{\tau}_{ij}}{\partial x_j} - \frac{\partial \overline{u_i' u_j'}}{\partial x_i} \tag{3.8}$$

where the time-averaged viscous stress tensor is

$$\overline{\tau}_{ij} = \mu \left(\frac{\partial \overline{u}_i}{\partial x_i} + \frac{\partial \overline{u}_i}{\partial x_i} \right) = 2\mu \overline{S}_{ij} \tag{3.9}$$

These are identical in form to the unsteady incompressible Navier–Stokes equations, except that the time-averaged quantities $\overline{\phi}$ have replaced the instantaneous ϕ quantities, and there is now an additional tensor $\rho\overline{u_i' u_j'}$. The tensor behaves as an apparent stress tensor due to the transport of momentum by turbulent fluctuations. Hence it is commonly known as the Reynolds Stress Tensor (τ_{ij}):

$$(\overline{\tau_{ij}})_{turb} = -\rho\overline{u_i' u_j'} \tag{3.10}$$

Closure to the RANS equations requires representation of the Reynolds stress tensor (τ_{ij}) in terms of the mean flow quantities. The area of research concerned with finding closure to the RANS equations is known as Turbulence Modeling and the specific methods of closure are called Turbulence Models.

3.3 Boussinesq Eddy Viscosity Hypothesis

One approach to turbulence closure of the RANS equations is to solve six additional transport equations, one for each of the stress tensor components, along with an equation for the energy dissipation rate. These models are categorized as Reynolds Stress Models (RSM) [47, 48]. Although Reynolds stress models adopt the most physically realistic approach to turbulence modeling, they are expensive and suffer from issues of robustness and convergence. A more common method of approximating

the Reynolds stress tensor is based on the hypothesis that the effects of turbulence are analogous to an molecular viscosity. This hypothesis is called the Boussinesq eddy viscosity hypothesis and it relates the Reynolds stress tensor to the mean strain rate as follows:

$$(\overline{\tau_{ij}})_{turb} = -\rho\overline{u_i' u_j'} = \frac{2}{3}\overline{\rho}k\delta_{ij} - \mu_t\left[\left(\frac{\partial\overline{u_i}}{\partial x_j} + \frac{\partial\overline{u_i}}{\partial x_j}\right) - \frac{2}{3}\frac{\partial\overline{u_k}}{\partial x_k}\delta_{ij}\right] \tag{3.11}$$

where, k is the turbulent kinetic energy given by:

$$k = \frac{1}{2}\left[\overline{(u_1')^2} + \overline{(v_1')^2} + \overline{(w_1')^2}\right] \tag{3.12}$$

and μ_t is a scalar value known as the turbulent or eddy viscosity. With this assumption, the final form of the total viscous stress tensor in the RANS equations becomes:

$$(\tau_{ij})_{total} = \frac{2}{3}\overline{\rho}k\delta_{ij} - (\mu + \mu_t)\left[\left(\frac{\partial\overline{u_i}}{\partial x_j} + \frac{\partial\overline{u_i}}{\partial x_j}\right) - \frac{2}{3}\frac{\partial\overline{u_k}}{\partial x_k}\delta_{ij}\right] \tag{3.13}$$

The turbulent kinetic energy term on the right-hand side is typically absorbed into the pressure term of the inviscid fluxes (Eq. 2.4–2.6). This approach assumes isotropic turbulence, which causes it to perform poorly for flows with significant turbulence anisotropy, such as decelerating boundary layers. Turbulence modeling research in the past few decades has produced hundreds of models to evaluate turbulent kinetic energy and eddy viscosity in the flow field as a function of mean flow quantities. This class of models that compute eddy viscosity to close the RANS equations are referred to as linear eddy viscosity models (LEVM). These models range from zero-equation algebraic expressions such as the Baldwin-Lomax model [49] to the four-equation $\nu^2 - f$ model [50]. Most of the turbulence models are calibrated to match theoretical

solutions and experimental data for canonical flows such as boundary layers and free shear layers. Therefore, a significant level of empiricism is present in turbulence modeling.

3.4 Large Eddy Simulation (LES)

The basic theory and idea of LES were formulated by Smagorinsky [28]. LES lies in between RANS and DNS in the manner that the large turbulent scales are resolved directly and the smaller scales are approximated by a mathematical model. According to the theory of Kolmogorov, the larger scales contain the majority of the energy and are most important in determining the flow behavior. Resolving them directly leads to high accuracy in LES. The smaller scales only contribute a fraction of the total energy and are assumed to behave uniformly and are easily modeled.

The energy distribution of these scales is shown in Figure 3.2. The Kolmogorov's law is indicated by the straight line in the figure and is defined by:

$$E(k) = C_k \epsilon^{2/3} k^{-5/3} \tag{3.14}$$

where C_k is a constant around 1.5, ϵ is the energy dissipation rate and k the wavenumber (proportional to the inverse of the length scale). The energy spectrum is roughly divided into three regions:

1. The first region is characterized by the larger eddies which contain the most energy and are denoted by the wavenumber k_i .

2. The second region contains the eddies which follow the Kolmogorov's law and

this region is known as the inertial subrange. The region is dominated by the transitive scales and transfers energy from the large to the small scales.

3. The last region is the dissipative range and contains the very small scales. The behavior of the eddies is dominated by the viscosity and energy transfer from the larger scales. It can be assumed that they do not depend on the larger scales and therefore are not aware of geometric boundaries.

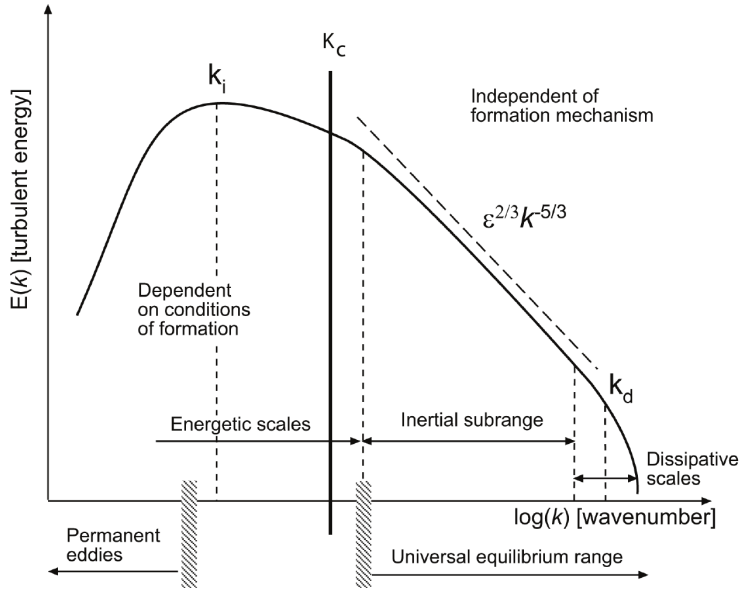

Figure 3.2: The energy spectrum divided into three regions: A energy-containing part, a region which transfers the energy to the smaller scales and the dissipation region. Reproduced from [29].

3.4.1 LES filter

In Figure 3.2, the cutoff wavenumber K_c denotes the scale separation between the larger and smaller scales and filtering is used to separate large scales from the small

scales. The filter is based on a locally derived weighted average of the flow properties over a volume of a fluid element. An important feature of the filter process is the filter width Δ. The turbulent length scales larger than Δ are retained in the flow field, whereas the smaller scales, the Sub-Grid Scales (SGS) are left to be modeled. Similar to RANS, the notion here is to express flow variables as a contribution of the large and small scales:

$$u = \overline{u} + u' \tag{3.15}$$

The over-bar refers to the larger, resolved scales, whereas the prime corresponds to the smaller scales. The filtering process to obtain the larger scales is defined as:

$$\bar{u} = \oint u(x')G(x, x'; \Delta)dx' \tag{3.16}$$

where the filter function $G(x, x', \Delta)$ satisfies following condition:

$$\oint G(x, x'; \Delta)dx' = 1 \tag{3.17}$$

Figure 3.3 illustrates one-dimensional representation of the filtering operation of a flow variable. A standard implicit top-hat filter is used in the current work. This filter is simply defined as the average over a rectangular region and is applied effectively to finite volume methods. If the grid-spacing is chosen to be the filter width Δ, the averaged and the local value of $\bar{u}$ will be equal. The top-hat filter function is given as:

$$G(x, \Delta) = \begin{cases} \frac{1}{\Delta}, & if|x'| \leq \frac{\Delta}{2} \\ 0, & otherwise \end{cases} \tag{3.18}$$

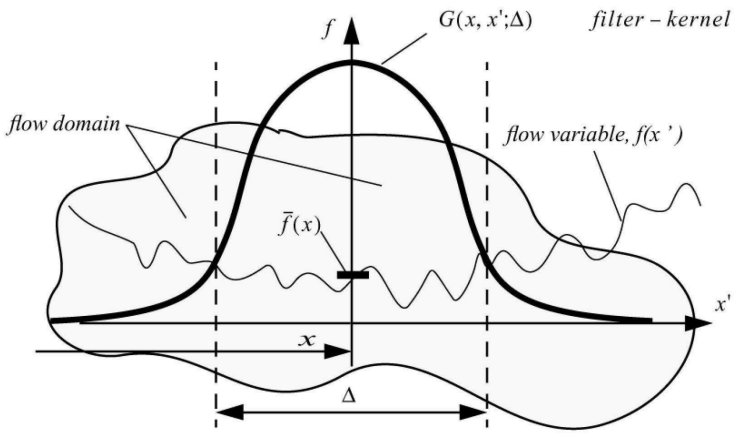

Figure 3.3: A representation of an arbitrary filter function of a flow variable. Reproduced from [30].

3.4.2 Filtered Navier-Stokes equation

When the filter is applied to the incompressible Navier–Stokes equations, one obtains the equations of motion, in terms of the resolved large scales, denoted by the over-bar:

$$\frac{\partial \bar{u}_i}{\partial x_i} = 0 \tag{3.19}$$

$$\frac{\partial \bar{u}_i}{\partial t} + \frac{\partial}{\partial x_i}(\bar{u}_i \bar{u}_j) = -\frac{1}{\rho}\frac{\partial \bar{p}}{\partial x_i} + \frac{1}{\rho}\frac{\partial \tau_{ij}^R}{\partial x_j} + \nu \nabla^2 \bar{u}_i \tag{3.20}$$

The non-linear convection term in Navier–Stokes equations causes a dependency between the resolved and unresolved scales. The influence of the unresolved scales are incorporated in the sub-grid stress tensor, which includes the residual stresses. This is defined as:

$$\tau_{ij}^R = \rho\left(\overline{u_i u_j} - \bar{u}_i \bar{u}_j\right) \tag{3.21}$$

A numerical model with an appropriate quality and quantity of numerical dissipation is needed to provide correct dissipative action of the unresolved scales. In this work, Smagorisnky [28] model is used to define the unresolved scales in LES and is described in the next section

3.4.3 The Smagorinsky model

This is the most widely used sub-grid scale model to define the unresolved scales in LES and was proposed by Smagorinsky [31]. Similar to RANS, this model is also an eddy viscosity model employing the Boussinesq hypothesis (section 3.3) to relate the sub-grid scale stresses to the local flow strain. Therefore, the stress tensor can be written as:

$$\tau_{ij}^{R} = 2\rho\nu_t\bar{S_{ij}} + \frac{1}{3}\delta_{ij}\tau_{kk}^{R} \tag{3.22}$$

where ν_{sgs} is the sub-grid scale eddy viscosity. Smagorinsky derived an algebraic expression for ν_{sgs}:

$$\nu_{sgs} = \left(C_S\Delta\right)^2 S^* \tag{3.23}$$

where

$$S^* = \sqrt{2S_{ij}S_{ij}} \tag{3.24}$$

There are some deficiencies pertaining to the Smagorinsky model. The Smagorinsky parameter C_s is not a constant and varies for homogeneous and sheared flows. Therefore, a fixed value is not suited for separating flows with mixed turbulence phenomena. The effect of wall proximity in the viscous sublayer is also not correctly reproduced by the model. The method requires additional damping which is provided through

modification of grid length scale Δ in this work. After substitution, the filtered incompressible Navier–Stokes equations become similar incompressible Reynolds-Averaged Navier–Stokes equations:

$$\frac{\partial \bar{u_i}}{\partial t} + \frac{\partial}{\partial x_j}(\bar{u_i}\bar{u_j}) = -\frac{1}{\rho}\frac{\partial \bar{p}}{\partial x_i} + 2\frac{\partial}{\partial x_j}[(\nu + \nu_{sgs})\bar{S_{ij}}] \tag{3.25}$$

The similarity of the equations 3.20 and 3.25 forms the basis of DES type Hybrid RANS-LES methods.

3.5 Turbulence closure model

One of the most widely used turbulence models in aerospace applications is the one-equation Spalart–Allmaras (SA) model [46]. It is based on solving additional transport equation to compute eddy viscosity ν_t and is known for its accuracy and numerical robustness for many internal and external flow problems. The turbulent eddy viscosity is defined as:

$$\upsilon_t = \tilde{\nu} f_{v1} \qquad with \quad f_{v1} = \frac{X^3}{X^3 + c_{v1}^3} \quad and \;\; X = \frac{\tilde{\nu}}{\nu} \tag{3.26}$$

Here, c_{v1} is a constant and ν represents the molecular viscosity. $\tilde{\nu}$ is the working variable, which satisfies the transport equation given by:

$$\frac{D\tilde{\nu}}{Dt} = c_{b1}\tilde{S}\tilde{\nu} + \frac{1}{c_\sigma}\left[\nabla.((\nu + \tilde{\nu})\nabla\tilde{\nu}) + c_{b2}(\nabla\tilde{\nu})^2\right] - c_{w1}f_w[\frac{\tilde{\upsilon}}{\tilde{d}}]^2 \tag{3.27}$$

$$S = \omega + \frac{\tilde{\nu}}{k^2\tilde{d}}f_{v2} \tag{3.28}$$

$$f_{\nu 2} = 1 - \frac{X}{1 + x f_{\nu 1}} \tag{3.29}$$

$$f_w = g\left[\frac{1+c_{w3}^6}{g^6+c_{w3}^6}\right]^{1/6} \tag{3.30}$$

$$g = r + c_{w2}(r^6 - r) \tag{3.31}$$

$$r = \frac{\tilde{\nu}}{\tilde{S}k^2\tilde{d}^2} \tag{3.32}$$

Constant values are set of constants are listed in table 3.1.

$c_{b1} = 0.135$	$c_\sigma = 2/3$
$c_{b2} = 0.622$	$\kappa = 0.41$
$c_{w2} = 0.3$	$c_{w3} = 2$
$c_{\nu 1} = 7.1$	$c_{w1} = c_{b1}/\kappa^2 + (1 + c_{b2})/c_\sigma$

Table 3.1: List of constants corresponding to Spalart–Allmaras model.

3.6 Hybrid RANS-LES methods

Hybrid RANS-LES methods typically use LES in the vicinity of the wall where turbulent boundary layer needs to be resolved. Away from the wall RANS modeling is used. The zonal class of hybrid RANS-LES technique usually provides an automated and smooth transition from RANS to LES. The current work focuses on DES (Detached Eddy Simulation) type hybrid RANS-LES methods which were first proposed by Spalart [20]. The general idea behind these types of models is to combine the advantages of both RANS and LES. More precisely, the model acts as a RANS model in attached boundary layers and turns into LES for the separated flow regions. The

switching between two models depends on the local grid-resolution. An overview of DES and DDES (Delayed Detached Eddy Simulation) and the issues encountered with these models are addressed in the next section.

3.6.1 Detached Eddy Simulation (DES)

The standard DES implementation [20] combines the standard Spalart–Allmaras RANS model with the Sub-Grid Scale (SGS) LES by modifying the length scale in the destruction term of the SA turbulence model. The modified length scale $\tilde{d}$ is defined as the minimum of the wall normal distance d and the length parameter proportional to the local grid spacing:

$$\tilde{d} \equiv \min(d, C_{DES}\Delta) \tag{3.33}$$

Here C_{DES} is a constant calibrated through experiment of homogeneous turbulence. The sub-grid length scale Δ is based on the local grid spacing and is equal to the maximum of local grid spacing in the standard implementation.

Although this formulation is very promising, it still encounters some drawbacks. Problems arise when the wall bounded flows have thick boundary layers and small separation regions. In this case, the wall-parallel grid spacing often becomes less than the boundary layer thickness. The grid spacing is then fine enough for the DES length-scale to follow the LES branch in accordance with 3.33. LES mode within the boundary layer leads to depletion of the modeled turbulent stresses and a corresponding under prediction of skin friction [23]. This leads to separation of the flow, which

is not physical. This separation in literature is called Grid Induced Separation (GIS) in the literature [32] and excessive reduction in modeled stresses is called Modeled Stress Depletion (MSD). Because of direct dependency on grid spacing, DES method requires the grid of specific size to avoid incorrect stress predictions.

3.6.2 Delayed Detached Eddy Simulation (DDES)

To eliminate grid induced separation, Menter and Kuntz [24] proposed a shielding function that enforces RANS mode within the wall boundary layer. The shielding makes the formulation independent of the mesh system thereby eliminating grid induced separation that may occur due to the LES mode entering the boundary layer. Spalart et al. [25] proposed a generic formulation of the shielding function, which depends on turbulence length scale and eddy viscosity. The formulation resulted in the DDES (Delayed Detached Eddy Simulation) method [25]. The modified length scale definition in DDES is given by

$$\tilde{d} \equiv d - f_d \max(0, d - C_{DES}\Delta) \tag{3.34}$$

with f_d as the boundary layer shielding function. The shielding function makes use of the internal length scale of the RANS model and the wall distance. In the Spalart–Allmaras model (one equation model), the internal length scales are not available. Hence, a parameter r_d is used, which is the ratio (squared) of a model length-scale to the wall-distance. For the S-A model, the parameter is defined as:

$$r_d = \frac{\nu_t + \nu}{\sqrt{U_{i,j}U_{i,j}}\kappa^2 d^2} \tag{3.35}$$

where $U_{i,j}$ are the velocity gradients, κ the Von Karman constant and d the wall distance. This parameter is equal to 1 in the logarithmic layer and fall rapidly to zero at the edge. The shielding function is given by:

$$f_d = 1 - tanh(8r_d)^3 \tag{3.36}$$

and is designed such that its value will be 1 in the LES region (rd << 1) and 0 elsewhere. Figure 3.4 illustrates the switching mechanism near the boundary layer.

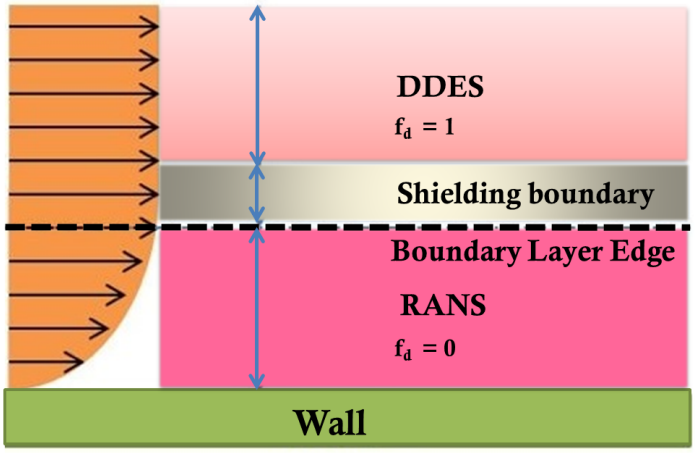

Figure 3.4: Switching mechanism of DDES method.

As per Spalart et al. [25], the values 8 and 3 in the definition of f_d are based on tests of DDES method over a flat-plate boundary layer. Considering adverse pressure gradient present in typical flow over airfoils, the values in the expression of f_d are subject to change if there is a requirement to aid or delay LES activation to avoid modeled stress depletion.

Chapter 4

Results and Discussion

This chapter details the development of the computational framework needed to achieve high accuracy in numerical prediction of static and dynamic stall flow events. A baseline computational framework is described first. This baseline framework examines and incorporates existing numerical techniques from the literature that is relevant in resolving flow undergoing laminar-turbulent transition and exhibiting weak separation. The baseline computational framework is assessed through the results obtained from numerical simulations of flow over SC1095 and VR12 airfoil sections. Series of numerical simulations are then conducted in which the turbulence length scales associated with hybrid RANS-LES methodology of the framework are analyzed along with the performance of the conventional shielding formulation. Based on the analysis, a hybrid length scale is suggested and the shielding formulation is revised to obtain high predictive accuracy from the framework

4.1 Baseline Computational Framework

4.1.1 Initial Mesh Setup

The baseline computational framework is first evaluated by conducting numerical simulations of flow over SC1095 airfoil section. SC1095 airfoil geometry is well suited for its usage in helicopter rotor blade application because of its good compromise between high $C_{l,max}$, low pitching moment and high drag divergence Mach number. There are several geometrical variants of this airfoil available in the literature with a decent number of experimental studies summarizing the corresponding sectional characteristics. The SC1095 airfoil geometry used in this work is the standard model comprising of a blunt trailing edge as shown in fig. 4.1b.

An O-grid is best suited to accurately model flow around the airfoil's blunt trailing edge. The grid generated for the baseline simulations comprises of 3 million nodes with relevant clustering and specifications prescribed for DES type methods. Figure 4.1 shows the grid clustering near the leading edge, the trailing edge and the region around the airfoil. This clustering is done to obtain nearly isotropic grid and to capture unsteady flow features resulting from separated flow when the airfoil operates in the stall and post-stall regime. The spanwise grid spacing is kept fine to 0.0068 chords with the spanwise extent of half a chord. The smallest grid spacing normal to the surface is 10^{-5} chords which resulted in $y^+ \leq 0.82$ for the forward flow simulations conducted at a Reynolds number of 2 million and Mach 0.3. The outer domain extends to 50 chords from the airfoil to eliminate disturbances from the far-field boundary. Final grid dimensions are $324 \times 124 \times 75$. Since the grid fitted on a single GPU card,

speed-up by a factor of 2.5 is obtained for simulations on a GPU card when compared to simulations conducted on 20 CPU cores.

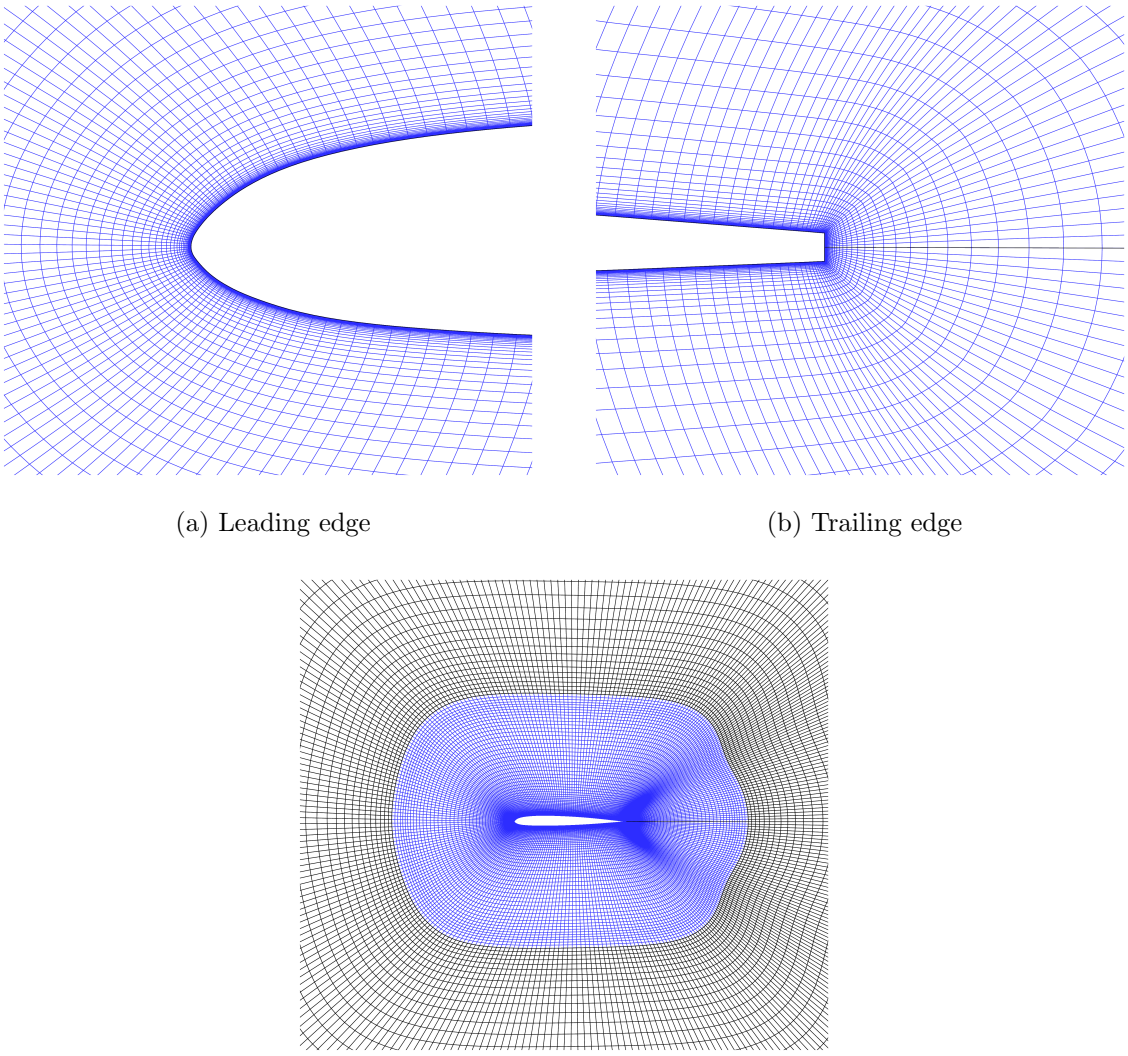

(a) Leading edge

(b) Trailing edge

(c) Region around airfoil

Figure 4.1: Grid refinement in the computational domain of SC1095 airfoil using clustering of points.

4.1.2 Laminar-Turbulent Transition model

The SA turbulence model is not equipped to handle transitional flow problems since it was developed and calibrated for fully turbulent flows at relatively high Reynolds numbers. It treats the boundary layer as fully turbulent whereas an incipient boundary layer under realistic flow conditions is typically in the laminar state without any significant mixing between adjacent fluid layers. As the boundary layer develops, instabilities may occur that will cause the transition to the turbulent state. The adequate modeling of this laminar-turbulent transition is very important for the correct prediction of wall-bounded flows as the transition substantially influences the skin friction and the energy losses in the form of heat transfer. Without accounting for transition, the model will over-predict the skin friction drag because of the greater extent of mixing between adjacent layers of fluid within the boundary layer. Treating the boundary layer as fully turbulent will have unfavorable implications on lift and prediction of separation as well. A fully turbulent boundary layer can sustain stronger adverse pressure gradient compared to the laminar boundary layer. This will reduce the susceptibility of flow to separate thereby resulting in attached flow beyond the practical stall limit. With this delayed stall, the lift will be over-predicted.

The laminar-turbulent transition in the current work is modeled using the correlation-based transition model [37] which was integrated with SA turbulence model and re-calibrated by Medida and Baeder [38]. This transition model comprises of transport equations for the intermittency coefficient and the transition criterion. The intermittency is indicative of the probability that a given point is located inside the turbulent

region. The intermittency coefficient is the fraction of time during which the flow over any particular point on the surface is turbulent. The transition criterion is expressed by means of the local transition onset momentum thickness Reynolds number which is strictly based on local variables. The transition model requires empirical relations for the onset and the length of the transition region but performs proficiently for complex three-dimensional shear flows.

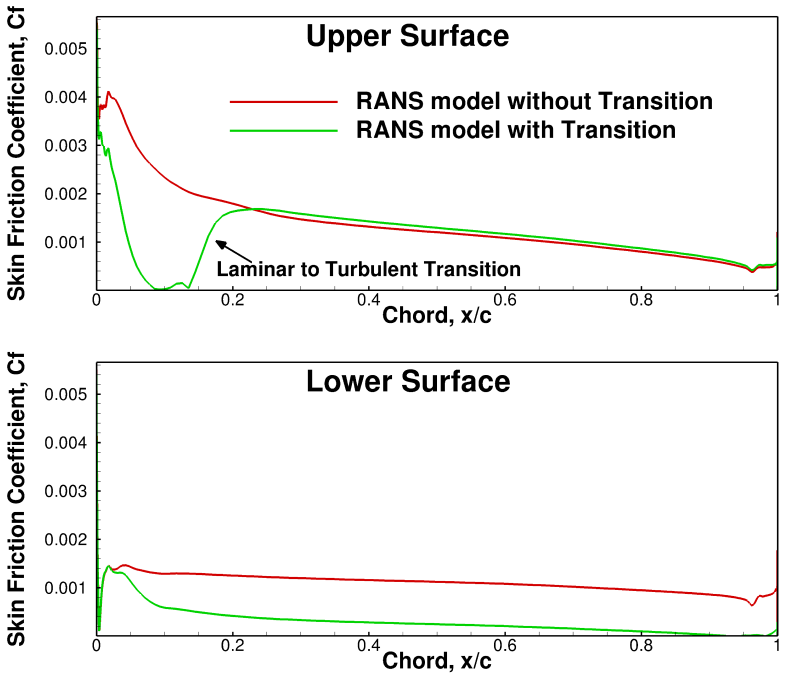

Figure 4.2: Skin friction coefficient at upper and lower surface of SC1095 airfoil.

To quantify the influence of transition modeling, flow over SC1095 airfoil is simulated at practical Reynolds number of 2 million and Mach 0.3. The angle of attack of 4° is selected to ensure that boundary layer remains attached throughout the upper

surface of the airfoil. Since the flow is fully attached, skin friction will depend strongly on the nature of boundary layer. The SA-RANS framework is used to conduct simulations with and without the transition modeling.

Figure 4.2 plots the skin friction drag along the upper and lower surface of the airfoil for the two cases shown in red and green. When transition model is enabled, the solver is able to capture the laminar-turbulent transition at the upper surface. This transition is evident from the rapid increase in skin friction drag at about 20% chord location at the upper surface. At the lower surface, transitional modeling predicts a laminar boundary layer throughout. The predicted integrated drag coefficient, in this case, is 0.008883 which matches well with the Look-up table data value of 0.008785 with the percentage error of 1.1%. In the absence of transition modeling, the boundary layer on both surfaces is fully turbulent and as a result, the skin friction drag is considerably over-predicted. The predicted integrated drag coefficient, in this case, is 0.01026 which results in percentage error of 16.8% when compared with Look-up table data. A very thorough verification and validation study of the transition model implementation and calibration is presented in [42].

4.1.3 Correction for Adverse Pressure Gradient

The ability of turbulence models to accurately model the effects of strong adverse pressure gradient (APG) is crucial to the prediction of boundary layer separation in RANS simulations. It is known that eddy viscosity based turbulence models fail to accurately predict stall onset on an airfoil section at high angles of the angle of attack

where strong adverse pressure gradient is encountered [85]. Under strong APG, The SA model over-predicts the maximum lift and stall onset. This undesirable behavior is associated with an underlying assumption in all eddy-viscosity based turbulence models. The assumption states that the production and dissipation of turbulent kinetic energy are balanced within the boundary. However, the boundary layer under strong APG is not in equilibrium [86] and the outer layer velocity scaling gets affected under the APG [42]. The viscous sub-layer and log-layer remain unchanged. Medida and Baeder suggested an empirical modification to the SA turbulence model to improve its sensitivity to strong adverse pressure gradients.

The original SA model is calibrated to predict accurate log layer in a zero pressure gradient boundary layer by assuming equilibrium between production and destruction terms. This equilibrium is maintained by the model in the defect layer with the help of a damping function f_w which controls the rate at which the destruction term decays away from the wall. Under strong adverse pressure gradient, the destruction term decays faster in a unphysical manner resulting in a boundary layer comprising of excessive modeled turbulence in the outer part a greater resilience towards separation. Based on the experimental observations [87], Medida and Baeder proposed a modification to the damping function through the reduction of Von Karman constant. They demonstrated that the proposed modification controlled the rapid decay of destruction in the outer layer and provided improved predictions in integrated aerodynamic loads.

The current work is also aimed at regulating the modeled turbulence through the outer part of the boundary layer. And to achieve this objective, this work investi-

gates the turbulence length scales involved in the DDES formulation and analyses the shielding parameters to obtain physical levels of turbulence in the boundary layer. The APG correction from Medida and Baeder [39] is integrated into the computational framework used in the current work and its impact on the turbulence length scales and as flow solutions are discussed in the following sections.

4.1.4 Convergence Improvement in Low Mach Region

The focus of the current work is in high Reynolds number flow at near-stall angles of attack. Under these conditions, the flow experiences strong pressure gradient resulting in separation from the suction surface, reverse flow and reattachment in some cases. The computational domain for such a flow regime comprises of low Mach number region within the overall high-speed flow. In the numerical solution to Navier-Stokes Equation, the conservation equations are expressed in the form of Roe upwind scheme which is a classical shock-capturing scheme widely used within the numerical solvers. In the modified form, the resulting artificial viscosity term in the momentum equations scales with the inverse of the Mach number. Because of this scaling, the numerical solution produced by the solver provides unphysical discrete results with poor convergence when the flow is nearly incompressible. Rieper et al. [59] studied the scaling issue and formulated a low Mach number fix for Roe upwind scheme. In this fix, local Mach number is multiplied to the velocity jump term in the Roe scheme making the artificial viscosity effectively independent of Mach number.

To handle low Mach numbers in this work, the aforementioned correction from

Rieper et al. is incorporated into the OverTURNS and GPU based solver. Two test cases are selected to observe the impact of all Mach correction. Flow over SC1095 airfoil at an angle of attack of 170° and Mach 0.1 is simulated using SA-RANS framework with and without the all Mach correction. Figure 4.3 depicts the pressure contours of the numerical solution obtained from the two simulations. The high-quality solution with smooth pressure contours is obtained when all Mach correction is used. Without the correction, unphysical distortion is observed in the solution along with poor convergence.

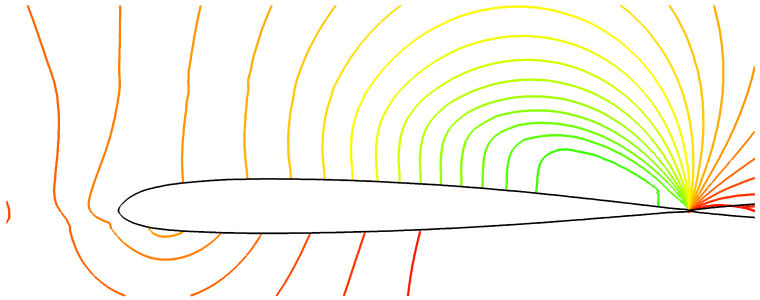

(a) Numerical solution with all Mach correction

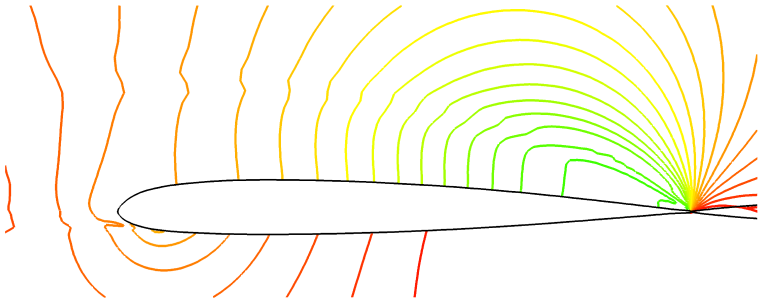

(b) Numerical solution without all Mach correction

Figure 4.3: Pressure contour lines obtained from simuating flow over over SC1095 airfoil ($\alpha = 170^0$, M = 0.1) using conventional RANS model.

4.2 Static RANS Forward Flow Simulations

The baseline computational framework is first evaluated by conducting conventional RANS simulations on the forward flow over SC1095 airfoil section under static conditions. The simulations are conducted in the comprehensive angle of attack (AoA) range starting from 2° to 20°.

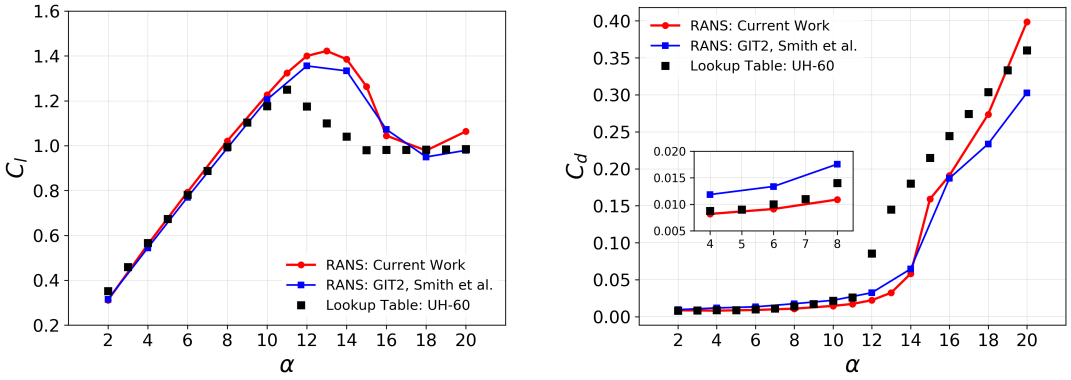

(a) Integrated lift coefficient

(b) Integrated drag coefficient

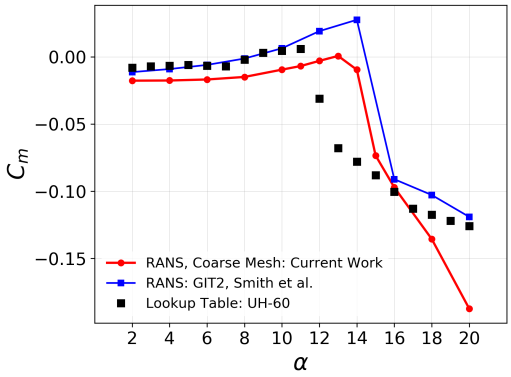

(c) Integrated pitching moment coefficient

Figure 4.4: Integrated predictions from current work and GIT (Cobalt LLC) dataset from Smith et al. [12] compared with UH-60A lookup table [11] for SC1095 airfoil.

Note that the modified $\gamma - Re_{\theta_t}$ model of Medida and Baeder [38] is active in all

the simulations to account for laminar to turbulent transition unless stated otherwise. To assess the accuracy of RANS based numerical predictions over experimental data, integrated force and moment coefficients obtained from CFD RANS data sets are compared with UH-60A lookup table data [11] in figure 4.4. The forward flow characteristics of the SC1095 airfoil can be inferred from the lookup table data. The airfoil exhibits fully attached flow until of 9° angle of attack. As the angle of attack is increased beyond 9°, marginal separation of flow begins at the trailing edge. This is evident from the slight decline in the lift curve slope in the AoA range $9° - 11°$, though the lift continues to increase with the increase in angle of attack. At around 11°, the airfoil section stalls and the flow separate completely. The lift begins to fall as the angle of attack is increased beyond this static stall limit. For comparison in figure 4.4, the first data set is the integrated results obtained from RANS simulations conducted in current work. The second data set is comprised of RANS based simulation results from the CFD code Cobalt LLC at Georgia Institute of Technology (GIT) [13]. When integrated lift coefficient is compared, there is a fair agreement between the RANS based CFD predictions and the lookup table data when the flow is fully attached ($\alpha \leq 10°$) and when the flow is extensively separated after stall (α is between 17° and 20°) as illustrated in figure 4.4a. In 4° to 11°, the flow remains almost completely attached to the surface. For the attached flow, skin friction depends strongly on the nature of boundary layer. Therefore, it is imperative to model laminar-turbulent transition of the boundary layer to obtain accurate values of the skin friction drag. The impact of transition modeling used in simulations is visible in the inset of figure 4.4b which shows the magnified plot of the drag coefficient in the 4° – 8° angle of

attack range. Integrated drag values predicted by RANS model with transition model in the current match closely with lookup table data. On the other hand, the GIT data set that used RANS based CFD code (Cobalt LLC) without transition modeling significantly over-predicts the drag values in the attached flow regime. Both the solvers however substantially under-predict the drag coefficient once the stall has occurred at an angle of attack of about 12°. Pitching moment predictions from RANS based data sets are also poor in the range 12°– 15°when compared with the lookup table data.

From the analysis, it is evident that RANS models perform poorly in the near-stall regime of 11°– 15°. They strongly over-predict the onset of the stall because they fail to accurately model important turbulence scales exhibited by weakly separated flows of the near-stall regime.

4.3 Static DDES Forward Flow Simulations

With an aim to improve the accuracy of aerodynamic load predictions, hybrid RANS-LES methods are investigated next since they provide higher fidelity compared to the RANS model. As discussed in chapter 3, DES type hybrid RANS-LES methods are selected for simulations since these methods are readily integrable into the SA-RANS framework of the current study. DES methods are able to offer accuracy close to LES with computational cost only slightly greater than RANS.

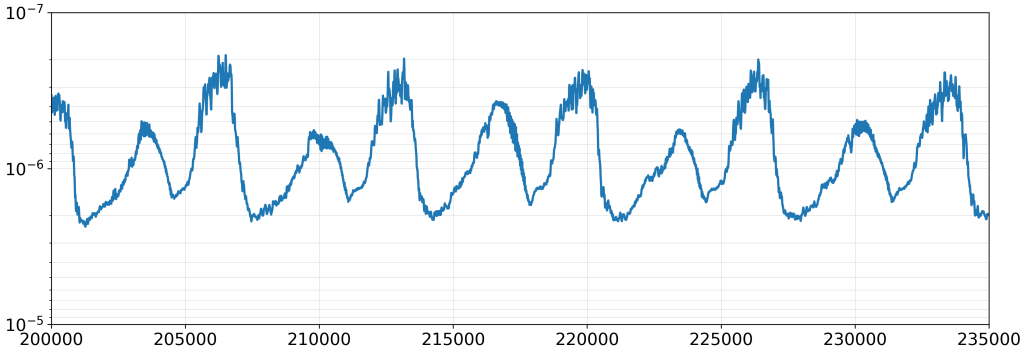

(a) Residual time history

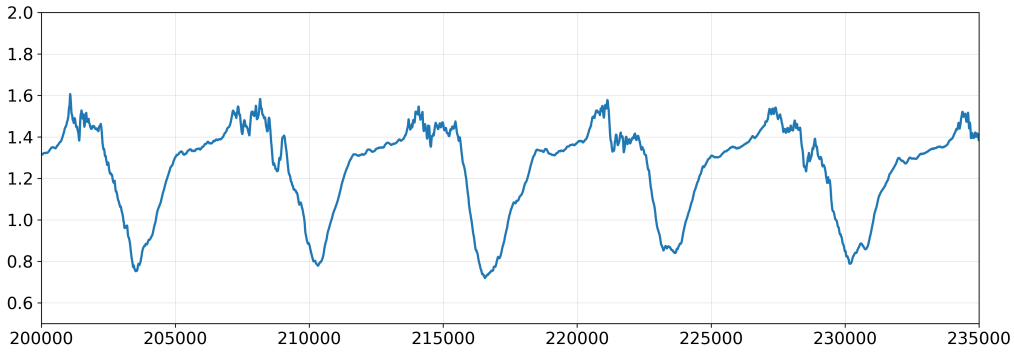

(b) C_l time history

Figure 4.5: Time history of residual (L2 norm of density) and integrated lift coefficient obtained from DDES simulation of flow over SC1095 airfoil section at 14° angle of attack.

It is to be noted that in order to achieve proper convergence under an adverse pressure gradient the DES simulations are required to be conducted at small physical time step size of the order of 0.001 and the considerable number of iterations are needed to achieve statistical convergence in unsteady flow simulations. As an instance, figure 4.5 depicts the time history of residual and integrated lift coefficient obtained

from the conventional DDES method simulation of flow over SC1095 airfoil section at 14°. The numerical solution achieved statistical convergence after 200,000 iterations. Once the statistical convergence is obtained, time-averaged integrated quantities are obtained by taking an average over 3-5 cycles of the time history.

4.3.1 Impact of Adverse Pressure Gradient Correction

Among the DES type methods, DDES method is used for conducting forward flow simulations over SC1095 airfoil section because of its ability to protect the boundary layer and eliminate modeled stress depletion in case the LES mode gets activated within the boundary layer. To quantify the impact of apparent adverse pressure present in the angle of attack range $8° - 15°$, DDES simulations are also conducted with APG correction enabled. These simulations with APG correction are referred to as DDES-APG method in the current section.

Time averaged lift coefficients taken at the mid-span of the SC1095 airfoil section obtained from RANS and DDES methods are compared in figure 4.6a in the AoA range of $4° - 20°$. Since DDES method applies RANS modeling inside the boundary layer, the predicted time-averaged coefficients are expected to be similar to RANS model predictions. In the 4° – 10° range, integrated lift predicted by RANS and DDES match well with the experiment (lookup table data). The adverse pressure gradient at upper surface is mild and the flow remains attached to the airfoil surface in this range. In the 11° – 15° angle of attack range, lift predictions are high compared to experiment as flow experiences strong adverse pressure gradient. Because of the

adverse pressure gradient, the SA turbulence model predicts excessive turbulence in the outer boundary layer of the flow making it resistant towards separation. Due to delayed separation, integrated lift values predicted by RANS and DDES methods are high. Experimental data measures the onset of a static stall at 11° while RANS and DDES method do not predict the static stall until 13°.

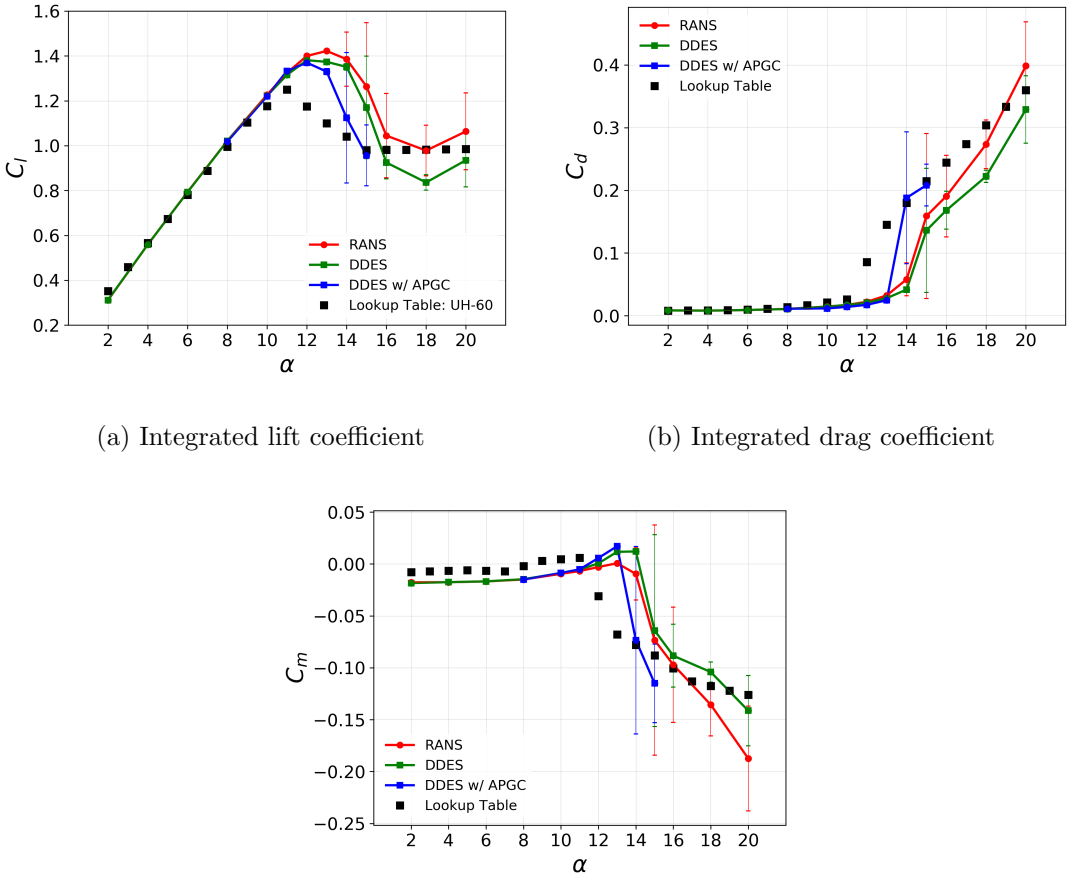

(a) Integrated lift coefficient

(b) Integrated drag coefficient

(c) Integrated pitching moment coefficient

Figure 4.6: Integrated predictions from current work and GIT (Cobalt LLC) dataset from Smith et al. [12] compared with UH-60A lookup table [11] for SC1095 airfoil.

Including the correction for strong adverse pressure gradient provides the improve-

ment in lift predictions in the near stall regime of 11° – 15°. DDES-APG method results in lower lift values which are closer to experimental data. The improvement in lift prediction becomes substantial at 14° and 15° angle of attack where the adverse pressure gradient is strongest. The error bars shown in figure 4.6 denote the standard deviation of the integrated quantities over time and quantify the unsteadiness of the flow at different angles of attack. The flow is strongly unsteady at 14°,15° and 16° once the predicted stall occurred after 13° degree angle of attack.

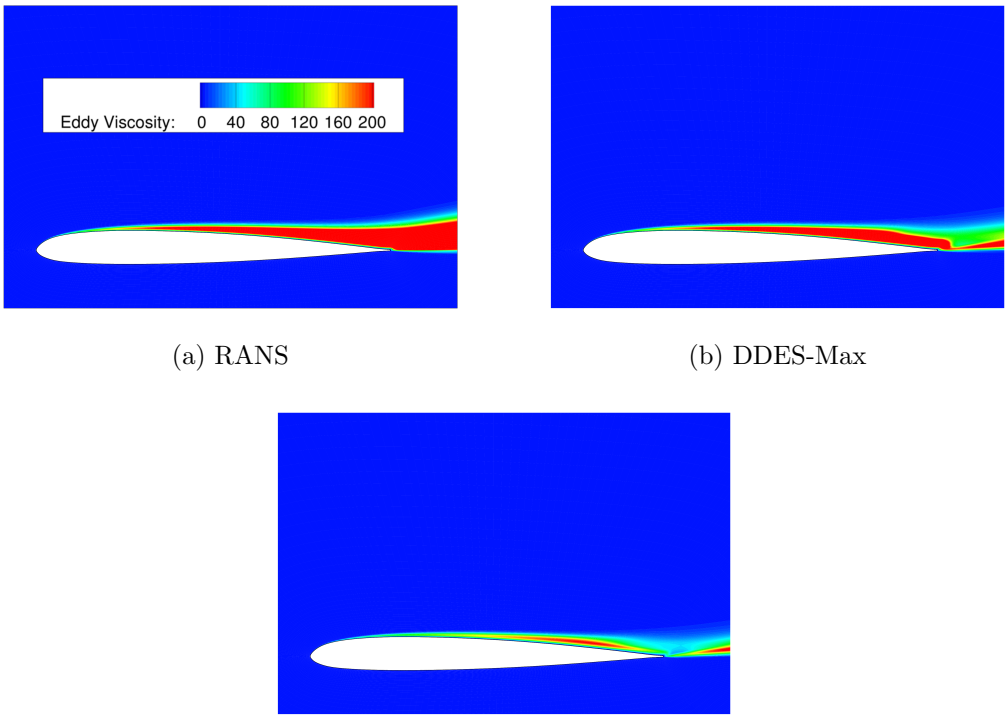

(a) RANS

(b) DDES-Max

(c) DDES-Max with APG correction

Figure 4.7: Instantaneous eddy viscosity contours for different methods at 12° angle of attack.

Figure 4.7 shows the instantaneous eddy viscosity contour plots for the numerical methods at 12° angle of attack. Because of the strong adverse pressure gradient in the

near-stall regime, RANS and DDES methods predicted high values of eddy viscosity with RANS model substantially over predicting eddy viscosity. When APG correction is included with DDES method, the levels of predicted eddy viscosity (modeled turbulence) reduced. As discussed earlier, the amount of eddy viscosity directly dictates the extent of flow separation in the near-stall regime as it governs the turbulence content in the outer part of a boundary layer. Figure 4.8 shows instantaneous vorticity contours, at 13° angle of attack for different methods. From vorticity contours it is clear that DDES-APG method is able to capture trailing edge separation which is typically observed in the experiment as well.

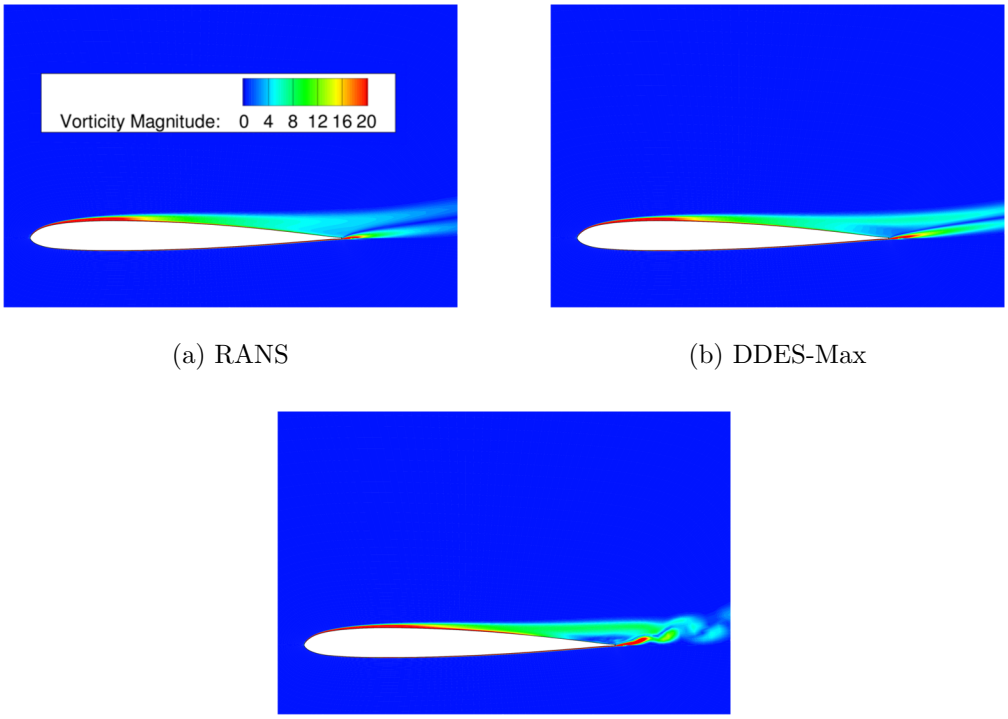

(a) RANS

(b) DDES-Max

(c) DDES-Max with APG correction

Figure 4.8: Instantaneous vorticity contours for different methods at 13° angle of attack.

4.4 Investigation of turbulence length Scales

In RANS-SA solver framework, the eddy viscosity is dominantly governed by the length scale $\tilde{d}$ which goes into the turbulence model formulation

$$\tilde{\nu} \propto S\tilde{d}^2 \tag{4.1}$$

The eddy viscosity, in turn, governs the amount of modeled turbulence and onset of flow separation which are important for lift, drag and pitching moment predictions. In DES type methods, local grid spacing parameter Δ becomes an important parameter since the turbulence length scale $\tilde{d}$ depends on Δ directly as per equations 3.33 and 3.34.

4.4.1 Max Length Scale

The typical definition of grid scale used in standard DDES formulation is given by:

$$\Delta_{max} = \max(\Delta_1, \Delta_2, \Delta_3) \tag{4.2}$$

where Δ_1, Δ_2 and Δ_3 are the three dimensions of the local grid cell. This grid scale is referred to as "Max" length scale in this work. This scale results in correct turbulence prediction only for an isotropic grid. While grid can be made isotropic away from the wall using relevant clustering of the node points, it is not possible to maintain isotropy in the near wall region for a typical airfoil grid. Since the spacing in span-wise direction is constant, the Max length scale is usually governed by span-wise grid spacing in the near wall region. Therefore, the span-wise grid spacing cannot be coarse for DES type methods.

4.4.2 Scotti Length Scale

To account for general anisotropy in the grid, Scotti length scale [35] can be used which offers a reduction in turbulence length scale through geometric mean and includes a factor dependent on the local grid aspect ratio. If $\Delta_1 \leq \Delta_2 \leq \Delta_3$, then the Scotti length scale is given by:

$$\Delta_{\text{Scotti}} = (\Delta_1 \Delta_2 \Delta_3)^{1/3} \text{f}(\text{a}_1, \text{a}_2) \tag{4.3}$$

where $\text{a}_1 = \Delta_1/\Delta_3$ and $\text{a}_2 = \Delta_2/\Delta_3$ are the two aspect ratios and $\text{f} \geq 1$ is a function equal to

$$\text{f}(\text{a}_1, \text{a}_2) \simeq \cosh \sqrt{4/27((\log \text{a}_1)^2 - \log \text{a}_1 \log \text{a}_2 + (\log \text{a}_2)^2)} \tag{4.4}$$

4.4.3 Shur Length Scale

To account for rapid wall stretching in the near wall region, Shur et al. [15] proposed an adaptive length scale definition in their IDDES formulation:

$$\Delta_{Shur} = \min\{\max[C_w d_w, C_w \Delta_{max}, h_{wn}], \Delta_{max}\} \tag{4.5}$$

where h_{wn} is the grid stepping in the wall-normal direction and C_{w} is the empirical constant. Shur length scale takes substantially small constant value in the near-wall region where the grid is highly anisotropic. The value of the length scale increases linearly as one moves away from the wall and becomes equivalent to Max length scale far away from the wall.

4.5 Proposition of a Hybrid Length Scale

In the standard DDES formulation [25], C_{DES}, the Smagorinsky constant takes the value of 0.65. Spalart et al. in their DES paper [20] recommended that the Smagorinsky constant should be of the order of one. This recommendation is based on two-dimensional experiments of homogeneous turbulence and free shear layer flow. They made it clear that the value of C_{DES} is applicable to the turbulent flow that does not contain high-frequency disturbances and C_{DES} should be made larger when there is substantial flow separation. In the DDES formulation, the boundary layer is shielded well most of the time and recalibration of C_{DES} is not needed. But as one approaches near-stall angles of attack, there is an increasing amount of LES content mixing with the outer part of the boundary layer. This mixing necessitates the re-calibration of C_{DES}. As an alternative to re-calibration of C_{DES}, alternative turbulence length scales which are more dynamically changing compared to the Max length scale are assessed in the current work. Among these length scales, Shur length scale has explicit dependence on wall distance along with local grid spacing. This wall-distance dependence accounts for wall-proximity effects and re-calibration of Smagorinsky constant is not needed. Also, the empirical constant C_w in the Shur length scale is based on well-resolved LES of the developed channel flow. This makes Shur length scale accurate in the outer region of boundary layer provided that the grid is capable of capturing LES content in that outer region. Finally, a length scale is proposed in the present work which is based on both Shur and Scotti length scales.

The proposed length scale is called Shur-Scotti-Min (SSM) and it accounts for

rapid wall stretching in the near-wall region and general anisotropy of the grid through the following definition:

$$\Delta_{Shur-Scotti-Min} = \min(\Delta_{Shur}, \Delta_{Scotti}) \tag{4.6}$$

SSM length scale adopts Shur length scale near boundary layer edge resulting in substantially reduced turbulence length scale. In region away from the wall, the turbulence length scale is computed from Scotti definition. Variation of these length scales as a function of wall distance is plotted in figure 4.9.

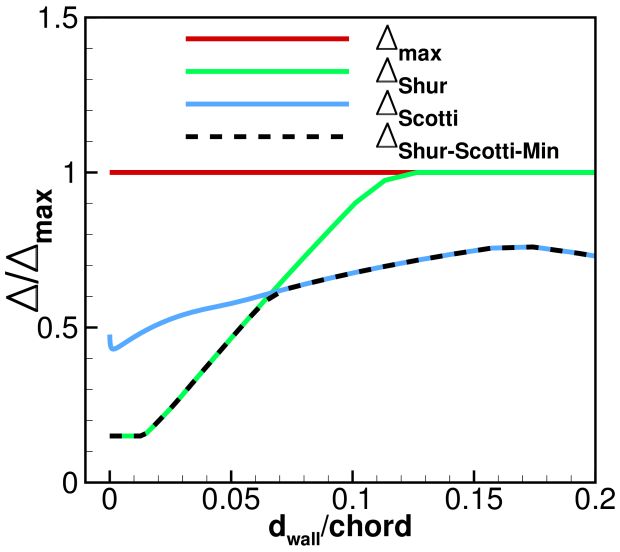

Figure 4.9: Normalized length scales plotted as function of normalized wall distance.

Normalized length scales are plotted as a function of wall distance in 4.9. In a typical grid, for up to 0.07 chords away from the wall surface, Shur length scale is minimal. This is the region with the considerable grid anisotropy due to wall-normal grid stretching. After 0.07 chords, Scotti length becomes smallest through out the

domain as Shur length scales become identical to Max length scale as one goes away from the wall.

Apart from governing eddy viscosity, length scale definition also helps in determining the location of switching between RANS and LES. Weakly separated flows have relatively thick boundary layer and relevant resolved turbulent scales are present near the edge of a boundary layer. For DDES method, since the switching takes place near the boundary layer edge, it is imperative to evaluate length scales for their ability to obtain correct modeled and resolved stresses at the interface. For the attached flow, length scale definition does not have a significant impact on the flow solution as there is no resolved content near the boundary layer and the modeled stresses are nearly same as the resolved stresses at the interface.

4.5.1 Evaluation of Length Scales

DDES simulations are conducted using different turbulence length scales to assess their predictive accuracy. Time-averaged lift, drag and pitching moment coefficients obtained by using different length scales in the DDES formulation are compared with the lookup table data in the figure 4.10.

The only near-stall regime of $11^\circ - 15^\circ$ is considered for this comparison. APG correction is enabled in all the simulations pertaining to the evaluation of length scales. The Scotti length scale provides best lift predictions compared to lookup table data as evident in figure 4.10a. Although the SSM length scale over-predicts the lift in general in the range $11^\circ - 15^\circ$, the predicted post-stall trend matched

well with the lookup table data. Also, it is the only length scale that predicted the occurrence of the stall at 11° angle of attack. Drag coefficient and pitching moment coefficients are also predicted very well by the SSM length scale as shown in figure 4.10b and 4.10c respectively.

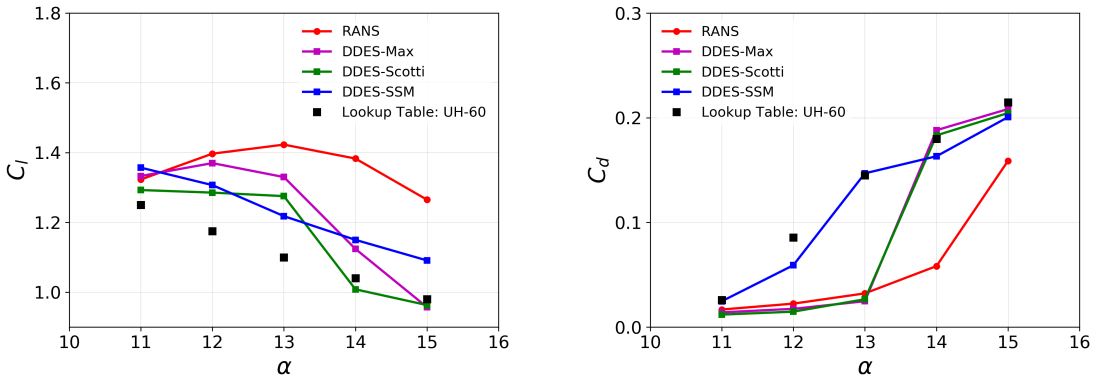

(a) Integrated lift coefficients

(b) Integrated drag coefficients

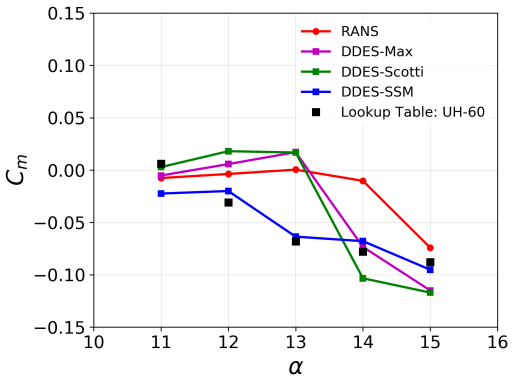

(c) Integrated pitching moment coefficients

Figure 4.10: Integrated force and moment coefficients in the 11^0–15^0 angle of attack range predicted by DDES method incorporating different length scales.

To understand why the predictions differ substantially for each of the length scales,

RANS-LES interface produced by the length scales are shown in figure 4.11 near the leading edge and the trailing edge of the airfoil section. The contours in the figure represent the magnitude of the length scale. Because of the reduced value of length scale, the RANS-LES interface produced by SSM length scale is closer to the airfoil surface compared to the interface produced by other two length scales.The proximity of the interface between the surface makes sure that the RANS mode is only active in the boundary layer and LES mode gets activated right outside the boundary layer. The proper activation of the modes results in a relevant amount of modeled turbulence in the outer part of the boundary layer making a significant difference in the predicted integrated forces. Scotti length scale definition causes some reduction in length scale compared to Max length scale definition by taking the geometric mean of the local grid dimensions and accounting for the anisotropy. This also results in the RANS-LES interface closer to the airfoil surface. However, the reduction of the length scale is not sufficient to provide the correct amount of turbulence in the defect part of the boundary layer irrespective of which mode is active. The Max length scale over-predicts the length scale value considerably in the near wall region owing to high anisotropy in the near wall region. Because of the large length scale value, the RANS mode extends significantly beyond the boundary layer as evident in figure 4.11c.

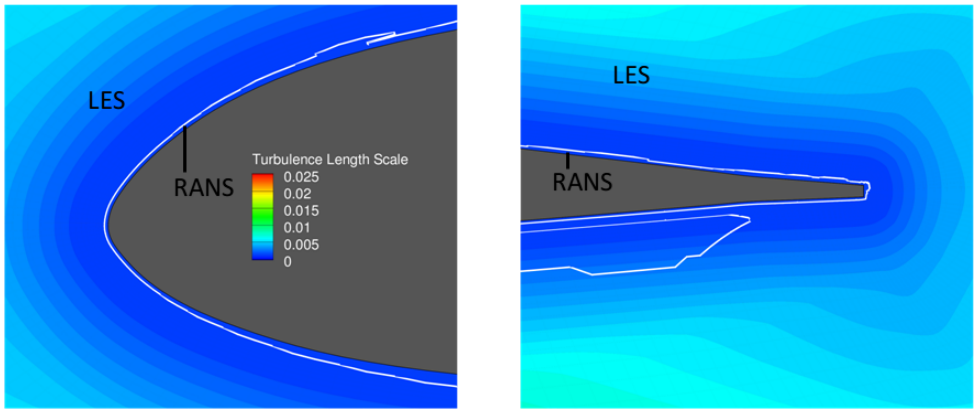

(a) SSM length scale

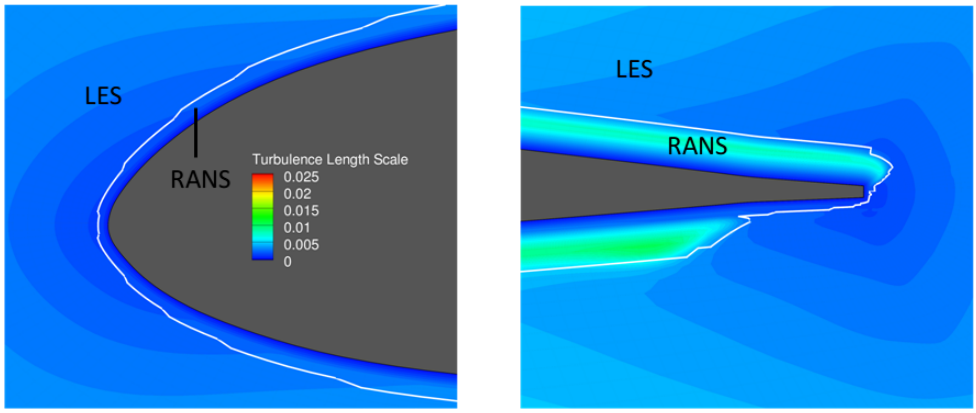

(b) Scotti length scale

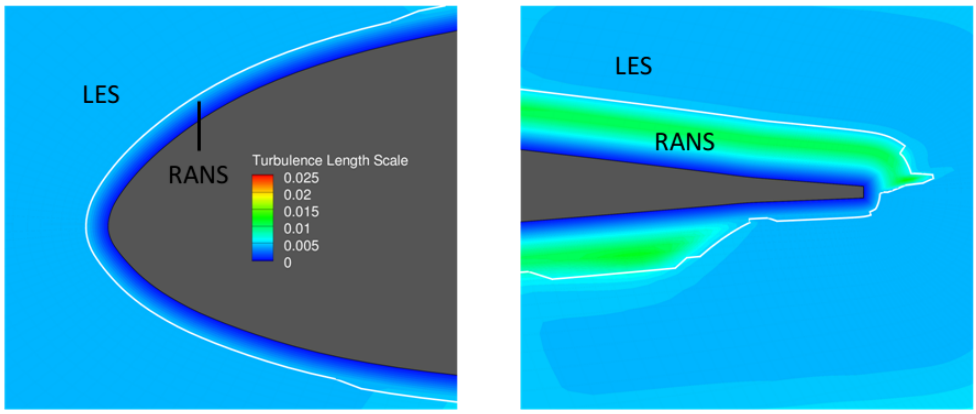

(c) Max length scale

Figure 4.11: RANS-LES interface near the leading edge and trailing edge of the airfoil section obtained by using different length scales in DDES formulation.

4.6 Senstivity of SSM length scale towards grid resolution

To test the sensitivity of the SSM length scale towards grid resolution, a second grid is generated with a high resolution in the near-wall region of the airfoil section to capture the boundary layer accurately. The second grid has dimensions $500 \times 160 \times 74$ with smallest wall-normal spacing of 5×10^{-6} chords. This wall-normal spacing results in first $y^+ \leq 0.4$. Wall stretching ratio is kept minimal in the grid to make sure there are the sufficient number of points within the boundary layer.

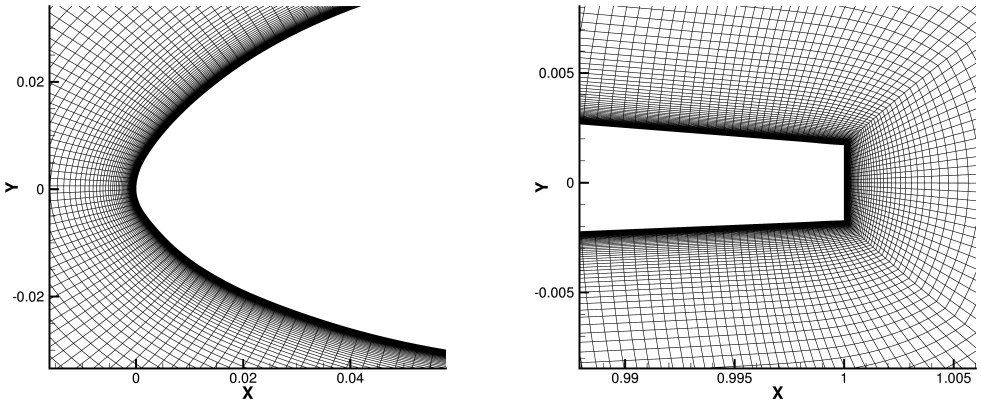

(a) Grid view near the leading edge

(b) Grid view near the trailing edge

Figure 4.12: Grid clustering near the leading and trailing edge.

The span-wise spacing for both grids is kept fine to 0.0068 chords with the span-wise extent of half a chord. Mesh points are densely packed around trailing edge to resolve the blunt trailing edge geometry of the SC1095 airfoil for both fine and coarse

grids. Also, grid clustering is done near the leading edge, trailing edge and the region around the airfoil. Figure 4.12a and 4.12b illustrate the fine grid distribution near the leading edge and trailing edge of the SC1095 airfoil respectively.

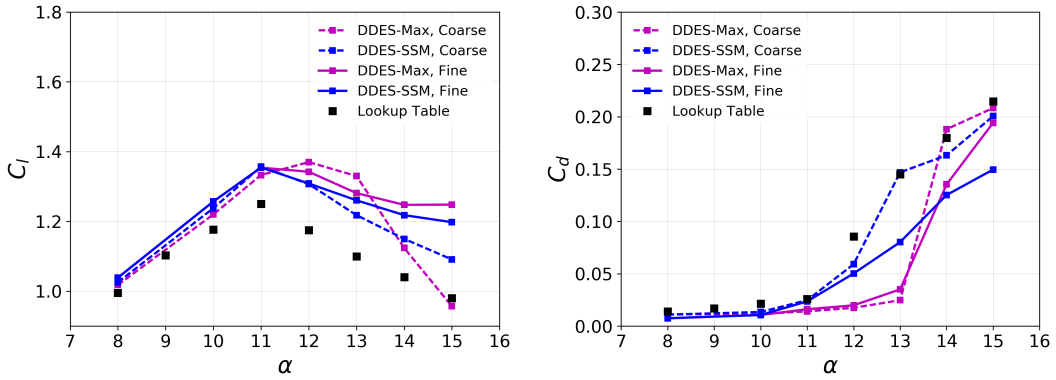

(a) Integrated lift coefficient

(b) Integrated drag coefficient

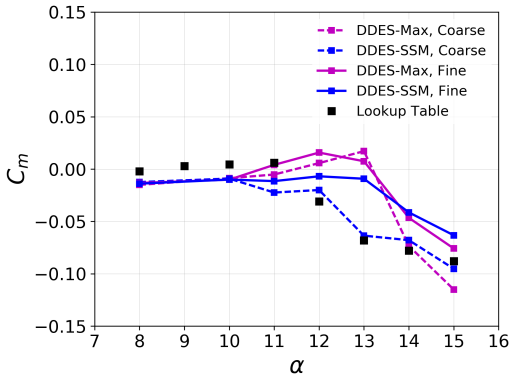

(c) Integrated pitching moment coefficient

Figure 4.13: DDES method predictions for coarse and fine grids using Max and SSM length scale.

Figure 4.13 compares aerodynamics characteristics of DDES methods obtained from grids of two resolutions and using SSM and Max length scales. In terms of onset

of stall, lift prediction improves for the Max length when the mesh is resolved. With SSM length scale, the lift predictions remain mostly unchanged with the increase in grid resolution. Drag and pitching moment predictions are certainly better for the SSM length scale as compared to Max length scale at both mesh resolutions.

Switching location for the two length scales can be visualized with the help of the shielding function used in the DDES method. Shielding function shields the boundary layer from LES mode and typically switches from zero to one as the hybrid method switches from RANS to LES. A location on the upper surface is chosen at 50% chord for shielding function analysis and shielding function is plotted against y^+along the wall-normal direction as shown in figure 4.14 for the numerical solution at 10° angle of attack. When SSM length scale is used, the location of switching is changed marginally such that SSM length scale enables switching closer to boundary layer edge.

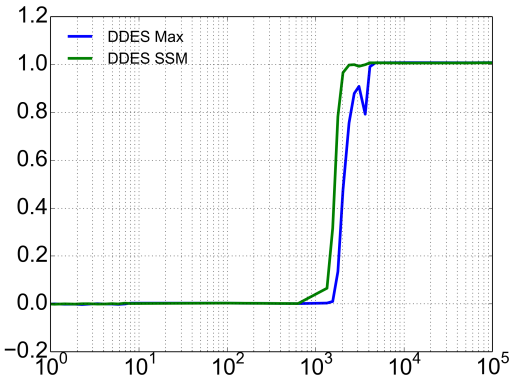

Figure 4.14: Plot of shielding function versus $y+$ at 50% chord location on the upper surface of SC1095 airfoil section obtained from flow solution at $\alpha = 10°$.

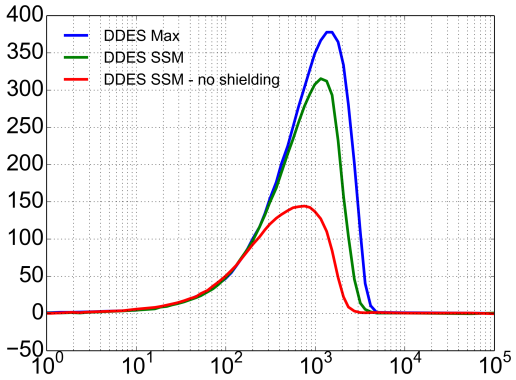

Figure 4.15: Plot of eddy viscosity versus $y+$ at 50% chord location on the upper surface of SC1095 airfoil section obtained from flow solution at $\alpha = 10°$.

The impact of SSM length scale becomes clear in figure 4.15 where eddy viscosity is plotted versus y^+ at the same selected location. The maximum eddy viscosity levels are reduced when DDES-SSM length scale is used. If the shielding function is removed, the eddy viscosity values drop drastically owing to the modeled stress depletion. This indicates that although the shielding is weakened at 10°, it remains active with SSM length scale thus averting modeled stress depletion. Note that the observable reduction in eddy viscosity with DDES-SSM is because of the marginal change in switching location and the wall distance dependent SSM length scale definition at the location of switching.

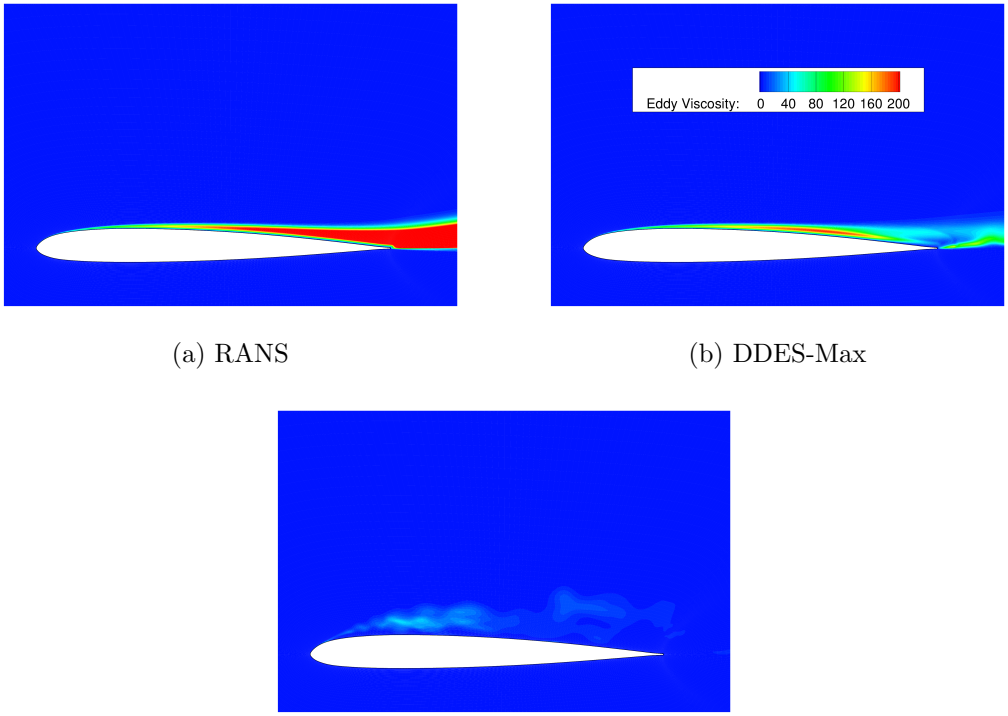

(a) RANS

(b) DDES-Max

(c) DDES-SSM

Figure 4.16: Instantaneous eddy viscosity contours for different methods at 12° angle of attack.

Figure 4.16 shows the instantaneous eddy viscosity contour plots for the numerical methods at 12° angle of attack. Because of a strong adverse pressure gradient in the near-stall regime, RANS and DDES-Max methods predicted high values of eddy viscosity with RANS model substantially over predicting eddy viscosity. SSM length scale predicts the onset of the stall at 11°matching well with experimental data and exhibited higher destruction of eddy viscosity leading to early flow separation.

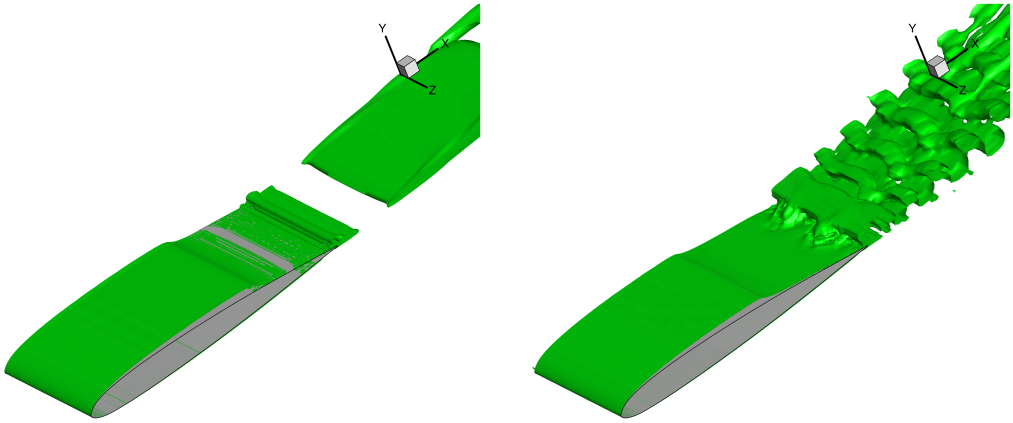

(a) DDES-Max, coarse grid. (b) DDES-Max, fine grid.

Figure 4.17: Instantaneous Iso q-criterion contours (value = 0.05) predicted by DDES-Max for two grids and two length scales at 12° angle of attack.

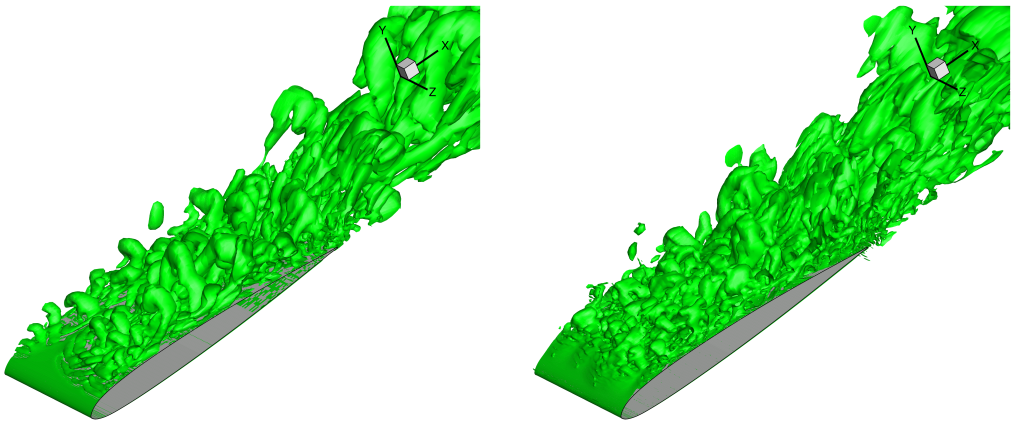

(a) DDES-SSM, coarse grid. (b) DDES-Max, fine grid.

Figure 4.18: Instantaneous Iso q-criterion contours (value = 0.05) predicted by DDES-SSM for two grids at 12° angle of attack.

The unsteady flow features captured by the numerical methods at 12° degree angle of attack are visualized through iso-surfaces of instantaneous q-criterion and are shown in figure 4.17, 4.18. DDES-Max method predicted fully attached flow for the coarse grid but exhibited incipient flow separation when the fine grid is used. DDES-SSM method predicted fully separated flow for both the grids. The structures are substantially broken down when the fine grid is used. DDES-SSM method predicted flow separation occurring very near to the leading edge near the location of laminar to turbulent transition.

4.7 VR12 Airfoil Dynamic Stall Simulations

In order to understand the impact of length scales in dynamic stall predictions, 3D time-accurate simulations are performed for modified VR12 airfoil undergoing sinusoidal pitching motion. Highly resolved O-grid with specifications analogous to SC1095 airfoil is generated for the modified VR12 airfoil geometry and is shown in figures 4.19.

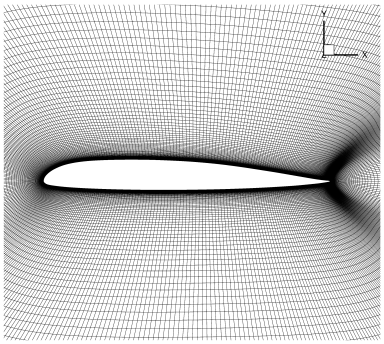

Figure 4.19: O-grid generated for modified VR12 airfoil.

Dynamic stall simulations are conducted using RANS model and DDES method with two length scales. Test case selected for dynamic stall has an angle of attack variation $\alpha = 8^\circ + 10^\circ \sin(\omega t)$ with Reynolds number of 2.1 million, Mach number of 0.3 and reduced frequency of 0.1. Detailed experimental data is available for this case from Ramaswamy et al. [17]. The lift predictions obtained from the three computational methods and from the experimental data is shown in figure 4.20.

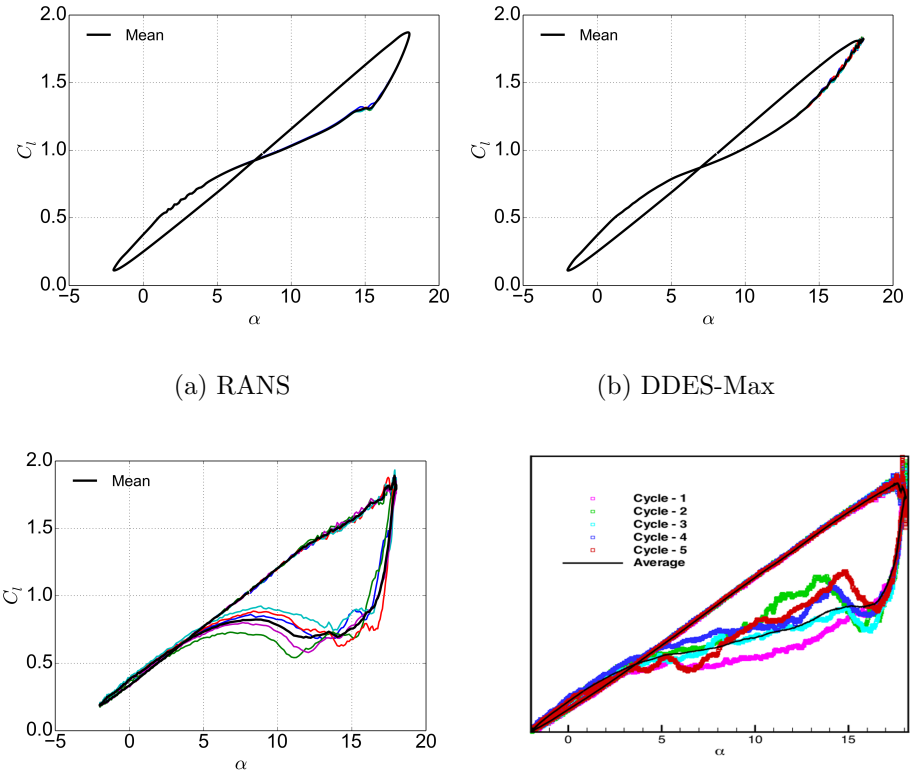

(a) RANS

(b) DDES-Max

(c) DDES-SSM

(d) Experiment [17].

Figure 4.20: Time history of lift coefficient obtained from different methods and experiment for VR12 dynamic stall simulation.

In order to visualize cycle-to-cycle variation, four cycles after convergence are

included in the lift coefficient plots. Mean of the four cycles is also included in black color. Cycle-to-cycle variation is negligible for the RANS model as shown in 4.20a. The time history of lift coefficient is smooth. As evident in figure 4.20b, DDES-Max method exhibits some unsteadiness during the downstroke. The DDES-SSM method predicted substantial cycle-to-cycle variation near the stall and during the downstroke. These variations are qualitatively similar to the observations in the experimental data. Similar to experimental data, DDES-SSM method also exhibits two lift peaks with secondary lift peak higher in magnitude than the first lift peak. The existence of two lift peaks indicates the presence of more than one dynamic stall vortex. Cycle-averaged pitching moment and drag predictions from three methods and experiment are shown in figure 4.21 DDES-SSM method perform well in predicting pitching moment and drag coefficients.

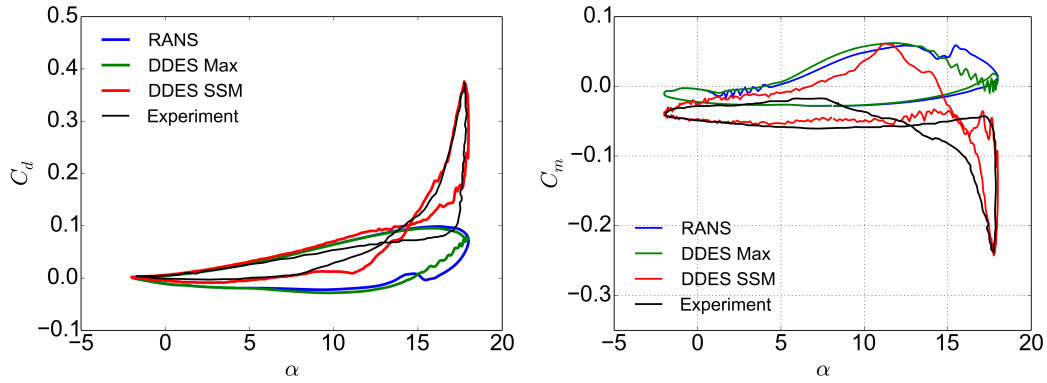

(a) Drag Coefficient

(b) Pitching Moment Coefficient

Figure 4.21: Cycle-averaged time histories of drag and pitching moment coefficients for different methods.

Note that the flow reattachment during the dynamic stall is a computationally challenging problem due to the presence of low-speed and highly unsteady, three-dimensional flow structures. Dynamic stall also exhibits strong history effects. The accuracy of predicted boundary layer during the upstroke has a substantial impact on the quality of downstroke flow solution. DDES-SSM is able to capture dynamic stall characteristics well because of accurate resolution of boundary layer during the upstroke as well as correct estimation of eddy viscosity levels. Both RANS model DDES-Max method owing to eddy viscosity predictions led to mild separation on the upper surface during the upstroke. As a result, both these methods failed to predict a deeper stall and exhibited more attached flow with earlier lift recovery in the post stall region.

4.8 Investigation of Shielding Parameters

The analysis of flow solution obtained from fine grid simulation over SC1095 airfoil indicate that conventional shielding remains functional with SSM length scale at moderate angles of attack. The reduced value of SSM length scale does alter the shielding region of the DDES method and changes the eddy viscosity levels in the LES mode. The slightly altered behavior of shielding function helps in the pertinent transition from RANS to LES mode in the near-stall separated flow regime [22]. However, reduction in length scale causes weakening of the shielding function. As a result, at 4° angle of attack, the SSM length scale with conventional shielding results in trailing edge separation induced by modeled stress depletion (MSD) as shown in

figure 4.24a.

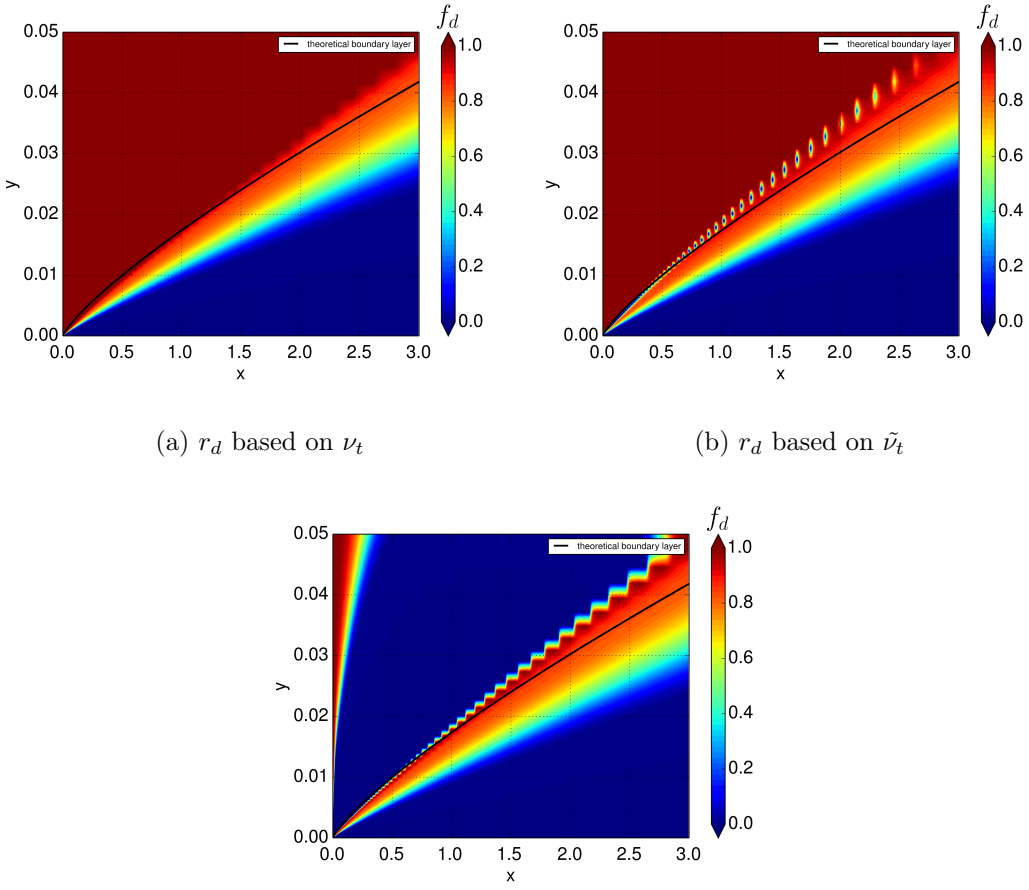

(a) r_d based on ν_t

(b) r_d based on $\tilde{\nu_t}$

(c) r_d based on $\nu_t + \nu_l$

Figure 4.22: Shielding function f_d obtained from different formulations of r_d.

Therefore, as a next step, the applicability of conventional shielding function f_d and r_d to the DDES method based on SSM length scale is investigated. A fully turbulent flow over the flat plate is setup for the investigation since the analytical solution is known for the zero pressure gradient boundary layer. The setup operates in the quasi-2D mode where the span-wise spacing is made extremely small compared

to the spacing in other two directions. Similar flat plate setup was used by Spalart et al. [25] for the calibration of their DDES method. With Spalart-Allmaras turbulence model, Shur et al. [25] recommended using $\tilde{\nu_t}$ for the computation of r_d

$$r_d = \frac{\tilde{\nu_t}}{\sqrt{U_{i,j}U_{i,j}}\kappa^2 d^2} \tag{4.7}$$

It is however not clearly stated why $\tilde{\nu_t}$ is preferred over ν_t or $(\nu_t + \nu_l)$. RANS solution is obtained for the flat plate and r_d is computed from the solution by using ν_t, $\tilde{\nu_t}$ and $(\nu_t + \nu_l)$.

Figure 4.22 compares the shielding function f_d obtained from different formulations of r_d. In the figures, the contour of f_d is plotted throughout the domain of the flat plate. The solid black line denotes the boundary layer thickness calculated from the analytical approach. Using $\tilde{\nu_t}$ for the computation of r_d results in discrete fluctuations of f_d right outside the boundary layer. This is not desirable since small fluctuations in r_d can lead to noticeable changes in the value of f_d and that will abruptly disable shielding leading to erroneous velocity predictions at the edge of the boundary layer. Using $(\nu_t + \nu_l)$ causes f_d to become zero outside the boundary layer. This will again interfere with the switching mechanism of DDES and therefore not useful. When ν_t is used instead of $\tilde{\nu_t}$, the resulting shielding function transitions smoothly from 0 to 1 or from RANS mode to LES mode and is, therefore, best suited. Now the conventional f_d parameter is given by

$$f_d = 1 - tanh(8r_d)^3 = 1 - tanh(C_{d1}r_d)^3 \tag{4.8}$$

It has been established that $C_{d1} = 8$ leads to a weak shielding for the SSM length scale which leads to MSD when the angle of attack less is than 4° for flow over the

SC1095 airfoil. To make the shielding stronger, flat plate simulations are conducted for C_{d1} = 12,14 and 16 with the definition of r_d based on ν_t.

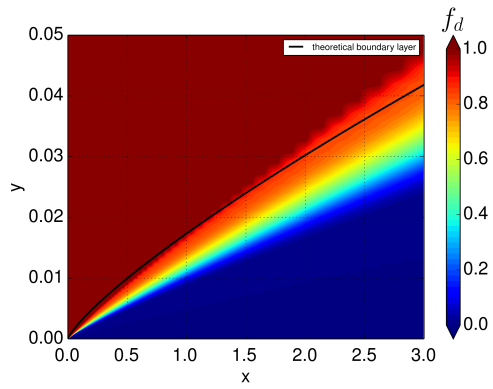

(a) $f_d = 1 - tanh(8r_d)^3$ with r_d based on ν_t

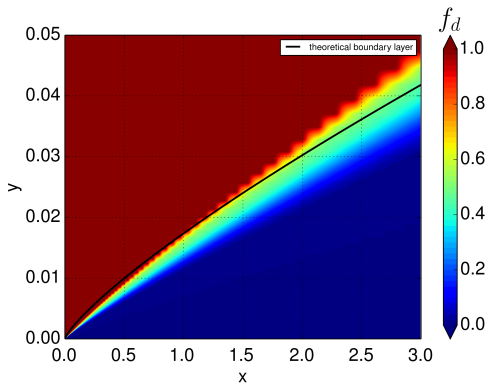

(b) $f_d = 1 - tanh(12r_d)^3$ with r_d based on ν_t

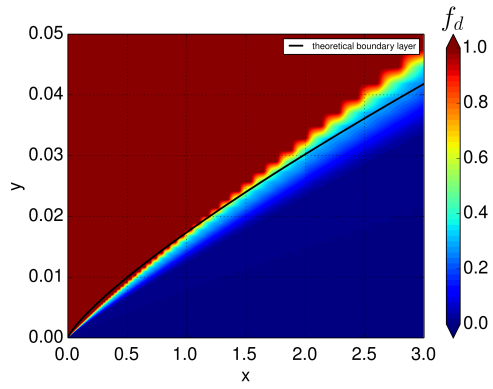

(c) $f_d = 1 - tanh(14r_d)^3$ with r_d based on ν_t

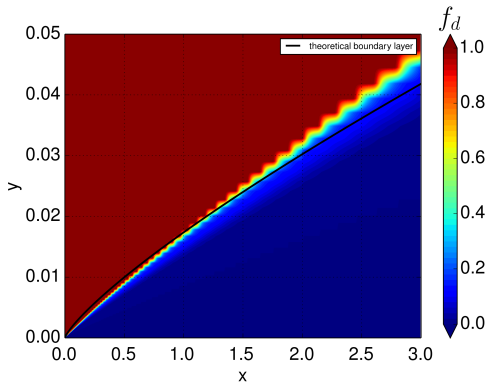

(d) $f_d = 1 - tanh(16r_d)^3$ with r_d based on ν_t

Figure 4.23: Contour plot of shielding function obtained from different values of C_{d1}.

Figure 4.23 compares the contour plot of shielding function f_d for different values of C_{d1}. Note that The boundary layer is shielded when f_d is near zero. When C_{d1} is 8, the outer part of the boundary layer that is not shielded at all. With C_{d1} of 12, the outer region of the boundary layer that is unshielded reduces. Only at C_{d1}

of 14, the boundary layer is completely shielded. Value of 16 for C_{d1} results in over-shielding. This is also not desirable since over-shielding will start suppressing LES content outside the boundary layer. So the value of 14 is chosen as new shielding parameter. The SSM length scale is then tested over the SC1095 airfoil with the new shielding parameters:

$$f_d = 1 - tanh(14r_d)^3 \quad where \quad r_d = \frac{\nu_t}{\sqrt{U_{i,j}U_{i,j}}\kappa^2 d^2}$$

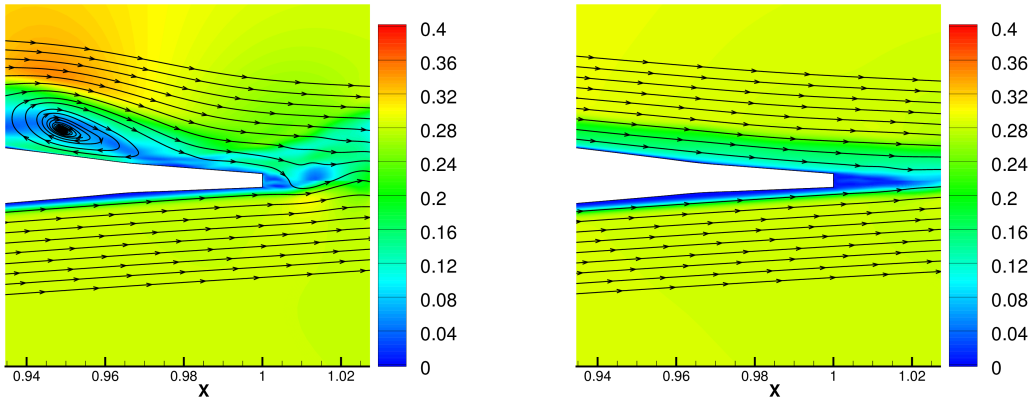

(a) $C_{d1} = 8$ with r_d based on $\tilde{\nu}_t$

(b) $C_{d1} = 14$ with r_d based on ν_t

Figure 4.24: Flow over SC1095 airfoil at 4° angle of attack simulated using DDES with two different shielding parameters.

Figure 4.24 compares the velocity magnitude contour obtained from simulation of flow over SC1095 airfoil at 4° angle of attack with a DDES-SSM method using the conventional shielding and the new shielding. Separation due to MSD is clearly eliminated from the solution when new shielding is used.

4.9 SSM Length Scale and APG Correction

The main motivation behind using adverse pressure gradient (APG) correction is to reduce the excessive modeled turbulence predicted by RANS-SA framework in the flow facing strong adverse pressure gradient.

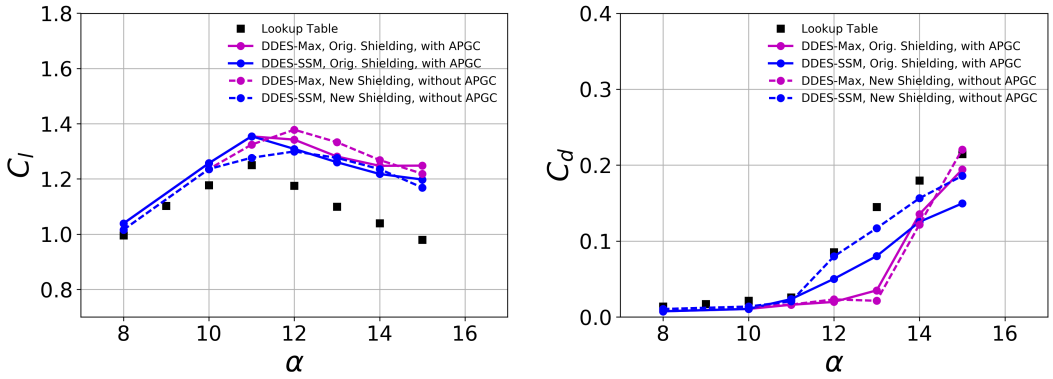

(a) Lift prediction

(b) Drag prediction

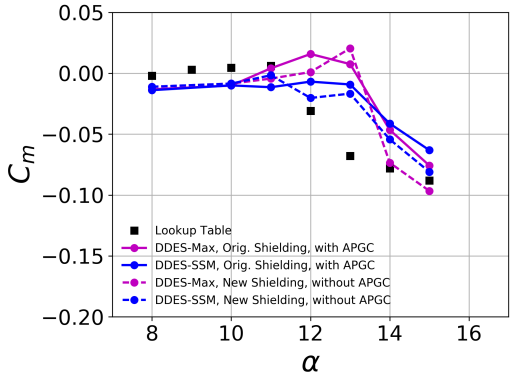

(c) Moment Prediction

Figure 4.25: Results from Max and SSM length scales with and without APG correction.

Now the SSM length scale length scale takes a small constant value in the near-

wall region of airfoil surface which is smaller than Max length scale as shown in figure 4.9. Because of reduced length scale value at the edge of the boundary layer, the eddy viscosity will also and APG correction may not be needed at all. To test this hypothesis, SC1095 flow simulations are conducted with SSM length scale (and new shielding) and with APG correction turned off. Figure 4.25 compares the integrated forces for the following four cases: (a) Max length scale with original shielding and with APG correction (b) SSM length scale with original shielding and with APG correction (c) Max length scale with new shielding and without APG correction (d) SSM length scale with new shielding and without APG correction (b). The predictions from Max length scale suffer clearly when the APG correction is turned off with over-prediction of lift and stall angle. However, with SSM length scale, the onset of lift prediction improves when the APG correction is turned off and the new shielding is used. Similarly, there is a significant improvement in the drag and pitching moment predictions when SSM length scale is used with new shielding and without the APG correction.

Chapter 5

Conclusions

This research developed an efficient computational framework to accurately resolve flow physics observed in stall events and weakly separated flows. Important flow features are discerned first through a comprehensive study of the static stall, dynamic stall, and incipient separated shear layers. It was found that modeling of laminar-turbulent transition, accounting for adverse pressure gradient and resolving low speeds within the flow-field is very important for accurate computation of aerodynamic characteristics of stalling flows. Consequently, a baseline computational framework is proposed which incorporated laminar-turbulent transition model, adverse pressure gradient (APG) correction, and a low Mach number correction. This baseline framework was evaluated through Spalart-Allmaras turbulence model based RANS simulations of flow over SC1095 airfoil section under static conditions. Simulation results demonstrated that RANS model within the baseline framework provided accurate drag predictions for the attached boundary layer because of proper resolution of laminar-turbulent transition. Simulations also established that Spalart-Allmaras

turbulence model with RANS formulation was not suited for modeling flow under the influence of strong adverse pressure gradient. The presence of APG inhibited the destruction of eddy viscosity and produced excessive modeled turbulence thus heavily over-predicting lift when the airfoil should have stalled. By including the APG correction, destruction of eddy viscosity was strengthened which resulted in substantial improvement in the lift predictions. The importance of regulating eddy viscosity for separating flows became apparent from this analysis of flow under the adverse pressure gradient.

Since the use of DNS and LES is beyond current computational resources at practical Reynolds number, DES type hybrid RANS-LES method called DDES method was investigated next to obtain the solution for separating flows with reasonable accuracy. There were clear advantages for selecting DDES method over other hybrid methodologies in this study. DDES method was readily integrable to baseline since it utilizes Reynolds stresses of RANS formulation within boundary layer and sub-grid scale stresses wherever LES was applicable. Moreover, significant adjustment in eddy viscosity can be achieved by changing sub-grid length scale definition and re-calibrating the criteria for transition from RANS to LES mode. Therefore, suitable sub-grid length scales such as those formulated by Shur [15] and Scotti [35] from the literature were assessed at the near-stall angles of attack for their ability to prescribe physical amount eddy viscosity in the outer part of the boundary layer. It was found that the choice of sub-grid length scale had a strong impact on the flow solution specifically for the airfoil type meshes where grid anisotropy increases rapidly as one proceeds towards the surface of the airfoil.

Based on the assessment and the understanding of grid-dependent formulation of each of the length scales, a novel length scale called SSM length scale was proposed that combines favorable aspects of two existing length scales. The proposed length scale was tested extensively for its robustness towards grid resolution and its interaction with transition model and adverse pressure gradient parameters of the baseline framework. Usage of SSM length within the standard DDES method led to an accurate prediction of drag coefficient, pitching moment and onset of the stall for the coarse mesh where the conventional length scale did not perform well. Apart from reducing eddy viscosity, the SSM length scale accelerates RANS to LES transition in flows involving separating shear layers within DDES. The reduction in eddy viscosity and early transition significantly facilitates the development of realistic turbulent structures in the shear layers leading to improved aerodynamic characteristics predictions. The performance of the new length scale remained consistent after mesh refinement and was superior to other length scales from the literature. Dynamic stall simulations were also conducted on modified VR12 airfoil to examine the sensitivity of length scales on dynamic flow solution. DDES method with conventional length scale was not able to predict deep stall and had a minimal cycle to cycle variation. Proposed length scale matched well with experimental data in terms of cycle-to-cycle variation, deep stall prediction and prediction of multiple dynamic stall vortices. There was no undesirable coupling between the new length scale and the transition model in the baseline framework as well.

The standard shielding function in the DDES method shielded the boundary layer effectively under the new length scale for flow nearing the static stall. However, it

was observed that the conventional shielding weakened for attached boundary layer at a low angle of attack and resulted in grid induced separation. The functioning of shielding parameters f_d and r_d employing SSM length scale definition were then investigated extensively in a quasi-2D flat plate setup. The setup provided with a suitable and stronger shielding function f_d that eliminated grid induced separation in flow over the flat plate. An alternative formulation of r_d was also identified during the investigation which ensured a smooth transition of f_d from RANS to LES mode in the outer part of the boundary layer.

As noted earlier, the main motivation behind using adverse pressure gradient correction was to regulate excessive modeled turbulence exhibited by Spalart-Allmaras model under strong adverse gradient. The SSM length scale also governs eddy viscosity directly through the modified definition of sub-grid scale. It was hypothesized and later established through SC1095 airfoil simulations that adverse pressure gradient correction is not needed at all if DDES method is used with the proposed length scale. In fact, significant improvement in the drag and pitching moment predictions were obtained when only SSM length scale was used with new shielding parameters along with transition model and all Mach correction.

5.1 Recommendations for future work

The work presented in this thesis should be seen as the first step towards a robust turbulence-resolving model tailored for resolving incipient separated flow. So far, the integrated computational framework including proposed length scale and the

re-calibrated shielding parameters have been tested only over rotorcraft pertinent airfoils. Though the results look promising, each aspect of the modeling framework, as well as the proposed length scale should be rigorously evaluated. Additional testing of the integrated framework needs to be carried out under three-dimensional conditions that closely resemble a complete rotor with proper accounting of three-dimensional effects discussed in the literature review. This testing will also highlight the performance of the integrated framework under reverse flow. To gain further confidence, the integrated framework must be applied to other classes of flows which exhibit strong recirculation and free-shear layers. Flow over a wall-mounted hump and backward facing step are some of the canonical domains available for such testing that will also assess the reattachment prediction capability of the integrated framework. Included methodologies in the framework are selected and refined for Reynolds numbers pertinent to rotorcraft operation. Additional investigation is required to establish any sensitivity of the framework towards lower Reynolds numbers.

For the next phase of this work, the main emphasis should be to reduce empiricism and grid dependence that comes from DDES method. Hence, IDDES [36] method which brings the advantages of wall-modeled LES in the traditional DES type formulation should be investigated next with the objective of resolving anisotropic content within the boundary layer of incipient separated flows. The main advantage of using IDDES is that it does not enforce RANS model throughout the boundary layer while ensuring that there is no modeled stress depletion. IDDES is able to resolve turbulence content present in the outer region of the boundary layer (near-wall turbulence) through a series of blending functions provided that there is a resolved turbulence

present within the boundary layer. This requires injection of synthetic turbulent content within the boundary layer in case the flow generated turbulence is not present. The injected synthetic turbulence should be as close to physical turbulence as possible and that itself is an area of intensive research. This makes the application of IDDES challenging for incipient separated flows as it requires a zonal approach of identifying the correct region and then injecting a suitable synthetic turbulence in that region. Nonetheless, IDDES predictions are highly accurate (comparable to LES) which are independent of length scale considerations or RANS to LES transition location and therefore IDDES method makes a vital candidate for future work.

Bibliography

[1] Bousman, W., "Aerodynamic Characteristics of SC1095 and SC1094 R8 Airfoils", *NASA Ames Research Center TP-212265*, 2003.

[2] McCroskey, W., McAlister, K., Carr, L. and Pucci, S., "An Experimental Study of Dynamic Stall on Advanced Airfoil Sections Volume 2. Pressure and Force Data", *TM-84245, NASA*, 1982.

[3] Leishman, J. G., "Principles of Helicopter Aerodynamics", *2nd Edition, Cambridge University Press, New York,* 2006.

[4] McCroskey, W. J., "Inviscid Flowfield of an Unsteady Airfoil", *AIAA Journal, 11(8), pp. 1130-1137*, 1973.

[5] McCroskey, W. J. (1982), "Unsteady Airfoils", *Ann. Rev. Fluid Mech., 14, pp. 285-311*, 1982.

[6] McCroskey, W.J., Carr, L.W., McAlister, K.W., "Dynamic Stall Experiments on Oscillating Airfoils", *AIAA Journal, 14(1), pp. 57-83*, 1976.

[7] Carr, L. W., McAlister, K. W., McCroskey, W. J., "Analysis of the Development

of Dynamic Stall Based on Oscillating Airfoil Experiments", *NASA TN D-8382*, 1977.

[8] McAlister, K. W., Carr, L. W., and McCroskey, L. W., "Dynamic Stall Experiments on the NACA 0012 Airfoil", *NASA Technical Paper 1100*, 1978.

[9] Carr, L., "Progress in Analysis and Prediction of Dynamic Stall", *Journal of Air- craft, vol. 25, no. 1, pp. 6–17*, 1998.

[10] DiOttavia, J., Watson, K., Cormey, J., Komerath, N. and Kondor, S., "Discrete Structures in the Radial Flow Over a Rotor Blade in Dynamic Stall", *26th AIAA Applied Aerodynamics Conference, AIAA 2008-7344, (Honolulu, HI)*, January 2008.

[11] Howlett, J. J., "UH-60A Black Hawk engineering simulation program. Volume 1: Mathematical model",*NASA-CR-166309, NASA Technical Report,* 1981.

[12] Smith, M.J., Wong, T., Postdam, M., Baeder, J.D., and Phase, S., "Evaluation of CFD to Determine Two-Dimensional Airfoil Characteristics for Rotorcraft Applications", J*ournal of the American Helicopter Society, Vol. 51, No. 1*, 2006.

[13] Strang, W. Z., Tomaro, R. F., and Grismer, M. J., "The Defining Methods of Cobalt60: a Parallel, Implicit, Unstructured Euler/Navier- stokes Flow Solver", *AIAA 99-0786,* 1999.

[14] Anderson, W. K., and Bonhaus, D. L., "An Implicit Upwind Algorithm for Computing Turbulent Flows on Unstructured Grids", *Computers and Fluid, Vol. 23, No. 1,* 1994.

[15] Travin, A.K., Shur, M., Spalart, P.R., Strelets, M.K., "Improvement of delayed detached eddy simulation for LES with wall modeling", *European conference on computational fluid dynamics ECCOMAS CFD 2006, TU Delft*, 2006.

[16] Jain, N., Baeder, J.D.,"Aerodynamic Characteristics of SC1095 Airfoil using Hybrid RANS-LES Methods Implemented into a GPU Accelerated Navier–Stokes Solver", *AIAA Aviation Forum, Dallas, Texas,* 22-26 June 2015.

[17] M. Ramasamy, J. S. Wilson, W. J. McCroskey, P. B. Martin,"Measured Characteristics of Cycle-To-Cycle Variations in Dynamic Stall", *AHS Technical Meeting on Aeromechanics Design for Vertical Lift, San Francisco, CA,* January 20–22, 2016.

[18] Piomelli, U., and Balaras, E.,"Wall layer models for large eddy simulations",*Annual Review of Fluid Mechanics*, 2002.

[19] Spalart, P.R., Jou, W.H., Strelets, M., Allmaras, S.R., "Comments on the feasibility of LES for wings, and on a hybrid RANS/LES approach", *Proceedings of first AFOSR international conference on DND/LES*, 1997.

[20] Spalart, P.R., Jou, W.H., Strelets, M., Allmaras, S.R., "Comments on the feasibility of LES for wings, and on a hybrid RANS/LES approach", *Proceedings of first AFOSR international conference on DND/LES*, 1997.

[21] Krishnan, V., Squires, K.D., Forsythe, J.R., "Prediction of separated flow characteristics over a hump using RANS and DES", *AIAA-2004-2224*, 2004.

[22] Jain, N., Baeder, J.D.,"Assessment of turbulence model length scales based on Hybrid RANS-LES modeling of unsteady flow over airfoil", *AHS 72nd Annual Forum, West Palm Beach Florida*, May 17–19, 2016.

[23] Gritskevich, M.S., Andrey, V.G., Schütze, J., and Menter, F.R., "Development of DDES and IDDES Formulations for the $k-\omega$ Shear Stress Transport Model", *Flow Turbulence and Combustion 88:431–449*, 2012.

[24] Menter, F.R., Kuntz, M., Langtry, R., "Ten years of experience with the SST turbulence model", *4th International Symposium on Turbulence Heat and Mass Transfer, pp. 625–632,* 2003.

[25] Ghosh D., Baeder, J.D., "Compact Reconstruction Schemes with Weighted ENO Limiting for Hyperbolic Conservation Laws", *SIAM Journal of Scientific Computing, Vol. 34, No. 3, pp. A1678–A1706,* 2012.

[26] P. Spalart., "Strategies for turbulence modelling and simulations", *International Journal of Heat and Fluid Flow, 21(3):252–263,* 2000.

[27] S. Pope, "Turbulent Flows", *Cambridge University Press*, 2000.

[28] Smagorinsky, J., "General Circulation Experiments with the Primitive Equations", *Monthly Weather Review*, 1963.

[29] E. de Villiers, "The Potential of Large Eddy Simulation for the Modelling of Wall Bounded Flows", *PhD thesis, University of London, Imperial College, London,* 2006.

[30] P.A. Davidson. Turbulence, "An introduction for scientists and engineers", *Oxford University Press, fourth edition*, 2007.

[31] J. Smagorinsky, "General circulation experiments with the primitive equations: I. the basic experiment*", Monthly Weather Review*, *91:99–164*, 1963.

[32] P. Spalart, "Detached-eddy simulation", *Annual Review of Fluid Mechanics*, *41:181–202*, 2009.

[33] Smith, M.J., Liggett, N.D., and Koukol., B.C.G., "Aerodynamics of Airfoils at High and Reverse Angles of Attack", *Journal of Aircraft, Vol. 48, No. 6*, November-December 2011.

[34] Medida, S., and Baeder, J.D., "Numerical Investigation of 3-D Dynamic Stall using Delayed Detached Eddy Simulation", *50th AIAA Aerospace Sciences Meeting, Nashville, Tennessee,* 09 - 12 January 2012.

[35] Scotti A., Meneveau, C., and Fatica, M., "Dynamic Smagorinsky model on anisotropic grids", *Center for Turbulence Research Proceedings of the Summer Program,* 1996.

[36] Shur, M.L., Spalart, P.R., Strelets, M.K., Travin, A.K., "A hybrid RANS-LES approach with delayed-DES and modeled LES capabilities", *International Journal of Heat and Fluid Flow 29*, 2008.

[37] R. B. Langtry, "A correlation-based transition model using local variables for unstructured parallelized CFD codes", *PhD thesis, University of Stuttgart*, 2006.

[38] Medida, S., Baeder, J.D., "Application of the Correlation-based $\gamma - Re_{\theta t}$ Transition Model to the Spalart-Allmaras Turbulence Model", *20th AIAA Computational Fluid Dynamics Conference,* 27 - 30 June 2011.

[39] S. Medida, J. D. Baeder, "Adverse Pressure Gradient Modification to Turbulence Models for Wall-bounded Flows", *21st AIAA Computations Fluid Dynamics Conference, San Diego, CA,* June 2013.

[40] J. D. Baeder G. R. Srinivasan, "Turns: A Free-Wake Euler/Navier-Stokes Numerical Method for Helicopter Rotors", *AIAA Journal, 31(5):959–962,* 1993.

[41] J. Blazek, "Computational Fluid Dynamics: Principles and Applications", *Second Edition, Elsevier Science*, 2006.

[42] Medida S., "Correlation-based Transition Modeling for External Aerodynamic Flows", *PhD Thesis, University of Maryland, College Park*, 2014.

[43] Thomas, S., Baeder, J.D., "A GPU Accelerated Navier-Stokes Solver with Multi-level Granularity for Solving Sparse Implicit Systems", *21st AIAA Computational Fluid Dynamics Conference, San Diego, California*, June 2013.

[44] Jude, D., Baeder, J., "Extending a Three-Dimensional GPU RANS Solver for Unsteady Grid Motion and Free-Wake Coupling", *54th AIAA Aerospace Sciences Meeting, AIAA SciTech Forum,San Diego, California,* January 2016.

[45] F. M. White, *"Viscous Fluid Flow"*, *McGraw-Hill, 3 edition*, 2005.

[46] P. R. Spalart and S. R. Allmaras, "A one-equation turbulence model for aerodynamic flows", *Recherche Aerospatiale, (1):5–21*, 1994.

[47] B. E. Launder, G. J. Reece, and W. Rodi., "Progress in the development of a reynolds-stress turbulent closure", *Journal of Fluid Mechanics, 68(3):537–566*, 1975.

[48] P. Durbin, "A reynolds stress model for near wall turbulence", *Journal of Fluid Mechanics, 249:465–498*, 1993.

[49] B. Baldwin and H. Lomax, "Thin layer approximation and algebraic model for separated flows", *16th AIAA Aerospace Sciences Meeting, number 1978–257, AIAA*, 1978.

[50] P. Durbin, "Near-wall turbulence closure modeling without damping functions", *Theoretical and Computational Fluid Dynamics, 3:1–13*, 1991.

[51] B. Van Leer, "Towards the ultimate conservative difference scheme: V. a second-order sequel to godunov's method", *Journal of Computational Physics, 135(2):229–248*, 1997.

[52] Ghosh D., Baeder J.D., "Compact Reconstruction Schemes with Weighted ENO Limiting for Hyperbolic Conservation Laws", *SIAM Journal of Scientific Computing, Vol. 34, No. 3, pp. A1678–A1706,* 2012.

[53] B. Koren, "Upwind schemes, multigrid and defect correction for the steady navier-stokes equations", *Proceedings of the 11th International Conference on Numerical Methods in Fluid Dynamics,* 1988.

[54] P. Roe., "Approximate riemann solvers, parameter vectors and difference schemes", *Journal of Computational Physics, 135(2):250–258*, 1997.

[55] C. Hirsch., "Numerical computation of internal and external flows", *Volume–2,Wiley Publishers*, 1990.

[56] A. Jameson and S. Yoon., "Lower-upper implicit schemes with multiple grids for euler equations", *AIAA Journal*, *Vol.25, No.7*, *929–935*, 1987.

[57] T. Pulliam., "Time accuracy and use of implicit methods", *11th AIAA Computational Fluid Dynamics Conference*, *number 1993–3360*, 1993.

[58] E. Turkel, "Preconditioning techniques in computational fluid dynamics", *Annual Review of Fluid Mechanics, 31:385–416*, 1999.

[59] Rieper, F., "A low Mach number fix for Roe's approximate Riemann solver", *Journal of Computational Physics*, *Vol. 230, pp. 5263–5287*, 2011.

[60] V. K. Lakshminarayan, "Computational investigation of micro-scale coaxial rotor aerodynamics in hover", *PhD thesis, University of Maryland College Park*, 2009.

[61] T. H. Pulliam and D. Chaussee, "A diagonal form of an implicit approximate factorization algorithm", *Journal of Computational Physics, 39(2):347–363*, 1981.

[62] Williamson, C. H. K. and Govardhan, R., "Vortex-Induced Vibrations," *Annual Review of Fluid Mechanics, Vol. 36, pp. 413–455, 2004.*

[63] Warming, R., and Beam, R., "On the Construction and Application of Implicit Factored Schemes for Conservation Laws", *SIAM-AMS Proceedings, Vol. 11, pp. 85-129*, 1978.

[64] Gerontakos, P., "Unsteady Airfoil Flow Control via a Dynamically Deflected Trailing-Edge Flap, Ph.D. Dissertation", *Department of Mechanical Engineering, McGill University, Montreal, Canada,* 2008.

[65] McCullough, G. B., Gault, D. E., "Examples of Three Representative Types of Aifoil-Section Stall at Low Speed", *NACA TN 2502*, 1951.

[66] Mulleners, K. and Raffel, M., "The onset of dynamic stall revisited", *Exp Fluids, 52, pp. 779-793*, 2012.

[67] Ward, J. W., "The Behaviour and Effects of Laminar Separation Bubbles on Aerofoils in Incompressible Flow," *Journal of the Royal Aeronautical Society, 67, pp. 783-790*, 1963.

[68] Gardner, A. D., "Influence of rotation on dynamic stall," *68th American Helicopter Society International Annual Forum 2012", Fort Worth, Texas, USA, pp. 464-474*, 2012.

[69] Sharma, D. M. and Poddar, K., "Experimental Investigations of Laminar Separation Bubble for a Flow Past an Airfoil", *Proceedings of ASME Turbo Expo 2010: Power for Land, Sea and Air, Glasgow, UK,* 2010.

[70] Martin, J. M., Empey, R. W., McCroskey, W. J., and Caradonna, F. X., "An

Experimental Analysis of Dynamic Stall on an Oscillating Airfoil", *Journal of the American Helicopter Society, 19(1), pp. 26-32,* 1974.

[71] Barla, C., Geissler, W., Berton, E., Raffel, M. and Favier, D., "Dynamic Stall Investigations on NACA0012 and OA209 Airfoils", *31st European Rotorcraft Forum, Florence*, 2005.

[72] Ekaterinaris, J., Menter, F., "Computation of Oscillating Airfoil Flows with One- and Two-Equation Turbulence models," *AIAA Journal, 32(12), pp. 2359-2365*, 1994.

[73] Carr, L. W., Chandrasekhara, M. S., "Compressibility Effects on Dynamic Stall", *Progress in Aerospace Sciences, 32(6), pp. 523-573*, 1996.

[74] Bowles, P. O., Coleman, D. G., Corke, T. C., Thomas, H. O., and Wasikowskim, M., "Compressibility Effects on Aerodynamic Damping During Dynamic Stall Effects", *American Helicopter Society 68th Annual Forum, Fort Worth, Texas, pp. 246-264*, 2012.

[75] Johnson, W., "Rotorcraft Aerodynamics Models for a Comprehensive Analysis", *American Helicopter Society 54th Annual Forum, Washington, DC*, May 20-22, 1998.

[76] Lee, T., Gerontakos, P., "Investigation of flow over an oscillating airfoil", *Journal of Fluid Mechanics, 512, pp 313-341*, 2004.

[77] Glauert, H., "Airplane Propellers", *In: Division L of Aerodynamic Theory, edited by W.F.Durand, Springer Verlag, Berlin, Germany*, 1935.

[78] Theodorsen, T., "General Theory of Aerodynamic Instability and the Mechanism of Flutter", *NACA Report 496*, 1934.

[79] McCroskey, W. J., Philippe, J. J., "Unsteady Viscous Flow on Oscillating Airfoils", *AIAA Journal, 13, pp. 71-79*, 1975.

[80] Ericsson, L. E., Reding, J. P., "Fluid Mechanics of Dynamic Stall Part 1. Unsteady Flow Concepts", *Journal of Fluids and Structures, 2, pp. 1-33*, 1988.

[81] Jose, A. I., Leishman, J. G., Baeder, J. D. (2006), "Unsteady Aerodynamic Modeling with Time-Varying Free-Stream Mach Numbers", *Journal of the American Helicopter Society, 51(4), pp. 299-318*, 2006.

[82] Leishman, J. G.; Beddoes, T. S., "A Semi-Empirical Model for Dynamic Stall", *Journal of the American Helicopter Society, Volume 34, Number 3, pp. 3-17(15)*, 1 July 1989.

[83] Ko, S., McCroskey, W. J. (1997), "Computations of Unsteady Separating Flows over an Oscillating Airfoil", *AIAA Journal, 35(7), pp. 1235-1238*, 1997.

[84] D. C. Wilcox, "Turbulence Modeling for CFD", *DCW Industries, Inc., La Canada, CA*, 2006.

[85] A. Celic and E. H. Hirschel, "Comparison of eddy-viscosity turbulence models in flows with adverse pressure gradient", *AIAA Journal, 44(10):2156–2169*, 2006.

[86] F. H. Clauser, "The turbulent boundary layer. Advanced Applied Mechanics", *Vol. 4, pp. 1–54*, 1956.

[87] A. E. Perry and W. H. Schofield "Mean velocity and shear stress distributions in turbulent boundary layers", *The Physics of Fluids, 16(12):2068–2074*, 1973.